

GC
7,1
S53
1989

Tidal Dynamics and Dispersion Around Coastal Headlands

by

Richard Peter Signell

B.S., University of Michigan (1983)
S.M., Massachusetts Institute of Technology (1987)

Submitted in partial fulfillment of the
requirements for the degree of

Doctor of Philosophy

at the

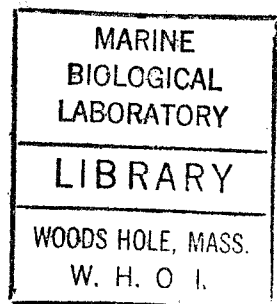
MASSACHUSETTS INSTITUTE OF TECHNOLOGY

and the

WOODS HOLE OCEANOGRAPHIC INSTITUTION

September 1989

© Richard Peter Signell, 1989



The author hereby grants to MIT permission to reproduce and
to distribute copies of this thesis document in whole or in part.

Signature of Author *Richard P. Signell*

Joint Program in Physical Oceanography
Massachusetts Institute of Technology
Woods Hole Oceanographic Institution
August 28, 1989

Certified by *W. Rockwell Geyer*
W. Rockwell Geyer
Assistant Scientist, Applied Ocean Physics and Engineering
Thesis Supervisor

Certified by *Robert C. Beardsley*
Robert C. Beardsley
Senior Scientist, Physical Oceanography
Thesis Supervisor

Accepted by *Carl I. Wunsch*
Carl I. Wunsch
Chairman, Joint Committee for Physical Oceanography, Massachusetts Institute of
Technology/Woods Hole Oceanographic Institution



1990

GIFT

WHOI

The dynamics of shallow tidal currents and tide-induced dispersion are investigated around coastal headlands that have alongshore length scales that are comparable to or less than the tidal excursion. Depth-averaged shallow water equations forced by oscillatory flow are solved numerically for Gaussian headlands. The tidal flows around these headlands are shown to be characterized by flow separation and transient eddy formation. Idealized models of flow separation and the transport and damping of vorticity away from the headland explain much of the observed behavior. The characteristics of the separated wake are compared with known results from the study of viscous flow around bluff bodies. The kinematics of particle dispersion in the numerical solutions is described and analyzed.

Rich Signell

Tidal Dynamics and Dispersion Around Coastal Headlands

by

Richard Peter Signell

Submitted to the Massachusetts Institute of Technology—
Woods Hole Oceanographic Institution
Joint Program in Physical Oceanography
on September 11, 1989, in partial fulfillment of the
requirements for the degree of
Doctor of Philosophy

Abstract

This thesis concerns the dynamics of tidal currents and tide-induced dispersion around coastal headlands. The depth-averaged shallow water equations forced by a oscillatory x -directed current with amplitude U_o and frequency σ are solved numerically for a Gaussian headland described by $\zeta(y) = b \exp[-1/2(x/a)^2]$. The water depth H is constant except for a shoaling region along the boundary which is narrow compared to the headland width b .

Solutions to this idealized tidal flow around a headland reveal a wide range of dynamical behavior, from quasi-linear, non-separating flow to strongly nonlinear, separating flow with transient eddy formation. During each half tidal cycle, transient eddies are formed when vorticity generated in the narrow shoaling region along the headland separates from the coast and wraps up to form a large scale transient eddy. For a fixed headland shape, the structure of the flow depends primarily on the relative sizes of the tidal excursion $[2U_o/\sigma]$, the frictional decay length scale $[H/2C_D]$ (where C_D is the depth-averaged drag coefficient), and the length scale of the headland a . If the frictional length scale is much shorter than the tidal excursion, then flow is quasi-steady, and can be described by a frictional Reynolds number $Re_f = [H/C_D a]$. If the frictional length scale is much longer than the tidal excursion, then the flow is controlled by $K_c = [U_o/\sigma a]$. In many tidal flows, the frictional length scale is comparable to the tidal excursion, and both Re_f and K_c control the structure of the flow.

Material released in the vicinity of the headland is stretched and folded by the high strain and transient eddy formation associated with the strongly nonlinear tidal flow, resulting in much greater dispersion than that associated with tidal turbulence. The character and extent of particle dispersion depends strongly on the interior vorticity structure arising from the boundary layer separation, and cannot be accurately described by a uniform eddy diffusivity when separation occurs.

Thesis Supervisor: W. Rockwell Geyer

Title: Assistant Scientist, Applied Ocean Physics and Engineering

Thesis Supervisor: Robert C. Beardsley

Title: Senior Scientist, Physical Oceanography

Acknowledgments

I would like to thank Bob Beardsley and Rocky Geyer for their encouragement, advice, many hours of discussion, and strategically timed words of inspiration. I also appreciate the time and interest expended by the rest of my committee members: Dave Chapman, Paola Rizzoli and Bob Weller. Thanks to my fellow Joint Program students for making the years fly by, and to Jack, who forced me to give basketball a try. Finally, I would like to thank Libby for providing enough love, support, and friendship to make nearly anything possible!

This work was supported by NSF grant OCE-87-11031 and the National Center for Atmospheric Research. Additional funding was provided by the Woods Hole Oceanographic Institution's Ocean Venture Fund, Coastal Research Center, and Education Program.

Contents

1	General Introduction	12
1.1	Introduction	12
1.2	Previous work	13
1.2.1	Tide-induced residual flow	13
1.2.2	Tidal headland flow	14
1.2.3	Tide-induced Lagrangian transport	16
1.3	Thesis objectives	18
2	Model Equations and Numerical Techniques	20
2.1	Introduction	20
2.2	Model equations	21
2.2.1	Depth-averaging the shallow-water equations	21
2.2.2	Differences between 2-D and 3-D	23
2.3	Numerical techniques	27
2.3.1	Eulerian flow modeling	27
2.3.2	Lagrangian flow modeling	29
2.4	Summary	30
3	Tidal Flow Around a Gaussian Headland	31
3.1	Introduction	31
3.2	Input parameters	32
3.3	Elevation, velocity and vorticity fields	34
3.3.1	Snapshots over a tidal cycle	34

3.3.2	Time series at fixed locations	40
3.3.3	Harmonic decomposition	44
3.4	The vorticity balance	54
3.4.1	The depth-averaged vorticity equation	54
3.4.2	The Eulerian vorticity balance	55
3.4.3	The Lagrangian vorticity balance	58
3.5	Summary and discussion	59
4	Tidal Dynamics	62
4.1	Introduction	62
4.2	An idealized model of flow separation	62
4.2.1	Potential flow	63
4.2.2	The boundary layer	71
4.2.3	Flow separation with bottom friction	74
4.3	Vorticity evolution in the interior	78
4.4	Parameter dependence	80
4.4.1	Introduction	80
4.4.2	Important length scales and dimensionless parameters	81
4.4.3	Simulations with varying parameters	82
4.5	Stability of the separated shear layer	100
4.6	Strength of the wake	102
4.6.1	Comparison of the idealized wake strength model to numerical simulation results	110
4.7	Results from viscous flow around bluff bodies	115
4.7.1	Steady flow	116
4.7.2	Adjustment to impulsive start-up	120
4.7.3	Oscillatory flow	123
4.7.4	Application to the tidal headland problem	124
4.8	Conclusions	125

5	Tidal Dispersion	127
5.1	Introduction	127
5.2	Stretching and folding: the basic mixing mechanism	128
5.3	The Eulerian and Lagrangian residual currents	132
5.4	Dispersion experiments	135
5.4.1	Dispersion from a point release: an example	135
5.4.2	Parameter dependence of dispersion	139
5.5	Discussion	141
6	Summary and Conclusions	145
A	Details of the Numerical Model	152
A.1	The basic difference scheme	152
A.2	Advection scheme	155
A.3	Shapiro filtering	155
A.4	Boundary conditions	156
A.5	Time splitting	158
A.6	Operational procedure	158

List of Figures

2-1	Vertical structure of secondary flow	25
3-1	Model geometry and numerical grid	33
3-2	The modeled tide at 0 lunar hours	36
3-3	The modeled tide at 1 lunar hour.	37
3-4	The modeled tide at 3 lunar hours	38
3-5	The modeled tide at 6 lunar hours	39
3-6	Observations of the current field at 3 and 6 hours at Gay Head, Massachusetts	41
3-7	Elevation, velocity and vorticity time series locations.	42
3-8	Time series of elevation, velocity and vorticity at selected grid points. . . .	43
3-9	Tide at 3 lunar hours reconstructed from mean, M_2 , and M_4 frequencies . .	45
3-10	Tide at 6 lunar hours reconstructed from mean, M_2 , and M_4 frequencies . .	46
3-11	Harmonic decomposition of the vorticity at Point C	48
3-12	Harmonic constituents of elevation.	49
3-13	The M_2 velocity field.	50
3-14	The mean and M_4 velocity fields	51
3-15	M_2 , mean and M_4 vorticity fields	53
3-16	Location of points for Eulerian vorticity balance calculation.	56
3-17	Vorticity and Eulerian vorticity balance at Points D, E, and F.	57
3-18	Lagrangian vorticity balance	60
4-1	Schematic of potential flow calculation around a bump in a channel wall . .	64
4-2	Potential flow solution around Gaussian and elliptic headlands.	65

4-3	Pressure gradient along the boundary of an elliptic headland for an advection dominated case	67
4-4	Pressure gradient along the boundary of an elliptic headland for a friction dominated case	68
4-5	Pressure gradient along the boundary of an elliptic headland for a time-dependence dominated case	69
4-6	Schematic of flow separation	74
4-7	Vorticity at slack water for Case 1.	85
4-8	Vorticity at slack water for Case 2	86
4-9	Vorticity at slack water for Case 3	86
4-10	Vorticity at slack water for Case 4	87
4-11	Vorticity at slack water for Case 5	88
4-12	Vorticity at slack water for Case 6	89
4-13	Vorticity at 0, 3, 6, 9 and 12 lunar hours for Case 6	90
4-14	Vorticity at slack water for Case 7	91
4-15	Vorticity at slack water for Case 8	92
4-16	Vorticity at slack water for Case 9	93
4-17	Vorticity at slack water for Case 10	93
4-18	Vorticity at slack water for Case 11	94
4-19	Vorticity at slack water for Case 12	95
4-20	Vorticity at slack water for Case 13	95
4-21	Vorticity for Case 14	96
4-22	Vorticity at slack water for Case 15	97
4-23	Vorticity at maximum eastward flow for Case 15	97
4-24	Schematic of the tidal structure as a function of Re_f , and K_c for aspect ratio 4.	99
4-25	Schematic of idealized shear layer	101
4-26	Circuit for circulation balance calculation	104
4-27	Circulation and circulation balance for Case 10	105
4-28	Vorticity flux off headland tip for Case 1.	107
4-29	Irrotational flow velocity at distance δ off the headland tip.	109

4-30	Circulation balance for Case 10 from idealized flux/damping model.	111
4-31	Comparison of peak vorticity flux and circulation between the full numerical model and the flux/damping model.	113
4-32	Streamlines and vorticity contours for flow past a cylinder at Reynolds number $Re = 4$	117
4-33	Streamlines and vorticity contours for flow past a cylinder at Reynolds number $Re = 40$	118
4-34	Streaklines for flow past a cylinder at Reynolds number $Re = 10,000$	119
4-35	Starting vortex on a wedge	121
4-36	Growth of vortices on an accelerated plate.	122
5-1	Patch deformation over 1 tidal cycle in Case 10.	129
5-2	Growth of the box perimeter from Figure 5-1 with time	132
5-3	The Lagrangian residual velocity calculated at 0 lunar hours	133
5-4	The Eulerian tide-induced residual flow	134
5-5	Dispersion of two patches of material released at 0 lunar hours.	136
5-6	Time sequence of relative dispersion	137
5-7	Dispersion of two patches with turbulence	138
5-8	Dispersion coefficient for Cases 1, 2 and 3 based on particles released at 3 lunar hours	140
5-9	Dispersion coefficient for Cases 7 and 8 at 3 lunar hours	141
A-1	Schematic of Richardson grid	153
A-2	Numerical phase speed for angled derivative advection scheme	156

List of Tables

4.1	Results of a boundary layer model for flow separation around an elliptic cylinder	77
4.2	Length scales varied in simulations	83
4.3	Parameters varied in simulations	84
4.4	Wake strength from numerical and idealized models	112

Chapter 1

General Introduction

1.1 Introduction

In most coastal seas and embayments, currents are dominated by tides. When tides encounter variations in the coastline and bathymetry, nonlinearity in the governing dynamics allows the fundamental frequencies to interact, generating residual and harmonic current components. These nonlinear components can strongly affect the structure of the flow and play an important role in the long-term transport of material in the water column and at the bed. A critical length scale is the tidal excursion $[2U_o/\sigma]$, where U_o and σ are the amplitude and frequency of the tidal current. In regions where the tidal excursion is small compared to the scale of spatial variability in the flow, the nonlinearly generated constituents are small compared to the fundamental components and the tide-induced Lagrangian residual transport of material can be obtained from a knowledge of the Eulerian flow field. This weakly nonlinear nature was exploited by Huthnance (1973) to model the circulation around sand banks in the North Sea, and by Loder (1980), who successfully showed that the clockwise circulation observed in drifter studies around Georges Bank (Bigelow, 1927) could be explained by tide-induced residual currents generated by the topography of the bank. In contrast, in regions where the flow varies rapidly over a tidal excursion, the magnitude of the residual and harmonic current components may become comparable to the fundamental tidal flow, and the relationship between Lagrangian transport and the Eulerian flow field will in general be analytically untractable (Zimmerman, 1979). Pasmanter (1988) has

showed that under these conditions, particle trajectories in simple spatially varying tidal flows can exhibit chaotic behavior, resulting in complicated dispersion characteristics.

In this thesis, the dynamics of tidal currents and tide-induced dispersion around coastal headlands (or promontories) are investigated. Emphasis is placed on strongly nonlinear tidal flows which have important implications for tide-induced dispersion. Depth-averaged shallow-water equations forced by oscillatory flow are solved numerically for a Gaussian headland. Using this idealized approach allows the important nondimensional parameters governing the nature of the tidal currents and the tide-induced dispersion to be identified.

1.2 Previous work

1.2.1 Tide-induced residual flow

It has long been known that ebb and flood tidal currents can be asymmetric and give rise to residual motions. Scientific interest in tide-induced residual currents, however, increased in the early 1970s, after quantitative measurements of mean circulation were performed around sand banks in the North Sea (Caston and Stride, 1970). Nihoul and Ronday (1975) showed theoretically by decomposing the depth-averaged tidal current into oscillatory and mean components and time-averaging the nonlinear terms in the governing equations, that the oscillatory component could drive residual flow through a mechanism they termed "tidal stress". Zimmerman (1978) emphasized that to produce a force, this stress must vary spatially, and that in coastal areas, this spatial variability is provided by variations in the bathymetry and geometry. Interpreting the generation of residual circulation by the transfer of depth-averaged relative vorticity from the fundamental tidal frequency to the mean, Zimmerman concluded that for residual circulation to exist, the fundamental oscillatory tide must generate vorticity, the oscillatory vorticity must have a streamwise gradient, and the oscillatory vorticity gradient must be partially in phase (correlated) with the oscillatory tidal flow.

1.2.2 Tidal headland flow

Along a coastline, the tidal current is reduced near the boundary due to frictional effects, and the horizontal shear associated with this current reduction represents vorticity that is largely in phase with the oscillatory current. Variations in coastline geometry, such as those associated with a coastal headland, introduce streamwise gradients in this tidal vorticity which are often in phase with the velocity, allowing efficient generation of residual and harmonic circulation.

One of the first studies of nonlinear tidal flow in rapidly changing geometry was conducted by Tee (1976, 1977), who showed that the gross structure of residual eddies around Cape Split in the Bay of Fundy could be represented by a depth-averaged nonlinear numerical model forced by the M_2 (12.42 hours) tide only. Tee found that vorticity was produced in side-wall boundary layers along the Cape and was advected into the interior by flow separation at the tip of the Cape. He argued that as long as a no-slip boundary condition is applied in a numerical model, proper resolution of the boundary layer is not critical, since the total vorticity in the layer depends only on the current at the outer edge. It was later shown by Abbott et al. (1985) that models with rectangular grid elements (like Tee's) introduce vorticity into the flow regardless of whether the no-slip condition is satisfied due to numerical difficulties at grid cell corners along the discretized boundary.

In a series of papers, Pingree (1977, 1978, 1979) studied the residual and harmonic circulation around a headland in more detail. Pingree (1979) proposed that in typical shallow-water tidal flow, vorticity at the headland is primarily generated by bottom frictional torque rather than the no-slip boundary condition. Using a high-resolution grid that properly resolved the bathymetric variation near the coast, he was able to represent the observed tide-induced residual circulation in the vicinity of Portland Bill, a headland in the English Channel (Pingree, 1977). In addition to the residual circulation, Pingree described the tide-induced mean elevation and vorticity, and the M_2 and M_4 (6.21 hours) fields.

Robinson (1981) took a different approach to understanding tide-induced residual flow, making estimates of the magnitude and distribution based on a simple 1-D Lagrangian vorticity model. He showed that for conceptual purposes, the relative vorticity can be regarded as a passive scalar which is acquired by fluid elements in a specified source region,

advected with the oscillatory tidal flow, and decayed by bottom friction. The principal conclusions were that the tide-induced residual circulation could not extend more than a tidal excursion of the vorticity source, and that the magnitude of the circulation should be controlled by the ratio of the tidal period to the frictional decay time.

Imasato (1983) studied a numerical model of tidal flow through a narrow strait separating a bay from the coastal ocean. In his model the coastline changed dramatically over the scale of a tidal excursion, and strong transient eddies formed downstream of the strait during each half-cycle. Imasato asserted that the usual approach of decomposing the tide into frequency components and discussing each component separately was physically meaningless, since the flow was strongly nonlinear, and he suggested that the usefulness of tide-induced residual velocity as a concept be reconsidered. Instead, he focussed on the formation and evolution of the transient eddies over the course of the tidal cycle, and discovered that the structure of the flow was sensitive to the value of bottom friction, which determined how rapidly the eddies decayed with time.

Wolanski et al. (1984) observed the generation of eddies on each phase of the tide past a small narrow island oriented nearly perpendicular to the dominant tidal streams. With an array of 24 current meters, float measurements, CTD studies and aerial photographs, they were able to describe the observed flow in detail. From the aerial images, the wake appeared to be similar to steady wakes observed in lab experiments around a flat plate at a Reynolds number $Re = 10$. Calculating the effective viscosity A_H from drifter experiments, however, they obtained a value of $Re = 1000$. To explain a much greater effective viscosity in the observed flow, they proposed a Reynolds number based on the ratio of advection to bottom friction, which they termed the "island wake parameter". For their study, friction was comparable to advection, and a stable wake was observed. Wolanski et al. then speculated that if friction dominated over advection, quasi-potential flow would result, and eddies would not form. If friction was smaller than advection, they predicted the wake would be unstable, and at very small friction levels that 2-D viscous lab results would apply.

Black and Gay (1987) criticized Wolanski et al. (1984) for not considering the time-dependent nature of tidal flow in their description of island wakes. They observed that in a frictional tidal flow, currents near the boundary can reverse direction several hours before

the free-stream currents due to the increased inertia of the free-stream flow. Claiming that this phase difference is responsible for the generation of eddies downstream of a headland, they stated that the eddy strength was not primarily governed by flow separation at the tip of the headland. In this thesis it is shown that although time-dependence is an important aspect of the tidal dynamics, it is the time-dependence of vorticity injected into the interior at the point of flow separation that is important for generating transient eddies.

1.2.3 Tide-induced Lagrangian transport

While measurements and numerical model output are obtained at fixed points in space (the Eulerian reference frame), many important problems in coastal waters, such as larval dispersal and pollutant transport, depend on calculating the net movement of particles following the fluid (the Lagrangian reference frame). If the horizontal currents at scales comparable to the water depth are resolved, then transport consists of two parts: a component due to the deterministic Eulerian velocity field (advection), and a stochastic component due to 3-D turbulence (diffusion).

If diffusive effects are unimportant, then net transport of material can be expressed in terms of the Eulerian velocity field by the Euler-Lagrange transformation. If $\mathbf{u}_e(\mathbf{x}, t)$ is the Eulerian velocity and $\mathbf{u}_l(\mathbf{x}_o, t)$ is the Lagrangian velocity of a parcel starting at location \mathbf{x}_o , the velocities are related by

$$\mathbf{u}_l(\mathbf{x}_o, t) = \mathbf{u}_e[\mathbf{y}(\mathbf{x}_o, t)] \quad (1.1)$$

where \mathbf{y} is the trajectory given by

$$\mathbf{y}(\mathbf{x}_o, t) = \mathbf{x}_o + \int_0^t \mathbf{u}_l(\mathbf{x}_o, t') dt'. \quad (1.2)$$

The transformation is nonlinear in that to obtain the Lagrangian velocity at a certain point, the trajectory must be known, but to determine the trajectory, the Lagrangian velocity must be known.

For some flows the Euler-Lagrange transformation is quasi-linear, and an approximate analytic expression for the Lagrangian velocity may be obtained from the Eulerian velocity field. An important example is an oscillatory Eulerian flow field in which the velocity varies slowly with respect to the excursion length ($2U_o/\sigma$), where U_o is the current amplitude and

σ is the frequency. In this case, the Lagrangian velocity of a parcel can be expressed in terms of the Eulerian velocity and velocity gradient at the initial location of the parcel \mathbf{x}_0 (Longuet-Higgins, 1969). When averaged over a tidal cycle, the residual Lagrangian velocity may be non-zero, and is called the Stokes drift. If an Eulerian residual velocity field exists that is weak compared to the oscillatory flow and varies over scales that are large compared to the excursion length, then the net motion may be expressed in words as

$$\mathbf{u}_{Lagrange} = \mathbf{u}_{Euler} + \mathbf{u}_{Stokes} \quad (1.3)$$

(Longuet-Higgins, 1969).

Zimmerman (1976) showed that for random bottom bathymetry, Eulerian tide-induced residual circulation is most efficiently produced by topographic variation of comparable length to the tidal excursion. In tidal flows, therefore, it must be expected that the scale of the tide-induced Eulerian residual current is often comparable to or less than the tidal excursion. In the case that the Eulerian tide-induced residual is weak compared to the oscillatory component, Zimmerman (1979) demonstrated that for certain flows an analytic relation between the Lagrangian residual and the Eulerian velocity can still be obtained. An important conclusion was that the Lagrangian residual velocity is different than the sum of the residuals calculated from the Eulerian components, thus a simple relation like (1.3) does not apply to the case in which the residual Eulerian velocity field varies rapidly over the length of the tidal excursion.

The true complexity of the relationship between the Eulerian and Lagrangian flow fields was illuminated by Aref (1984), who demonstrated that Lagrangian motion in two-dimensional incompressible flow which varies in time is a Hamiltonian dynamical system that may be non-integrable even for simple flows. The particle trajectories, therefore, may become chaotic functions of time. Such a flow results in a diffusion process over scales large compared to the scale of the fluctuations, even though the Eulerian flow field is completely deterministic. Pasmanter (1988) superposed oscillatory and mean tidal components varying sinusoidally in space and showed that patches of particles released in the flow were characterized by "anomalous diffusion". Anomalous refers to the fact that the patches spread at rates both faster and slower than linearly with time, depending sensitively upon the parameter settings. The concentration field also tended to be patchy, with "islands" of unmixed

particles interspersed with well-mixed regions.

More evidence for dispersion in deterministic flow was demonstrated by Awaji et al. (1980), who obtained particle spreading rates by integrating the Eulerian output from a numerical model of tidal flow through a narrow strait. From the growth in variance of the particle releases, they determined effective diffusivities, which were shown to vary by more than an order of magnitude over a tidal excursion. Cheng and Casulli (1982) pointed out that the diffusivities should be a strong function of the tidal phase at initial release of the particles, as well as initial position. In Chapter 5, it will be shown that for separating tidal flow around headlands, the Eulerian mean flow has no relationship to Lagrangian residual displacements, and that dispersion caused by the deterministic tidal currents leads to mixing that cannot be represented by Gaussian diffusion.

1.3 Thesis objectives

This thesis is aimed at understanding the tidal dynamics and dispersion around headlands in shallow water, where the tidal currents vary strongly over the scale of the tidal excursion. Bathymetric variation is dominated by a shoaling region along the boundary that is narrow compared to the scale of the headland, since it is the effects of coastline variation that are of interest. These conditions pertain to a large number of typical headlands in shallow coastal waters, such as those studied by Tee (1977) in the Bay of Fundy, Pingree (1978) in the English Channel, and Wolanski et al. (1984) on the northeast coast of Australia.

In Chapter 2, the approximations associated with a 2-D representation of the governing equations are discussed, and a numerical model is developed to solve these equations. The numerical model represents the nonlinear depth-averaged shallow-water equations in orthogonal curvilinear coordinates, which effectively eliminates the spurious numerical input of vorticity from coastline discretization. In addition, the high resolution in the vicinity of the headland tip allows the boundary layer and the free shear layer associated with flow separation to be accurately represented.

In Chapter 3, a case study of tidal flow around a headland is described in detail. Using parameters that typify the class of headland described above, snapshots of the flow fields, time series at specific locations, harmonic constituents, and Eulerian and Lagrangian vortic-

ity balances are all described to build intuition regarding the flow separation and transient eddy formation which typify these highly nonlinear flows. Insight into the observed flow structures is obtained by considering the generation, advection and dissipation of relative vorticity.

In Chapter 4, the important parameters controlling the nature of the flow are identified by an idealized model of flow separation and consideration of vorticity transport and damping in the interior. Numerical simulations are then performed to investigate the dependence of the solutions on these parameters. The remainder of the chapter discusses the the strength and detailed structure of the wake generated by tidal flow past the headland and how the headland wake compares to wakes found in laboratory studies of viscous oscillatory flow around circular cylinders.

In Chapter 5, the tide-induced dispersion of material around headlands is investigated. The basic mechanism by which mixing takes place is investigated, then experiments are carried out which describe the spreading of material over multiple tidal cycles, emphasizing the difference between the observed mixing and the gradient-type diffusion that is commonly applied in transport modeling. Finally the sensitivity of dispersion to the parameters that control the nature of the tidal flow is discussed.

Chapter 6 summarizes the thesis and presents conclusions from this research.

Chapter 2

Model Equations and Numerical Techniques

2.1 Introduction

The governing model equations used in this study are the depth-averaged shallow-water equations, which express mass and momentum conservation for shallow tidal flows in which vertical structure is not of dominant importance. In the first part of this chapter, these equations are obtained by depth-averaging the three-dimensional shallow-water equations. This illustrates the assumptions inherent in the simpler two-dimensional equations. Some differences between 2-D and 3-D formulations are then discussed for the problem of tidal dynamics around headlands. In the second part of this chapter the numerical solution of the depth-averaged shallow-water equations is discussed. Solutions are obtained using a finite-difference method on a orthogonal curvilinear grid. The use of the curvilinear grid allows the coastline to be smoothly represented and allows high resolution near the headland tip, where flow separation and transient eddy formation occur.

2.2 Model equations

2.2.1 Depth-averaging the shallow-water equations

The three-dimensional shallow-water equations describe the nearly horizontal motions that occur in a thin layer of rotating fluid. Vertical accelerations are neglected, which eliminates short wavelength motions such as wind waves. The horizontal momentum equation in the absence of density gradients can be expressed as

$$\frac{\partial \mathbf{u}_h}{\partial t} + \mathbf{u} \cdot \nabla \mathbf{u}_h + w \frac{\partial \mathbf{u}_h}{\partial z} + f(\hat{\mathbf{k}} \times \mathbf{u}_h) = -g\nabla\eta + \nabla \cdot (A_H \nabla \mathbf{u}_h) + \frac{\partial}{\partial z} \left(A_v \frac{\partial \mathbf{u}_h}{\partial z} \right) \quad (2.1)$$

where \mathbf{u}_h denotes the horizontal velocity vector, w the vertical velocity component, η the free-surface elevation, f the Coriolis parameter, g the gravitational acceleration, and $\hat{\mathbf{k}}$ the vertical unit vector acting upward. The turbulent Reynolds stresses are parameterized by horizontal and vertical eddy viscosities A_H and A_v .

Mass conservation for an incompressible fluid can be expressed

$$\nabla \cdot \mathbf{u}_h + \frac{\partial w}{\partial z} = 0. \quad (2.2)$$

Derivation of these equations and a detailed discussion of the implicit assumptions can be found in textbooks such as Batchelor (1967) or Gill (1982).

In the absence of wind stress, surface and bottom boundary conditions can be expressed as

$$\tau_s = A_v \frac{\partial \mathbf{u}_h}{\partial z} = 0 \quad \text{at} \quad z = \eta, \quad (2.3)$$

$$\tau_b = A_v \frac{\partial \mathbf{u}_h}{\partial z} = C_d \mathbf{u}_h |\mathbf{u}_h| \quad \text{at} \quad z = -h + z_r, \quad (2.4)$$

where h is the water depth and z_r is some reference height above the bottom below which the stress varies little (typically 1 m). C_d is the drag coefficient for the flow at z_r , which in the simplest scenario of steady flow over a rough bed, is only a function of the physical bed roughness. In this case, the quadratic drag law parameterizes the experimentally determined “law-of-the-wall” logarithmic velocity profile

$$\mathbf{u} = \frac{u_*}{\kappa} \ln \left(\frac{h+z}{z_o} \right) \quad (2.5)$$

where u_* is the friction velocity defined by

$$\tau_b = \rho u_* |u_*|, \quad (2.6)$$

z_o is the bottom roughness height, and κ is von Karman's constant (≈ 0.4).

The equations (2.1–2.2), with boundary and initial conditions, determine the elevation and the three-dimensional structure of nearly horizontal flow. Solution of these equations in regions of strong nonlinearity and rapidly varying coastline, however, requires a 3-D numerical modeling approach of considerable complexity. The development and understanding of 3-D circulation models is a active area of current research (see collections edited by Heaps, [1987] and Nihoul, [1987]).

The governing equations can be greatly simplified if vertical shear effects are neglected. This is a reasonable approximation if the vertical mixing time scale is considerably less than the tidal period. From solving the vertical diffusion equation, the time scale for complete vertical mixing (10% variation from the mean) of a perturbation introduced at the boundary is $0.4h^2/A_v$, where A_v is the characteristic vertical eddy viscosity (Fischer et al., 1979). Choosing A_v as the mean value of the parabolic eddy viscosity profile that is consistent with the law-of-the-wall velocity profile (2.5) yields the result that $A_v = 0.07u_*h$. From (2.6), $u_* = \sqrt{C_D}|\bar{u}|$. Combining these results leads to an expression for the vertical mixing time

$$T_{vm} = \frac{0.4h^2}{A_v} \approx \frac{0.4h^2}{0.07u_*h} = \frac{5.7h}{\sqrt{C_D}\bar{u}}. \quad (2.7)$$

For values typical of a vigorous shallow tidal flow, $C_D = 2.5 \times 10^{-3}$, $h = 20$ m, and $\bar{u} = 1$ m s⁻¹ resulting in a vertical mixing time of $T_{vm} = 0.5$ hours. Since this is much smaller than the tidal time scale, the assumption that the properties are well-represented by the depth-averaged flow is a reasonable approximation if the tidal currents are moderate and the depth is not too great.

If vertical structure is not important, the simpler physics can be represented by integrating (2.1–2.2) over the water column. If the equations are then divided by depth, the depth-averaged shallow-water equations are obtained:

$$\frac{\partial \bar{\mathbf{u}}}{\partial t} + \bar{\mathbf{u}} \cdot \nabla \bar{\mathbf{u}} + f(\hat{\mathbf{k}} \times \bar{\mathbf{u}}) = -g\nabla\eta - \frac{C_D \bar{\mathbf{u}}|\bar{\mathbf{u}}|}{h + \eta} + \nabla \cdot (A_H \nabla \bar{\mathbf{u}}), \quad (2.8)$$

$$\frac{\partial \eta}{\partial t} + \nabla \cdot [\bar{\mathbf{u}}(h + \eta)] = 0, \quad (2.9)$$

where $\bar{\mathbf{u}}$ is the depth-averaged velocity defined by

$$\bar{\mathbf{u}} = \frac{1}{h + \eta} \int_{-h}^{\eta} \mathbf{u}_h dz, \quad (2.10)$$

and C_D is a depth-averaged drag coefficient.

2.2.2 Differences between 2-D and 3-D

In the 2-D representation of tidal flow, vertical shear effects cannot be modeled, and the bottom stress must be expressed in terms of the depth-averaged flow. Therefore, rotation and phase change of the tide with depth, cannot be represented. For the typical water depths (10–40 m) and flow speeds (0.25–1.0 m s⁻¹) in this study, however, these effects will be shown to be negligible.

From the full shallow-water equations (2.1–2.2) it can be seen that the bottom stress depends on the near-bottom flow, while in the depth-averaged form (2.8–2.9) the bottom stress must be expressed in terms of the depth-averaged flow and a depth-averaged drag coefficient C_D . Equating these two stress parameterizations

$$C_d |\mathbf{u}_h(-h + z_r)| \mathbf{u}_h(-h + z_r) = C_D |\bar{\mathbf{u}}| \bar{\mathbf{u}} \quad (2.11)$$

contains the implicit assumption that the phase and direction differences between the depth-averaged current and the bottom current are small and that the magnitudes of the two currents are proportional. In essence, it is assumed that the law-of-the-wall (2.5) holds over the entire water column. Integrating (2.5) over depth leads to an expression for C_D

$$C_D = \frac{\kappa^2}{[\ln(h/z_o) - 1]^2} \quad (2.12)$$

that depends on the ratio h/z_o . Typically, however, a constant C_D is used, the implied assumption being that either the roughness height scales linearly with water depth, or that the bottom boundary layer is so poorly represented that a more complicated function than a constant is not warranted.

The deficiency of the 2-D model in representing the difference in angle between the depth-averaged flow and the bottom stress is a potential problem for tidal flow around

headlands. If the momentum balance in the bulk of the water column has a significant contribution from Coriolis or centrifugal effects, then the pressure gradient will have a component orthogonal to the depth-averaged flow. Near the bottom, this component of pressure gradient drives a down-gradient flow, since the stress divergence balances the pressure gradient where vertical mixing is large. This is reflected at the headland tip, where the onshore pressure gradient that accelerates the bulk of the flow around the tip of the headland also drives a secondary onshore current near the bottom. This flow has been suggested as a possible upwelling mechanism in tidal flows around headlands (Garrett and Loucks, 1976). Another source of secondary circulation is eddies shed from headlands. These eddies are characterized by a depression in elevation at the eddy core, which leads to convergent flow at the bottom and upwelling in the center (Wolanski, 1984).

The generation of secondary currents induced by centrifugal and Coriolis effects in shallow water is reviewed by Kalkwijk and Booij (1986). In the simplest case of a steady logarithmic streamwise velocity profile (2.5) and a parabolic vertical eddy viscosity distribution consistent with this profile, the secondary flow profiles are given by

$$u_n = -\text{sign}(\bar{u}_s) \frac{fh}{2\kappa^2} G_1 \left(\frac{z}{h}, \frac{h}{z_0} \right) \quad (2.13)$$

and

$$u_n = \frac{|\bar{u}_s|h}{\kappa^2 r_c} G_2 \left(\frac{z}{h}, \frac{h}{z_0} \right) \quad (2.14)$$

for the Coriolis and centrifugal effects respectively. In these expressions, \bar{u}_s is the depth-averaged streamwise flow, u_n is the secondary flow normal to the stream, and r_c is the radius of curvature. G_1 and G_2 are vertical structure functions that are weakly dependent on h/z_0 , or equivalently, the depth-averaged drag coefficient C_D (2.12). For a realistic range of C_D their amplitude is order one, and their shape is shown in Figure 2-1. These results apply to shallow tidal flow around headlands when the bottom friction is strong enough that the vertical mixing time scale (2.7) is significantly less than the tidal period.

Examining the expression for secondary flow due to the Coriolis effect (2.13), it is seen that the magnitude does not depend on the magnitude of the streamwise flow, but on its sign only. At a given latitude, in fact, the magnitude of the cross-stream flow due to the Coriolis effect essentially depends only on the water depth h . This seemingly odd result arises from

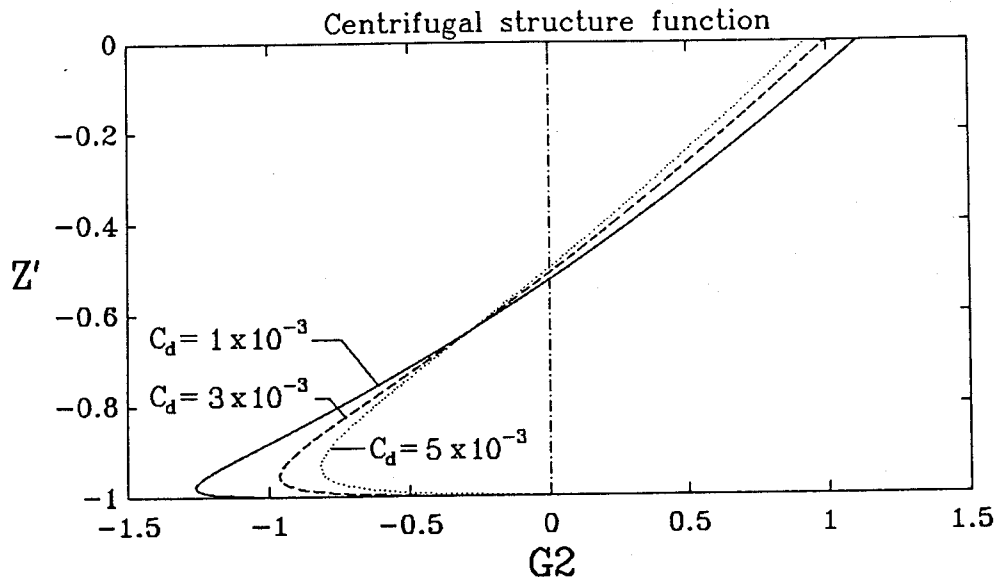
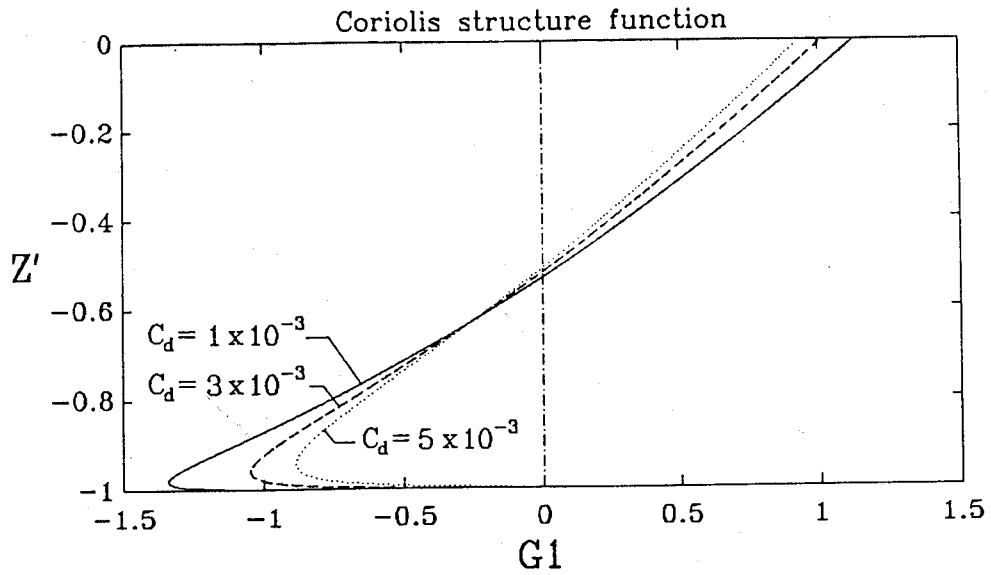


Figure 2-1: (a) The vertical structure function G_1 of the secondary flow induced by Coriolis effects acting on a logarithmic streamwise flow. (b) The vertical structure function G_2 induced by curvature effects. Three profiles are shown are different values of the depth-averaged drag coefficient C_D .

the fact that in shallow water, the eddy viscosity, the cross-stream components of pressure gradient, and bottom stress all depend linearly on the depth-averaged streamwise velocity. For depths of 10–40 m (the depth range of interest in this study) and $f = 1 \times 10^{-4} \text{ s}^{-1}$, the magnitude of the Coriolis-induced secondary flow varies from 0.3–1.2 cm s^{-1} , and is therefore negligible compared to the residual flow due to variations in the coastline, which is shown in Chapter 3 to be an order of magnitude larger.

The magnitude of the secondary flow associated with centrifugal effects (2.14) depends linearly on the depth-averaged streamwise velocity, with a proportionality factor of $(h/\kappa^2 r_c) \approx (6h/r_c)$. Since the secondary flow has the same sign regardless of the streamwise flow direction, reversing flow past a bend in the coastline will drive a non-zero mean when averaged over a tidal cycle. For tidal circulation in bays, the generated residual flow will be weak except in very localized areas, since typically $[h/r_c] < 10^{-2}$. For example, an average tidal speed of 50 cm s^{-1} in 10 m water depth, for $r_c = 1 \text{ km}$, will result in a secondary current of 3.1 cm s^{-1} . This is much smaller than the horizontal residual currents induced by variation in the coastline for these tidal conditions, as will be shown in Chapters 3 and 4. Curvature-induced secondary flow becomes more important as $[h/r_c]$ increases, and it is an extremely important effect in rivers.

Another important difference between the 2-D and 3-D representations results from the vertical integration of the nonlinear advective terms. The horizontal flow vector can be decomposed as

$$\mathbf{u}_h(x, y, z, t) = \bar{\mathbf{u}}(x, y, t) + \mathbf{u}'(x, y, z, t), \quad (2.15)$$

where $\mathbf{u}'(x, y, z, t)$ represents the departure of the current from the depth-averaged value. Integrating the advective component in the x -momentum equation results in

$$\int_{-h}^{\eta} u \frac{\partial u}{\partial x} + v \frac{\partial u}{\partial y} dz = \bar{u} \frac{\partial \bar{u}}{\partial x} + \bar{v} \frac{\partial \bar{u}}{\partial y} + \frac{1}{h + \eta} \left\{ \frac{\partial}{\partial x} [(h + \eta) \overline{u'^2}] + \frac{\partial}{\partial y} [(h + \eta) \overline{u'v'}] \right\}. \quad (2.16)$$

The ratio of the vertically varying contribution to the depth-mean momentum flux is order $[U'^2/\bar{U}^2]$, where \bar{U} is the scale of the depth-averaged flow, and U' is the scale of the shear. For tidal flows in shallow water, the vertical structure is nearly logarithmic (Fischer et al., 1979), so U'^2 averaged over the water depth is much smaller than U^2 . Small-scale phenomena such as the effect of a vertical wake generated by a large boulder, however,

cannot be represented by a depth-averaged formulation.

2.3 Numerical techniques

2.3.1 Eulerian flow modeling

The solution of the nonlinear depth-averaged shallow-water equations (2.8–2.9) for arbitrary geometry requires a numerical approach. Most schemes that have been devised discretize the spatial derivatives on a grid or mesh, and calculate the solution forward in time from a specified initial condition. The model developed here is an explicit time-stepping finite difference method based on the the scheme of Flather and Heaps (1975). The Flather and Heaps scheme is simple to implement, and it has a number of attractive features: (1) when applied to the linearized equations, all derivatives are centered in space and time, the truncation error is $O(\Delta t^2, \Delta x^2)$, and there is no numerical damping; (2) since it is a two-level scheme in time, there is no computational mode (a purely numerical wave which is present in three-level time schemes); (3) the model has been used successfully by many investigators in shallow tidal flow (Choi, 1980; Uncles, 1982), and the predicted tide-induced residual circulation compares well to observations (Pingree, 1978). The scheme is described in more detail in Appendix A.

The scheme was modified in the following ways:

1. Orthogonal curvilinear coordinates were used instead of Cartesian coordinates so that the spatial mesh could conform smoothly to variations in the coastline;
2. Horizontal momentum diffusion terms were included to represent sub-grid scale turbulence;
3. A filtering procedure was implemented to remove spurious high wavenumber components ($2-6\Delta x$);
4. Open boundary conditions were modified to allow gravity wave radiation;
5. A time-splitting version of the code was developed to take advantage of the different time scales of advection, gravity wave propagation and diffusion.

Most of the numerical techniques are fairly standard and are described in detail in Appendix A. The orthogonal curvilinear coordinates deserve special mention, however.

It has been known for some time that when a smoothly varying coastline is represented by rectangular grid elements, spurious vorticity is introduced into the domain due to numerical difficulties at the corners of the boundary elements (Abbott et al., 1985). In these models, residual circulation is generated even when the governing equations are devoid of vorticity generating mechanisms. In orthogonal curvilinear coordinates this problem is avoided because of the smooth representation of curved coastlines. In addition, a considerable degree of flexibility exists in controlling the grid resolution throughout the domain, which allows high resolution of the strong gradients in the flow that occur near the headland tip. Unlike generalized curvilinear coordinates (e.g. Spaulding, 1984), orthogonal coordinates maintain much of the simplicity of Cartesian coordinates in that no additional derivatives of the dependent variables (u, v, η) are introduced. This means that the large literature concerning finite difference methods on rectangular grids (see for example books by Roache, [1976] and Anderson et al., [1984]) can be applied in a straightforward way to orthogonal curvilinear coordinates.

If the orthogonal curvilinear coordinates are defined by (x_1, x_2) and the physical coordinates by (x, y) , then

$$dx^2 + dy^2 = (s_1 dx_1)^2 + (s_2 dx_2)^2, \quad (2.17)$$

where s_1 and s_2 are metric factors given by

$$s_1^2 = \left(\frac{\partial x}{\partial x_1} \right)^2 + \left(\frac{\partial y}{\partial x_1} \right)^2 \quad (2.18)$$

and

$$s_2^2 = \left(\frac{\partial x}{\partial x_2} \right)^2 + \left(\frac{\partial y}{\partial x_2} \right)^2. \quad (2.19)$$

With these definitions, the x_1 and x_2 momentum equations in curvilinear coordinates are (see Anderson et al., 1984)

$$\begin{aligned} & \frac{\partial u_1}{\partial t} + \frac{u_1}{s_1} \frac{\partial u_1}{\partial x_1} + \frac{u_2}{s_2} \frac{\partial u_1}{\partial x_2} + \frac{u_1 u_2}{s_1 s_2} \frac{\partial s_1}{\partial x_2} - \frac{u_2^2}{s_1 s_2} \frac{\partial s_2}{\partial x_1} - f u_2 \\ &= -\frac{g}{s_1} \frac{\partial \eta}{\partial x_1} - \frac{C_D u_1 \sqrt{u_1^2 + u_2^2}}{h + \eta} + \frac{A_H}{s_1 s_2} \left[\frac{\partial}{\partial x_1} \left(\frac{s_2}{s_1} \frac{\partial u_1}{\partial x_1} \right) + \frac{\partial}{\partial x_2} \left(\frac{s_1}{s_2} \frac{\partial u_1}{\partial x_2} \right) \right] \end{aligned} \quad (2.20)$$

$$\begin{aligned} & \frac{\partial u_2}{\partial t} + \frac{u_1}{s_1} \frac{\partial u_2}{\partial x_1} + \frac{u_2}{s_2} \frac{\partial u_2}{\partial x_2} + \frac{u_1 u_2}{s_1 s_2} \frac{\partial s_2}{\partial x_1} - \frac{u_1^2}{s_1 s_2} \frac{\partial s_1}{\partial x_2} + f u_1 \quad (2.21) \\ = & -\frac{g}{s_2} \frac{\partial \eta}{\partial x_2} - \frac{C_D u_2 \sqrt{u_1^2 + u_2^2}}{h + \eta} + \frac{A_H}{s_1 s_2} \left[\frac{\partial}{\partial x_1} \left(\frac{s_2}{s_1} \frac{\partial u_2}{\partial x_1} \right) + \frac{\partial}{\partial x_2} \left(\frac{s_1}{s_2} \frac{\partial u_2}{\partial x_2} \right) \right] \end{aligned}$$

where A_H has been assumed constant.

The continuity equation becomes

$$\frac{\partial \eta}{\partial t} + \frac{1}{s_1 s_2} \left\{ \frac{\partial}{\partial x_1} [s_2 u_1 (h + \eta)] + \frac{\partial}{\partial x_2} [s_1 u_2 (h + \eta)] \right\} = 0. \quad (2.22)$$

The model domain has closed boundaries at the north and south, and open boundaries at the east and west. The headland is at the center of the southern boundary. Along the closed boundaries, the normal velocity u_2 is set to zero at the wall, which ensures no mass flux at the wall. At the western open boundary, the tide is forced by an oscillatory current and at the eastern boundary the tidal wave is allowed to propagate out of the domain via a simple gravity wave radiation condition. See Appendix A for more details.

The model is started from a state of rest and is run for multiple tidal cycles until periodic conditions are obtained (taken to be $< 5\%$ velocity differences between successive tidal cycles at the headland tip). The number of cycles required to reach equilibrium depends on the level of bottom friction and horizontal viscosity, typically 2 to 6 cycles for the cases in this study.

2.3.2 Lagrangian flow modeling

The Lagrangian velocity and water parcel (or passive particle) trajectories are calculated by spatial interpolation and time integration of the Eulerian velocity field obtained by the model. First the Lagrangian velocity at the particle location is determined by bilinearly interpolating the Eulerian velocity field. Bicubic interpolation was also tried, but did not result in significant differences in particle trajectories. With the velocity field specified in space by interpolation, the particle positions are advanced in time using a 4th order Runge-Kutta integration scheme. The time step is constrained so that particles move less than 1 grid cell per time unit, which results in time steps of 1–5 minutes for the flows considered in this study.

The effects of sub-gridscale turbulence on particle motion are simulated by using a random-walk Markov-chain model whereby the particle velocity is perturbed at each time step by a random fluctuation corresponding to a specified level of diffusivity. In this way, a level of diffusivity that parameterizes three-dimensional bottom-generated tidal turbulence can be represented in the motion of the particles. Details of the Markov-chain model can be found in Awaaji (1982).

2.4 Summary

Depth-averaged dynamics are appropriate when vertical mixing is strong enough to prevent large phase variation and rotation of the tidal current with depth. This condition is met for vigorous tidal flows ($0.25\text{--}1.0\text{ m s}^{-1}$) in shallow water (10–40 m). In regions of rapidly varying coastline and bathymetry, the horizontal momentum advection terms are of critical importance, and the equations must be solved numerically using a nonlinear model. A numerical model has been developed based on the methods of Flather and Heaps (1975), but transformed to an orthogonal curvilinear coordinate system. The curvilinear coordinates allow smooth representation of the coastline as well as high resolution around the headland tip. This avoids the spurious vorticity input generated by rectangular grids at rapid changes in the coastline (Abbott, 1985).

Chapter 3

Tidal Flow Around a Gaussian Headland

3.1 Introduction

To illustrate the basic nature of strongly nonlinear flow around a headland, this chapter presents a detailed analysis of the tidal flow around a Gaussian headland that is characterized by flow separation and transient eddy formation. This case is referred to as Case A.

Snapshots of the elevation, velocity, and vorticity fields at several phases of the tidal cycle are presented, together with flow visualization of a line of floats initially released along the boundary of the headland. The snapshots clearly indicate that during each phase of the tide, the flow separates near the headland tip and an eddy forms on the downstream side. Vorticity emerges as a natural descriptor of the formation and evolution of these eddies.

Time series of elevation, velocity and vorticity at several fixed locations show that the tidal flow can be divided into three regions: a narrow layer along the headland where vorticity is produced, a region near the headland where vorticity advected from the headland influences the flow, and a region further from the headland where vorticity is negligible.

Harmonic decomposition of the tidal fields shows that much of the signal is contained in the M_2 , mean and M_4 constituents. The M_2 is the fundamental frequency and the mean and the M_4 are the nonlinearly generated constituents that result from M_2 - M_2 interaction. The

magnitudes of the mean and M_4 constituents are comparable to the M_2 near the headland, reflecting the strong nonlinearity of the flow.

Examination of the vorticity balance shows that the transient eddy formation can be described by production of vorticity in a narrow layer along the headland, injection of vorticity into the interior at the point of flow separation, and damping of vorticity by bottom friction.

3.2 Input parameters

The parameters for Case A were selected to characterize the geometry and tidal conditions at Gay Head, Massachusetts, where high resolution measurements of the spatial current structure have been obtained with an Acoustic Doppler Current Profiler (Geyer and Signell, 1989). The tidal currents around Gay Head vary from 0.3 to 0.8 m s⁻¹, the depth ranges from 10–30 m, and the headland scales are comparable to the tidal excursion of 5-10 km. Headlands with similar attributes are common in coastal waters (Pingree, 1978; Wolanski et al. 1984). The tidal flows around these headlands are typically highly asymmetric and nonlinear, with strong variation in the tidal currents, transient eddy formation, and large residual and harmonic current components.

The model geometry is shown in Figure 3-1. A Gaussian headland for the coastline is specified according to the equation

$$\zeta(x) = b \exp \left[-\frac{1}{2} \left(\frac{x}{a} \right)^2 \right]. \quad (3.1)$$

where ζ is the coastline position, $a = 2$ km defines the length (or alongshore extent), and $b = 8$ km defines the width (or offshore extent). The domain is 50 km long and 25 km wide, which with a 60 by 30 grid results in a minimum grid spacing of 53 m at the tip of the headland and a maximum grid spacing of 1.8 km in the northwest and northeast corners. The depth increases linearly northward away from the southern boundary, from 1 m at the coast to 20 m at a distance of 3 km from the boundary. The basin has a constant depth of 20 m elsewhere. The western boundary is forced by a normal depth-averaged velocity that varies sinusoidally with an amplitude of 0.5 m s⁻¹ and a M_2 tidal period of 12.42 hours (12

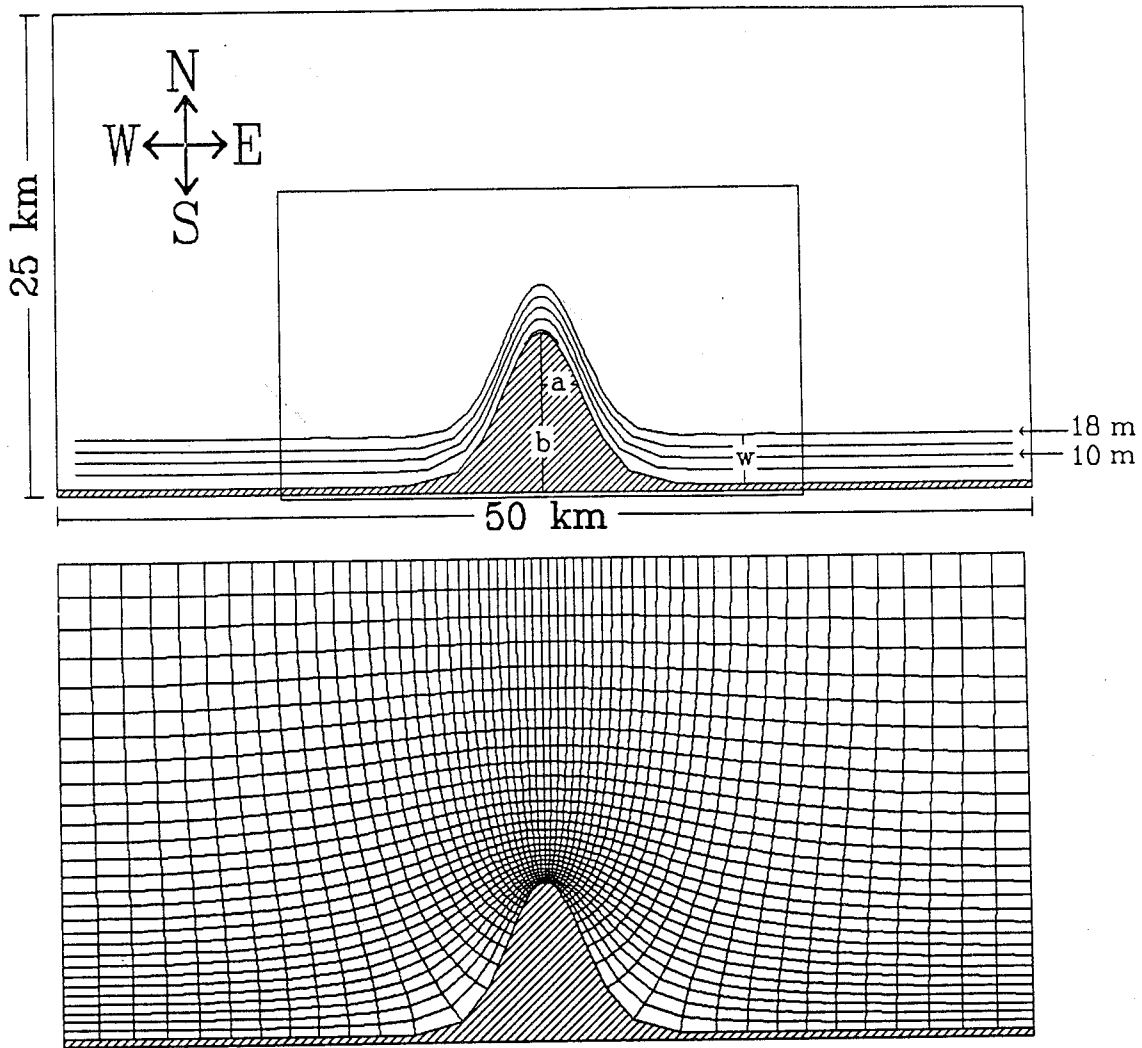


Figure 3-1: Model geometry and numerical grid for Case A. The top panel shows contours of the model bathymetry at intervals of 4 m. The depth along the southern boundary increases linearly to the north, reaching a depth of 20 m in 3 km. The interior of the basin has a constant depth of 20 m. The enclosed region near the headland indicates the sub-domain that will be presented in succeeding plots of results. The bottom panel shows the 60×30 curvilinear orthogonal grid used in the study. The basin is 50 km long, 25 km wide and the minimum spacing between grid points is 53 m at the tip of the headland.

lunar hours). The eastern boundary radiates gravity waves. The Coriolis parameter was fixed at $f = 1 \times 10^{-4} \text{ s}^{-1}$.

In realistic simulations, the inputs that are least well known are the bottom friction and the horizontal eddy viscosity, as they parameterize processes that are not resolved by the model physics. In general, they may be functions of time and space, but in the interest of simplicity they will be considered constant in this study. For Case A, the drag coefficient was chosen as $C_D = 2.5 \times 10^{-3}$, a value commonly used in shallow water tidal and storm surge models (Heaps, 1978). If the law-of-the-wall log profile is assumed, then this choice of depth-averaged drag coefficient, using (2.12), corresponds to a roughness length of $z_0 = 0.25 \text{ cm}$ at 20 m depth. With the grid resolution of the model, the horizontal eddy viscosity represents only the momentum transfer due to bottom-generated tidal turbulence. From gathered observations, Zimmerman (1986) concluded that in water depths up to 30 m and current speeds in the range of $0.75\text{--}1.50 \text{ m s}^{-1}$, the horizontal viscosity is $0.1\text{--}1 \text{ m}^2 \text{ s}^{-1}$. This roughly agrees with the empirical formula $A_H = 0.2u_*h$ of Fischer et al. (1979). For a drag coefficient $C_D = 2.5 \times 10^{-3}$, the ratio of the shear velocity to the depth-averaged current is $u_*/\bar{u} = 0.05$, therefore a 1 m s^{-1} current (a characteristic flow speed near the headland) in 20 m water yields a value of $0.2 \text{ m}^2 \text{ s}^{-1}$ for the horizontal eddy viscosity. Using the upper bound of these estimates, the eddy viscosity was fixed at $A_H = 1 \text{ m}^2 \text{ s}^{-1}$.

3.3 Elevation, velocity and vorticity fields

3.3.1 Snapshots over a tidal cycle

The nature of the flow is perhaps best illustrated by snapshots of elevation, velocity and vorticity fields at several phases of the tidal cycle. In this section, snapshots over the first half cycle will be described, where the start of the tidal cycle is defined as the time of slack water at the western open boundary, just before eastward flow commences. In addition, flow separation and eddy formation are visualized by following a line of numerical floats released at the beginning of the previous half cycle in a x_1 -directed line located $1/10$ of a grid spacing above the coastline of the headland. In the subsequent discussion lunar hours are referred to simply as hours.

At the beginning of the tidal cycle ($t = 0$ hours), the surface slopes downwards to the east, exerting an eastward force over most of the domain (Figure 3-2a). The only exception is a slight local depression to the west of the headland tip, associated with a counterclockwise eddy that is seen in the velocity field (Figure 3-2b). This eddy was formed on the previous half cycle of westward flow, and near the coast this eddy has caused early reversal of the flow, evidenced by the 0.5 m s^{-1} eastward flow between the eddy and the headland. The eddy is also revealed in the vorticity field (Figure 3-2c). The maximum vorticity ($11 \times 10^{-4} \text{ s}^{-1}$) is located at the center of the eddy, and the eddy is attached by a thin band of vorticity to the eastern side of the headland. There is also a strip of negative vorticity along the western side of the headland, associated with the boundary shear of the eastward flow. The floats released at the beginning of the previous half cycle spiral into the eddy, with the end of the float line located at the eddy center (Figure 3-2d).

One hour after the start of the cycle, the surface still slopes downwards to the east, and has a magnitude similar to that at the start of the cycle (Figure 3-3a). Along the headland, however, the eastward pressure gradient is very strong on the western side of the headland and weak on the eastern side. The flow is strongest near the tip as the flow accelerates around the headland, and a local minimum in pressure occurs due to the Bernoulli effect (Figure 3-3b). The flow has a strong offshore component at the tip, with the result that the flow along the lee side of the headland is weak, and the pressure gradient is very weak. The vorticity field shows a region of very large negative vorticity ($-25 \times 10^{-4} \text{ s}^{-1}$) along the boundary just upstream of the tip, and the vorticity of the counter-clockwise eddy has decreased to $7 \times 10^{-4} \text{ s}^{-1}$ (Figure 3-3c).

At maximum eastward flow ($t = 3$ hours), the pressure gradient offshore is still directed eastward but has decreased in strength (Figure 3-4a). The pressure gradient along the boundary upstream of the tip has intensified, however, and there is now a distinct pressure minimum at the tip, after which the pressure gradient is directed westward. The flow upstream of the tip smoothly increases in speed as the tip is approached, but at the tip, it separates from the coast and an eddy is evident on the downstream side of the headland (Figure 3-4b). The vorticity of the counterclockwise eddy has diminished to $1 \times 10^{-4} \text{ s}^{-1}$, while the strip of high negative vorticity now extends across the sloping region into the

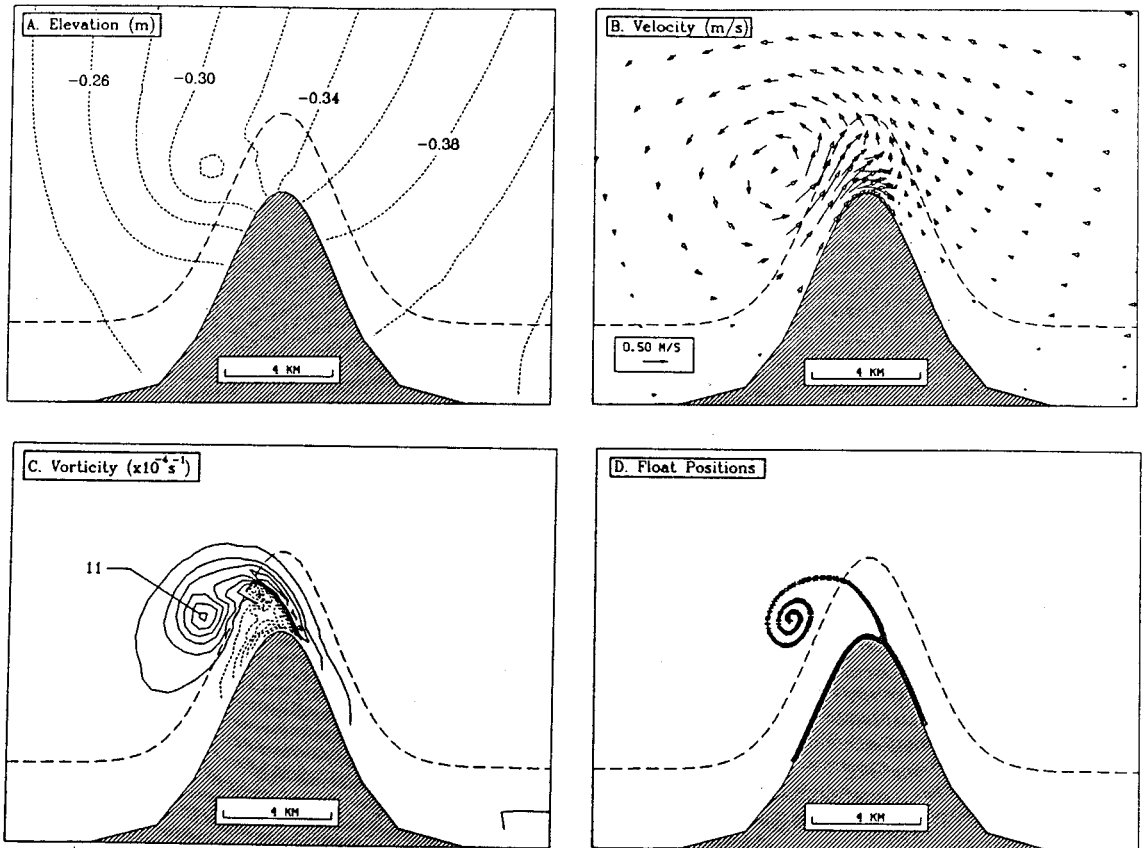


Figure 3-2: The modeled tide at 0 lunar hours. (a) Elevation contoured at intervals of 0.02 m. (b) Depth-averaged velocity vectors (plotted every other grid point). (c) Depth-averaged relative vorticity ($\times 10^{-4} \text{ s}^{-1}$). The solid contours indicate positive vorticity, the dashed lines indicate negative vorticity and the contour interval is $2 \times 10^{-4} \text{ s}^{-1}$. (d) Location of floats initially released in a x_1 -directed line along the headland at the beginning of the previous half cycle (six hours previous to the start of the cycle).

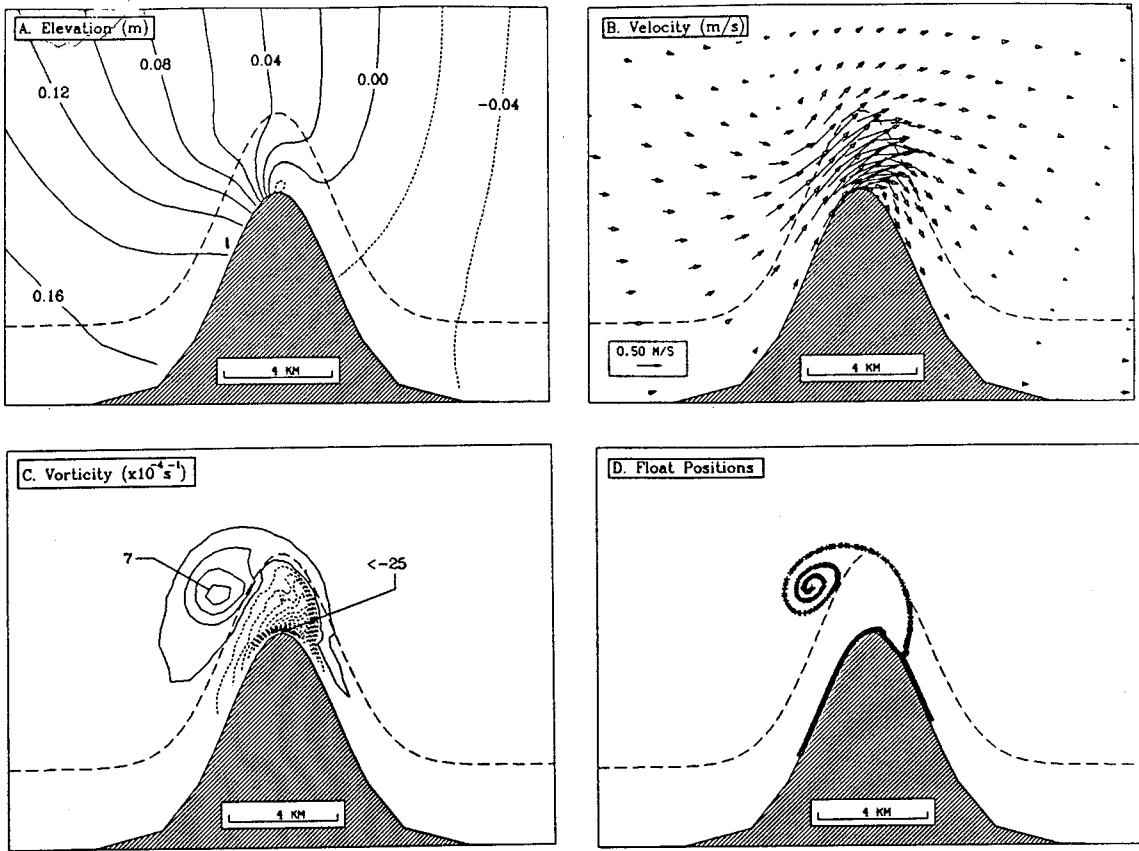


Figure 3-3: The modeled tide at 1 lunar hour. Panels as in Figure 3-2.

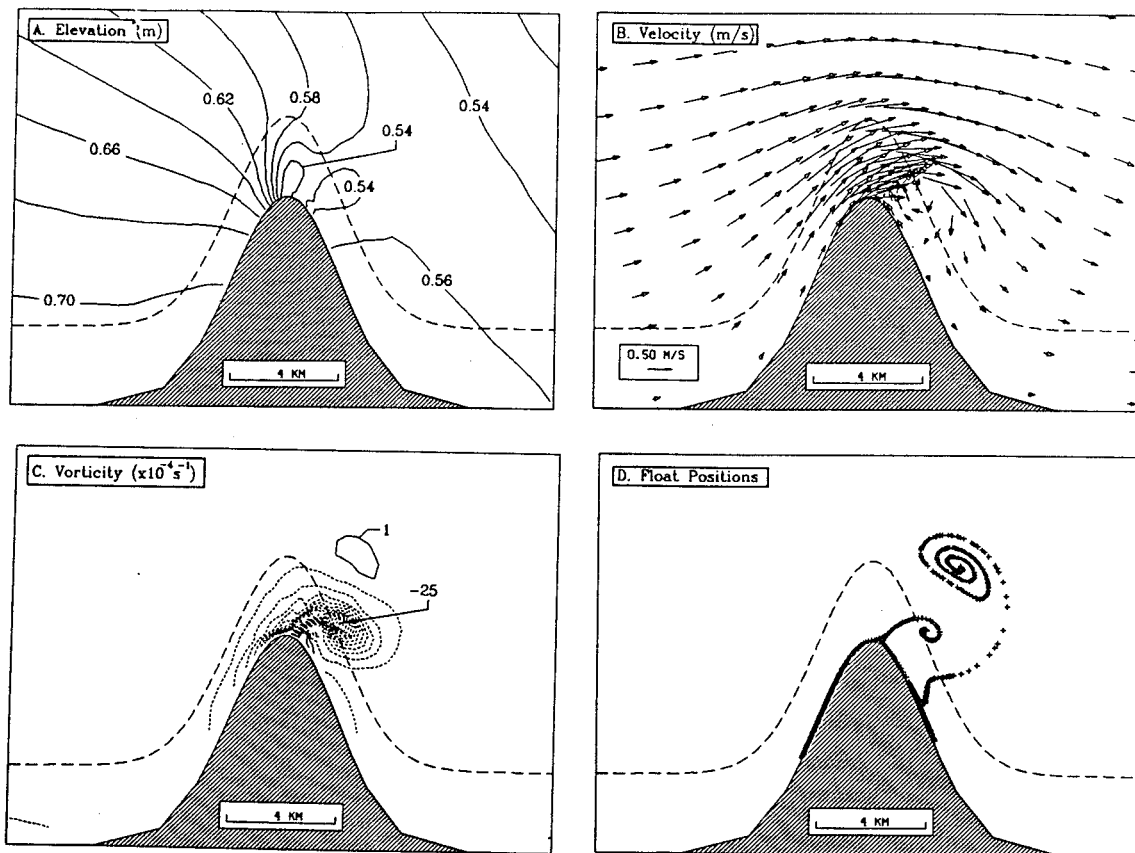


Figure 3-4: The modeled tide at 3 lunar hours. Panels as in Figure 3-2.

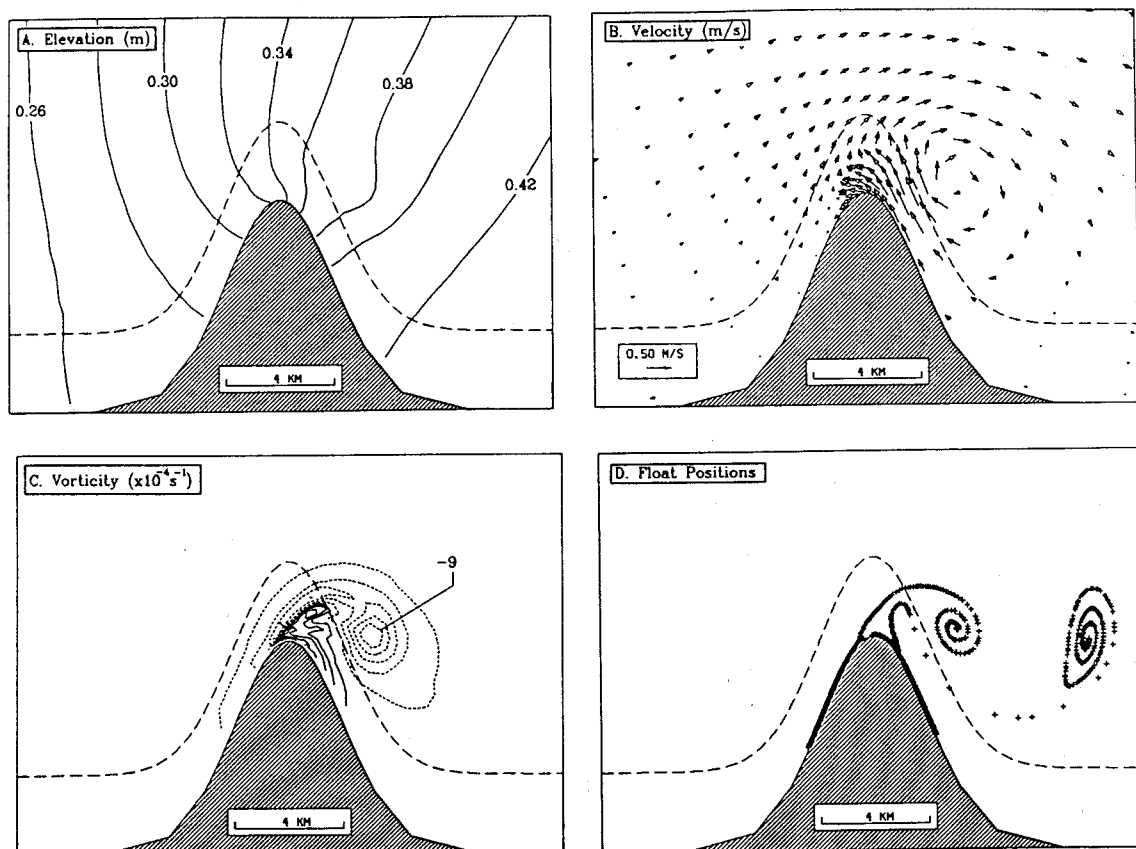


Figure 3-5: The modeled tide at 6 lunar hours. Panels as in Figure 3-2.

interior (Figure 3-4c). The tip of the high negative vorticity strip is beginning to curl up in the clockwise direction. This process concentrates vorticity in a blob, which marks the center of the clockwise eddy. The maximum vorticity magnitude is $25 \times 10^{-4} \text{ s}^{-1}$. The edge of the high vorticity layer coincides with the line of floats that is drawn off the headland at the point of flow separation, and the curling up of the free end is shown (Figure 3-4d).

At the end of the half cycle ($t = 6$ hours), all three fields are nearly mirror images of the fields at the start of the cycle (Figure 3-5). The pressure gradient is now exerting a westward force, and a small bulge can be seen in the pressure contours at the location of the clockwise eddy (Figure 3-5a). The flow far offshore of the headland is weakly eastward, while the flow along the tip has turned to the west (Figure 3-5b). The eddy has moved

further downstream, the center located 4 km to the east of the headland tip (roughly half a tidal excursion). The vorticity field shows that the counter-clockwise eddy has completely disappeared, and the clockwise eddy has a larger extent and decreased peak magnitude compared to $t = 3$ hours (Figure 3-5c). Positive vorticity is present along the eastern side of the headland, associated with the shear in the westward flow along the boundary. The floats in the clockwise eddy continue to spiral up, while the floats that were in the counterclockwise eddy are no longer wrapping, since the eddy has been completely damped by bottom friction (Figure 3-5d).

The second half cycle is nearly a mirror image of the first half cycle, and therefore will not be discussed. The only departures from symmetry are due to the eastward propagation of the forcing tidal wave, which causes the water depth to be about 1 m greater during eastward flow. The effect of the Earth's rotation is not important, since the relative vorticity ($5.25 \times 10^{-4} \text{ s}^{-1}$) is much larger than the planetary vorticity f ($1 \times 10^{-4} \text{ s}^{-1}$).

The snapshots of the model current field are qualitatively similar to the current field obtained with high resolution Acoustic Doppler Current Profiler measurements at Gay Head, Massachusetts (Geyer and Signell, 1989). Figure 3-6 shows the current field at maximum flood (3 hours) and slack high water (6 hours) constructed from data along numerous ship tracks. The generation and evolution of the transient eddy has the same character as the corresponding model currents (Figure 3-4b and Figure 3-5b). The flow at maximum current shows flow separation occurring just downstream of the headland tip, and the flow at slack water shows that a large clockwise eddy has formed.

3.3.2 Time series at fixed locations

To illustrate further the behavior of the flow, the time series of elevation, velocity and vorticity are shown for three points in the domain that characterize different dynamical regimes (Figure 3-7). Point A is located away from the headland's influence, Point B is located directly off the headland tip, and Point C is located in the region influenced by the eddy formed on the eastward flowing tide. The curvilinear velocity components u_1 and u_2 will be referred to as alongshore and cross-shore flow, respectively.

Away from the influence of the headland (Point A), the elevation and flow are nearly

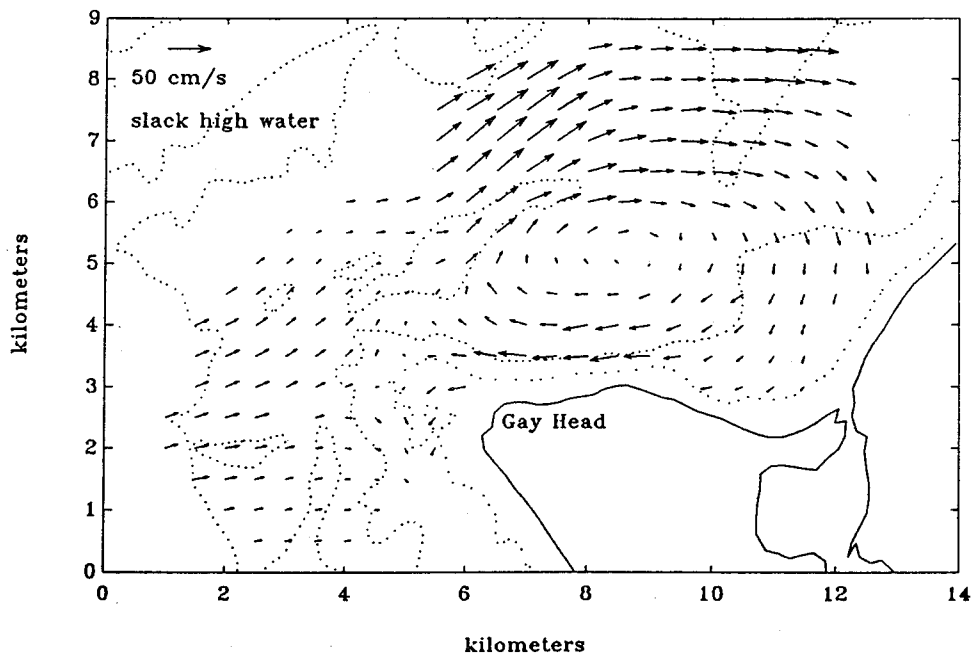
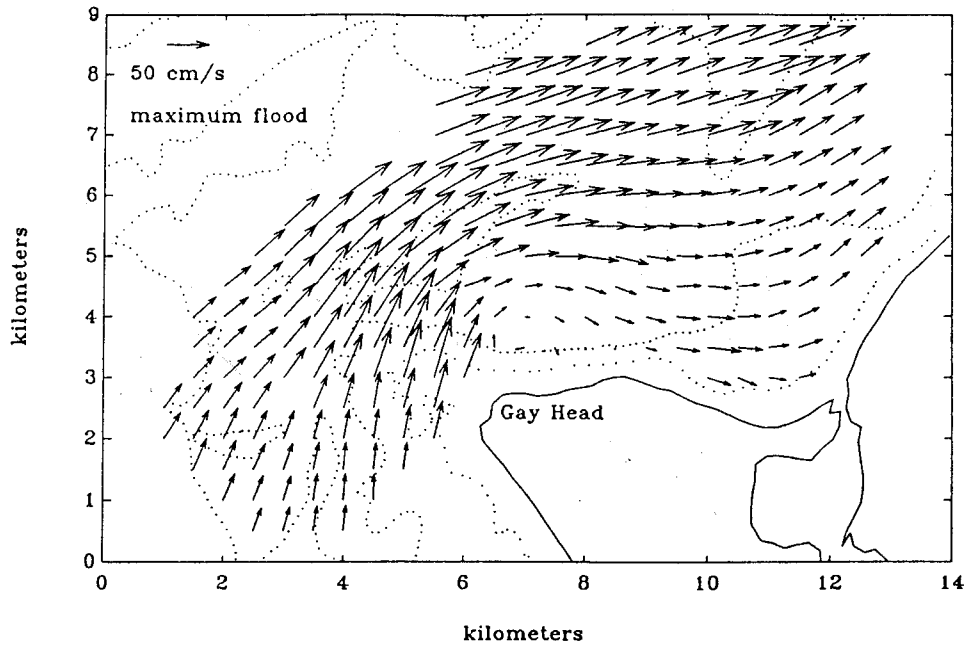


Figure 3-6: Observations of the current field at maximum flood (3 hours) and slack high water (6 hours), obtained with acoustic Doppler current profiler measurements at Gay Head, Massachusetts (Geyer and Signell, 1989).

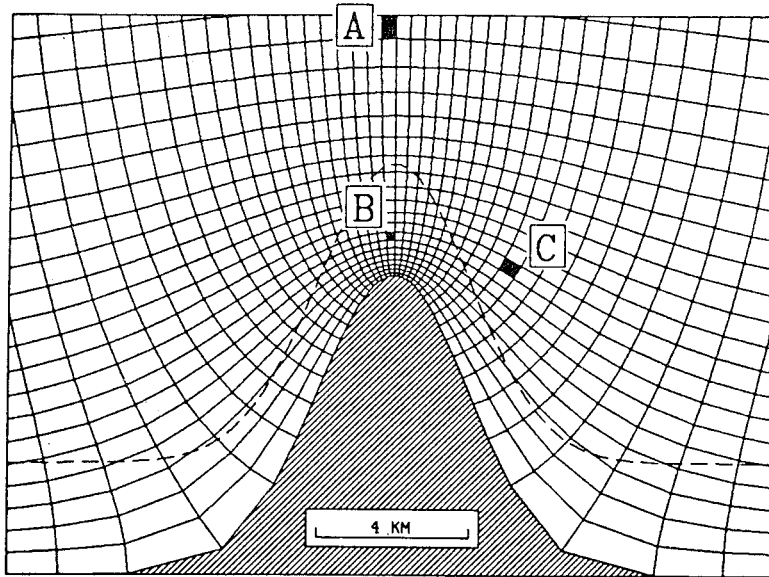


Figure 3-7: Location of points at which time series of elevation, velocity and vorticity are presented. Point A characterizes the flow away from the headland's influence; Point B, the flow off the tip of the headland; and Point C, the flow influenced by the formed eddy.

sinusoidal, reflecting the nature of the oscillatory forcing flow (Figure 3-8a). The M_2 tidal flow specified on the western boundary and the radiation condition on the eastern boundary result in a nearly progressive M_2 tidal wave with an amplitude of 0.7 m. The phase difference (≈ 0.5 hours) between elevation and velocity is the result of bottom friction. The increase in the amplitude of the alongshore velocity from 0.5 to 0.7 m s^{-1} and the small, nearly constant cross-shore velocity indicate the weak effect of the headland. The vorticity amplitude is negligible, much less than $1 \times 10^{-4} \text{ s}^{-1}$.

Off the tip of the headland (Point B) the elevation is still dominantly sinusoidal, but a strongly asymmetrical response (indicating significant nonlinearity) is seen in the velocity and vorticity fields (Figure 3-8b). The magnitude of the alongshore velocity shows nearly a two-fold increase compared to Point A, and the maximum current occurs two hours before the maximum elevation, indicating that the dominant momentum balance is between the pressure gradient and bottom friction terms. The component of cross-shore flow is comparable to the strength of the far-field flow, and is directed offshore over the entire tidal cycle. The departure from sinusoidal response reflects the presence of overtide and mean components in the flow. These constituents are chiefly generated by nonlinear self-

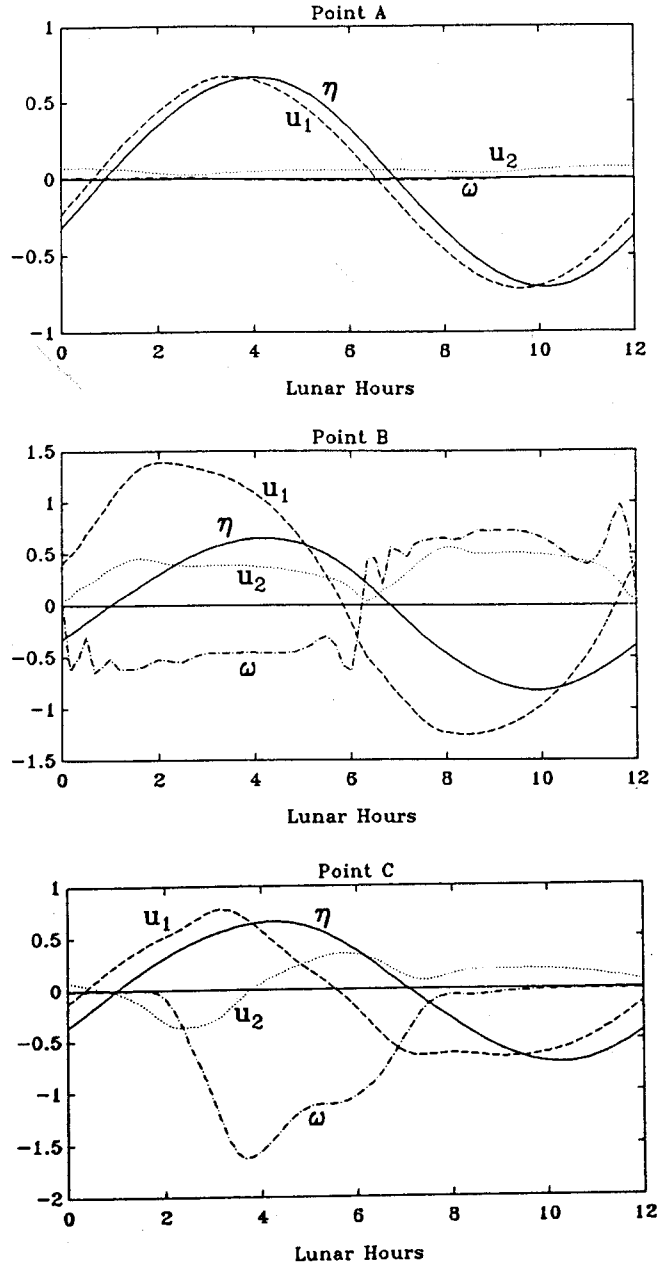


Figure 3-8: Time series of elevation η (m), alongshore velocity u_1 (m s^{-1}), cross-shore velocity u_2 (m s^{-1}), and vorticity ω (s^{-1}) at points A, B, and C (see Figure 3-7). Vorticity values have been multiplied by 10^3 .

interaction of the M_2 tide, and will be described in detail in the following section. The vorticity has a nearly constant value of $-5 \times 10^{-4} \text{ s}^{-1}$ over the eastward half cycle, and a nearly constant value of $5 \times 10^{-4} \text{ s}^{-1}$ over the westward half cycle. This quasi-steady behavior of the vorticity during each half cycle reflects the strong frictional influence in this region.

In a region influenced by the clockwise eddy (Point C), the velocity and vorticity fields again exhibit considerable asymmetry (Figure 3-8c). Over the first half cycle (0-6 hours), the cross-shore flow component oscillates between negative and positive values as the developing eddy passes through the region. The vorticity reaches a minimum of $-15 \times 10^{-4} \text{ s}^{-1}$ at the closest encounter of the eddy, then decreases as the eddy moves out of the region.

These time series at the three locations illustrate the different dynamical regions of the domain and how the dynamics are characterized by the vorticity. Far away from the headland, the dynamics are nearly linear: a nearly progressive tidal wave propagates along a channel with slight damping due to bottom friction, generating nearly sinusoidal elevation and velocity fields. There is very little vorticity in this region. In contrast, the region near the headland tip is characterized by a highly asymmetric velocity field, indicating nonlinear processes, and large vorticity levels over much of the tidal cycle.

3.3.3 Harmonic decomposition

Since tidal flows are periodic, a standard practice is to decompose tidal time series into component frequencies. In deep water, where tidal dynamics are essentially linear, the constituent frequencies correspond directly to astronomical forcing frequencies. In shallow water, nonlinearity in the governing equations gives rise to harmonics of the forcing frequencies. If the tides are weakly nonlinear (tide-induced residual and overtides much weaker than the fundamental), the dynamics can often be understood by decomposing the flow into a first-order component oscillating at the basic frequency, and second-order components with frequencies zero and twice that of the basic flow. For some simple situations these second order components can be obtained analytically through perturbation methods (e.g., Huthnance, 1973; Loder, 1980). As the strength of the nonlinearly-induced components grow with respect to the mean, perturbation methods break down, and solutions must in general

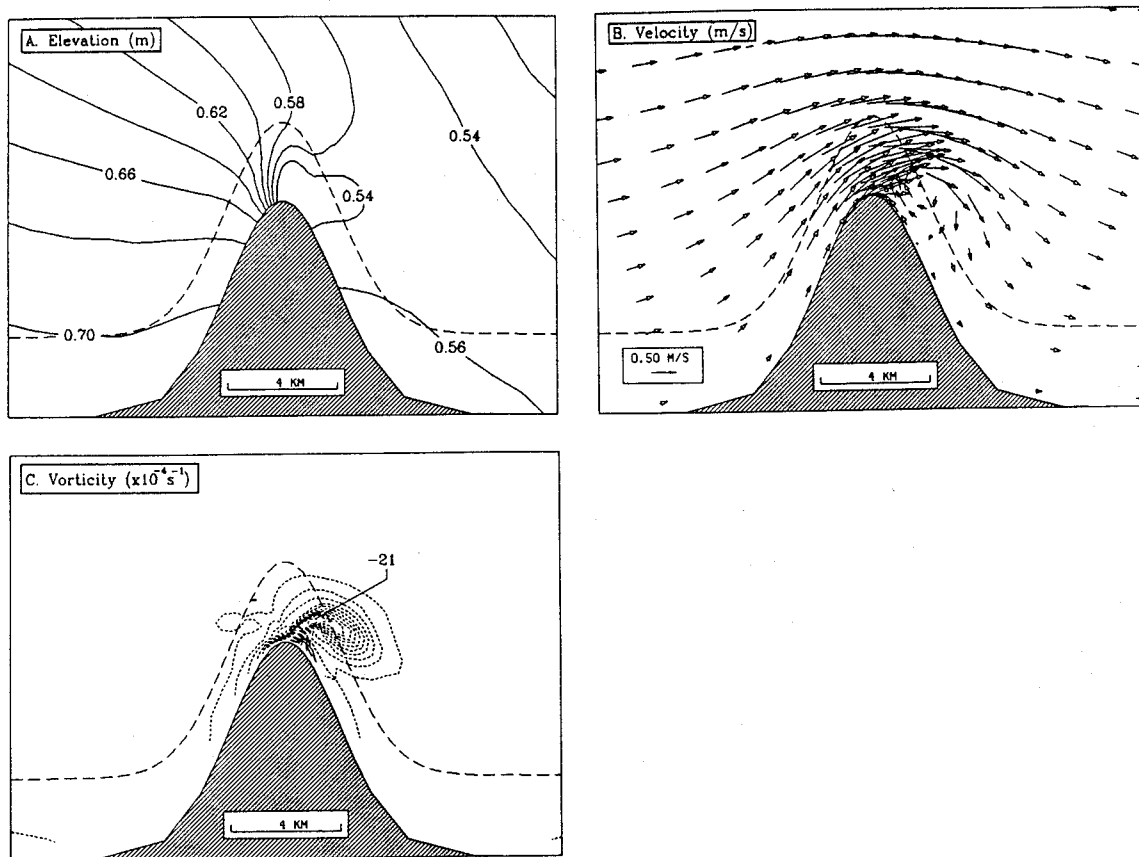


Figure 3-9: Tide at 3 lunar hours reconstructed from mean, M_2 , and M_4 frequencies.

be obtained numerically. Much of the tidal signal, however, is still contained in the mean, fundamental (M_2) and first harmonic (M_4). As an illustration of the information contained in the first few constituents for Case A, Figures 3-9 and 3-10 show the tide at 3 and 6 hours, reconstructed from the mean, M_2 , and M_4 frequencies only. Comparing to Figures 3-4 and 3-5 shows that the gross aspects of the flow are well represented, but the details of the flow separation are not resolved.

Although the dynamics of the flow are perhaps more naturally described in the time domain, which emphasizes the transient nature of the flow separation and eddy formation, it is still useful to consider the M_2 , mean, and M_4 fields, particularly for interpreting observations and for relating headland flow to other tidal studies. The mean current generated

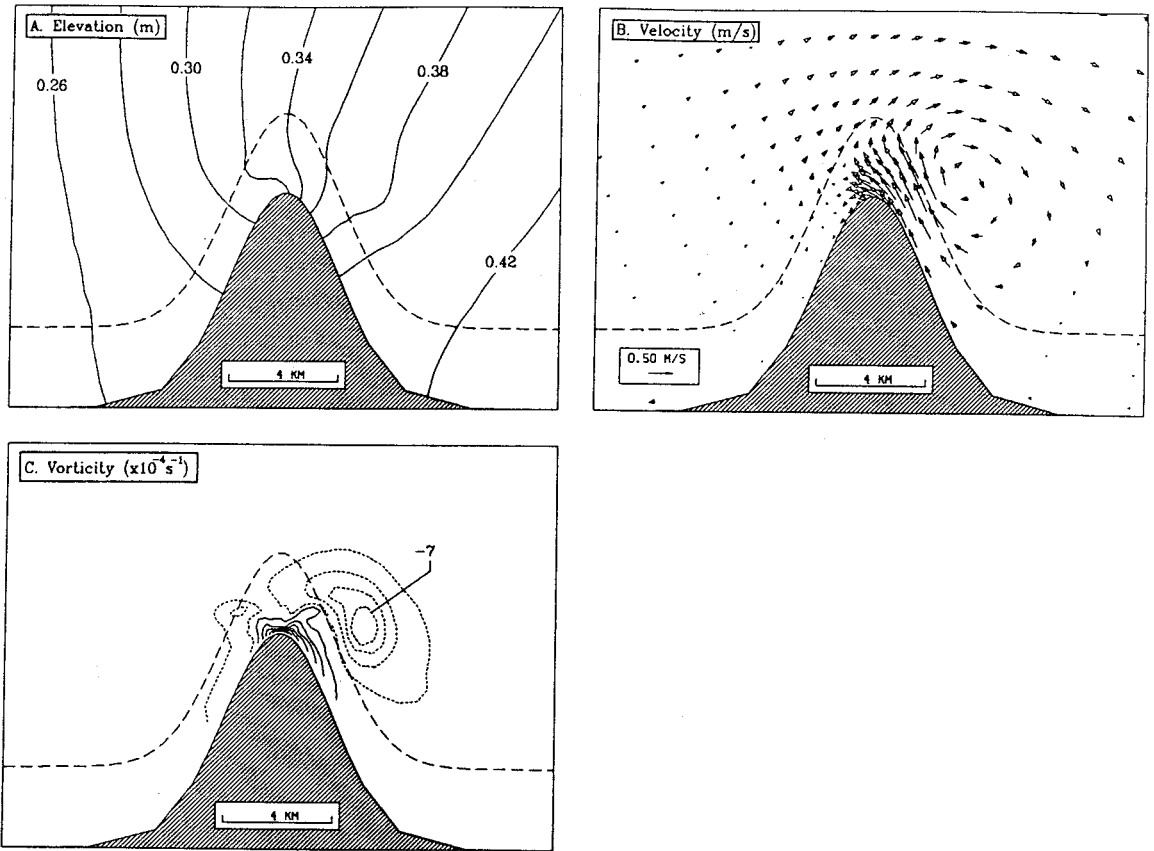


Figure 3-10: Tide at 6 lunar hours reconstructed from mean, M_2 , and M_4 frequencies.

by tidal effects has received much attention over the last fifteen years (see review by Robinson, 1983). Also called the tide-induced residual current or tidally rectified flow, it is an important contributor to long-term transport of material in regions where the spatial scale of the residual field is much larger than the tidal excursion. The mean elevation field is important in interpreting data from pressure gauges in the vicinity of a headland. The M_4 fields, like the mean fields, are principally generated as the result of M_2 - M_2 interaction. M_4 currents are especially important because they represent asymmetry in the tidal flow (e.g., a strong flood of short duration followed by a weaker ebb of long duration). For processes like sediment transport that scale nonlinearly with the flow speed, such asymmetry results in a tide-induced residual transport even in the absence of residual currents. Pingree and Griffiths (1979) calculated the mean bottom stress on the Northwest European shelf from M_2 and M_4 numerical model output and showed that the distribution of stress has strong similarity to sand transport paths based on geological evidence.

Before the harmonic analysis of the tidal fields are presented, it is first useful to understand how transient eddies are represented in terms of harmonic constituents. Figure 3-11 shows a least squares fit of the M_2 , mean, and M_4 constituents to the vorticity time series at Point C (Figure 3-8c). The vorticity at Point C is due exclusively to the passage of the clockwise eddy, which affects the flow for roughly six hours at this location. For the remainder of the cycle, the vorticity is near zero. This 6 hour pulse of vorticity is reflected in the harmonic decomposition by an M_4 component roughly 50% of the amplitude of M_2 , and a mean component roughly 75% of M_2 . The amplitude of these components vary as the location relative to the path of the eddy changes, and the shape of the pulse changes. Other attributes of the eddy, such as the local depression in sea level that drives the eddy's radial acceleration, will also be reflected as M_4 and mean components at fixed locations.

M_2 , mean and M_4 elevation

The M_2 elevation field is only weakly affected by processes taking place at the headland (Figure 3-12a,b). The elevation amplitude deviates less than 4% from an average value of 0.73 m, and the phase changes by 12° (24 lunar minutes) over the 20 km extent shown in the figure. High tide occurs at the headland tip 30° (1 hour) after the beginning of the tidal cycle. The phase increase and amplitude decrease toward the east is consistent with

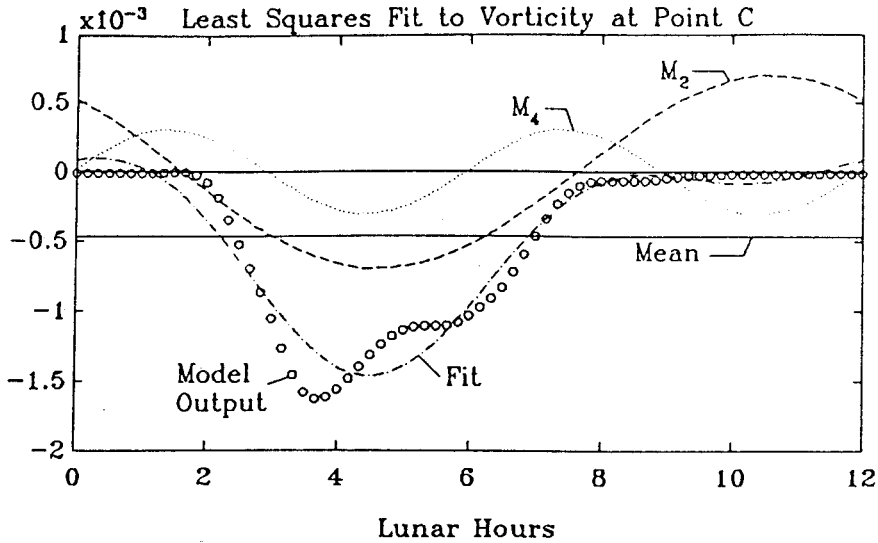


Figure 3-11: A least squares fit of M_2 , mean, and M_4 constituents to the vorticity at Point C (the region influenced by eddy formation at the headland tip). The roughly six hour pulse of vorticity is due to the passage of an eddy, and is reflected in mean and M_4 components that are 50 and 75% of the M_2 amplitude.

an eastward-propagating, slightly-damped tidal wave. The small decrease in amplitude offshore reflects the effect of the Earth's rotation, and the presence of the transient eddies is apparent in the slightly increased amplitude on the western side of the headland and the slightly reduced amplitude on the eastern side.

Compared to the amplitude of the M_2 , the nonlinearly-induced elevation components are very small (Figure 3-12c,d). The mean and M_4 extrema both occur off the headland tip, the mean with a 0.064 m depression and the M_4 with a maximum amplitude of 0.042 m. This can be explained by the Bernoulli effect, which causes pressure to vary with the speed squared. Squaring the sinusoidal M_2 velocity field gives rise to mean and M_4 components, and since the M_2 velocity has a maximum just offshore of the headland tip (as described below), the mean and M_4 components have extrema there as well.

The M_4 elevation maximum is flanked by secondary maxima to the west and east of the tip, with magnitudes of 0.036 m and 0.027 m respectively. These maxima are associated with the transient eddies, as each eddy has a slight depression in the sea surface which balances the radial acceleration. The roughly six-hour duration of each eddy gives rise to

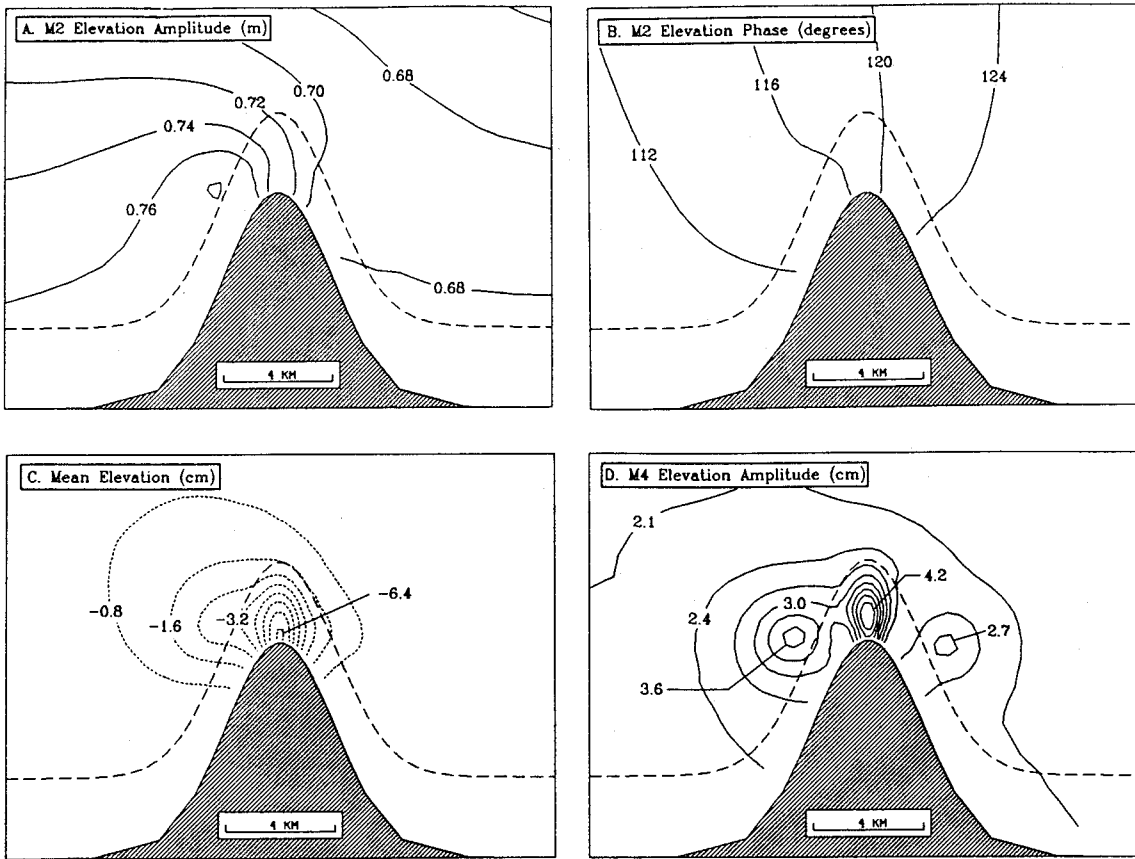


Figure 3-12: Harmonic constituents of elevation: (a) M_2 elevation amplitude; (b) M_2 elevation phase; (c) mean elevation; and (d) M_4 elevation amplitude.

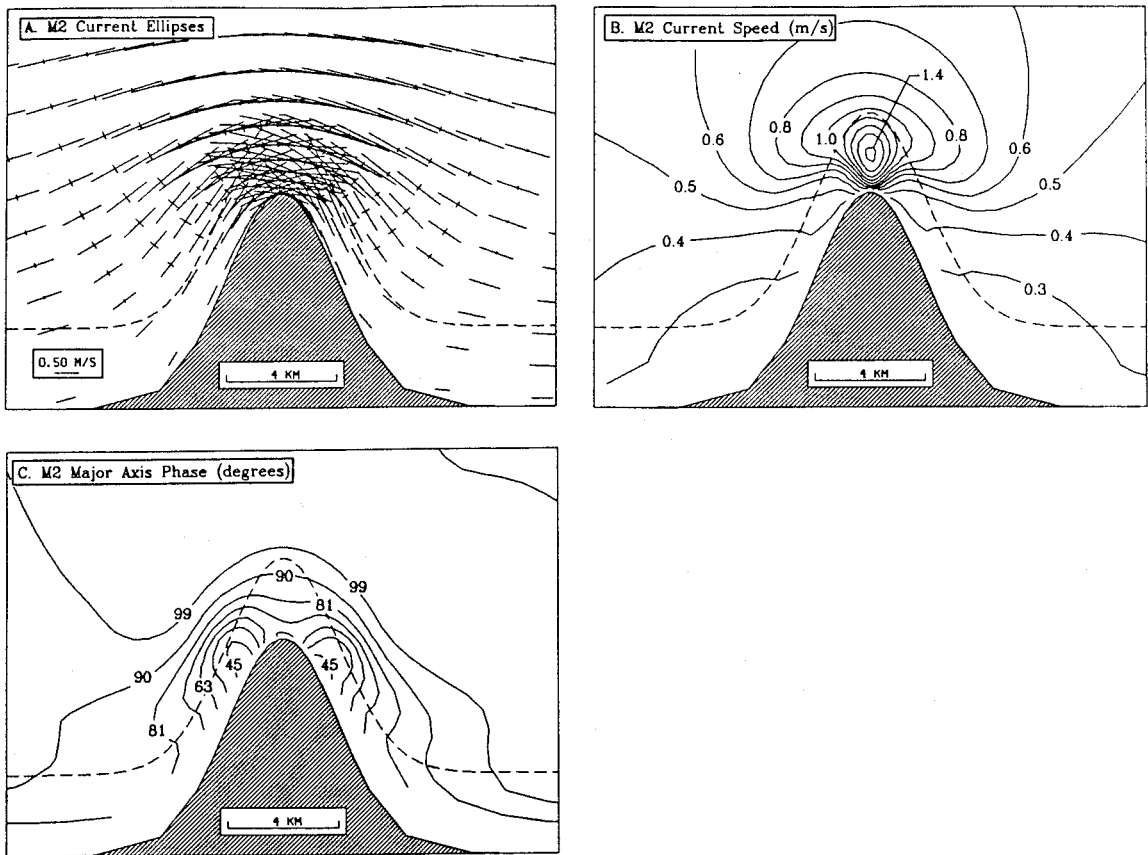


Figure 3-13: M_2 velocity field. (a) Tidal ellipses. (b) Major axis amplitude (m s^{-1}). (c) Phase in intervals of 9° .

secondary constituents as described for the vorticity in section 3.3.3.

M_2 , mean and M_4 velocity

While the M_2 elevation field is only mildly affected by the headland, the headland has a strong influence on the M_2 velocity field (Figure 3-13). The major-axis amplitude increases rapidly near the headland tip due to potential flow effects (section 4.2.1), reaching a peak value of 1.4 m s^{-1} off the tip of the headland, nearly 3 times higher than the far-field current amplitude. At the base of the headland the tides are weaker than the forcing strength, with an amplitude of only 0.2 m s^{-1} . The phase of the M_2 currents is such that the maximum current far offshore of the headland tip occurs 20 minutes after the maximum current at

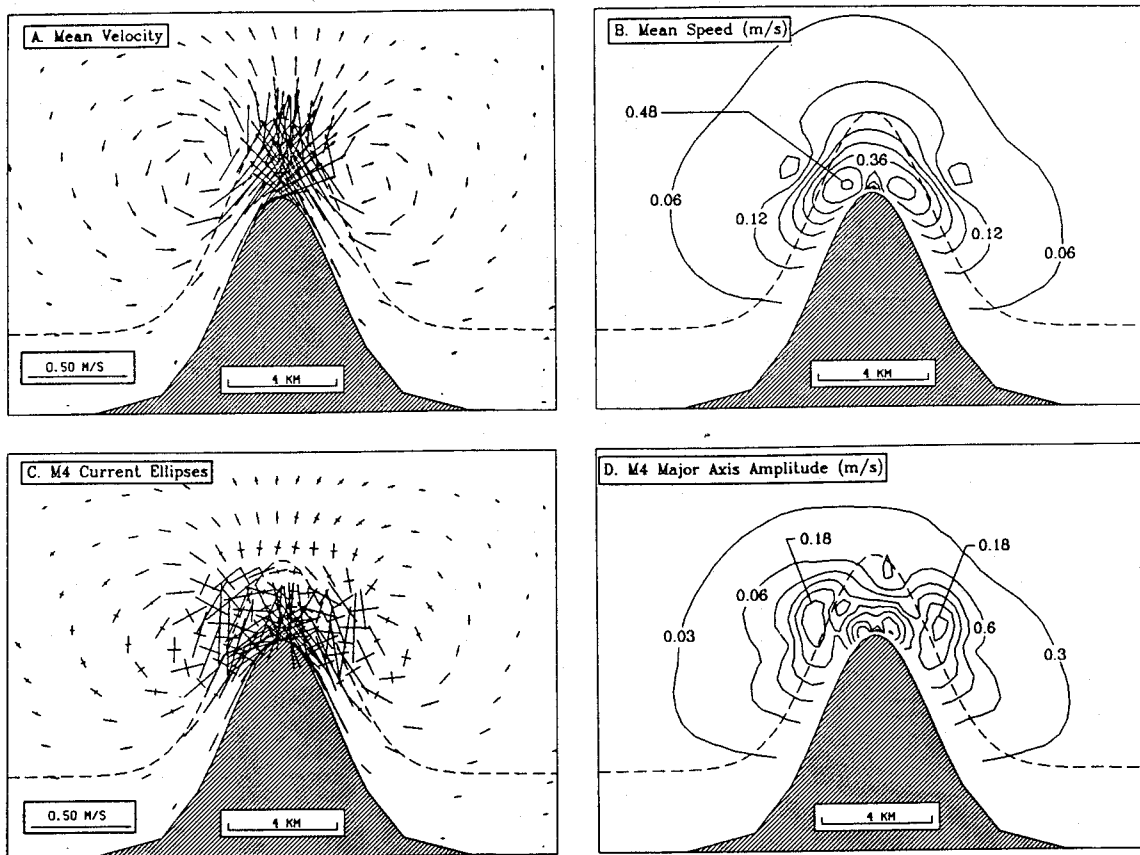


Figure 3-14: The mean and M_4 velocity fields. (a) Mean velocity vectors. (b) Mean current magnitude. (c) M_4 current ellipses. (d) M_4 major axis amplitude.

the western open boundary (Figure 3-13c). As the headland is approached, the tide turns earlier due to the combined effect of friction and the transient eddies. The tide on either side of the headland turns nearly 2 hours before the free stream flow. The ellipses are oriented within 20° of the orientation of the numerical model grid (which constitute streamlines of potential flow), and the ratio of the minor and major axes is less than 0.2 throughout the domain, indicating that the M_2 tide is essentially co-linear.

The mean current field clearly shows the result of time-averaging the transient eddies generated on each phase of the tide (Figure 3-14a,b). Two large counter-rotating residual eddies straddle the headland, with strong offshore flow ($0.2\text{--}0.4\text{ m s}^{-1}$) between the eddies

at the headland tip. The mean flow has the greatest magnitude in the shoaling regions near the sides of the headland where recirculation occurs. The mean in this region reaches a maximum of 0.48 m s^{-1} , nearly equal to the 0.50 m s^{-1} amplitude of the far-field flow.

The M_4 velocity field is similar to the mean velocity field, with major axes of the ellipses forming a circular pattern on either side of the headland (Figures 3-14c,d). The maximum at the headland tip is 0.18 m s^{-1} , about 50% of the mean, and is due to the offshore component of flow that occurs on both phases of the tide. The local maxima on either side of the headland are due to transient eddies which from the time series at Point C were shown to cause the cross-shore velocity to fluctuate between positive and negative values over a six hour period.

M_2 , mean and M_4 vorticity

The M_2 vorticity is mushroom-shaped, with a strong maximum ($> 25 \times 10^{-4} \text{ s}^{-1}$) at the tip of the headland (Figure 3-15a). The structure on either side of the headland for the M_2 vorticity is very similar to the transient vorticity structure in Figures 3-2c and 3-5c with local maxima at the locations of the transient eddies. As previously described, on either side of the headland, one half cycle is highly rotational, with a strong eddy, while the other half cycle is nearly irrotational and has no eddy. Fourier decomposing this signal, therefore, yields M_2 , M_4 and mean components.

The headland eddies are reflected in two large patches of positive and negative mean vorticity, which are linked to the headland tip by narrow filaments of high magnitude (Figure 3-15b). Along the boundary of the headland, there are thin regions of high residual vorticity which reflect the boundary shear associated with flow that is directed toward the headland tip over much of the tidal cycle. The mean vorticity magnitude in the two eddies is over $3 \times 10^{-4} \text{ s}^{-1}$, which is substantially larger than the planetary vorticity f ($1 \times 10^{-4} \text{ s}^{-1}$).

The M_4 vorticity field has maxima of $7 \times 10^{-4} \text{ s}^{-1}$ on either side of the headland (Figure 3-15c). Like the M_2 vorticity field, these maxima are linked to the passage of the transient eddies.

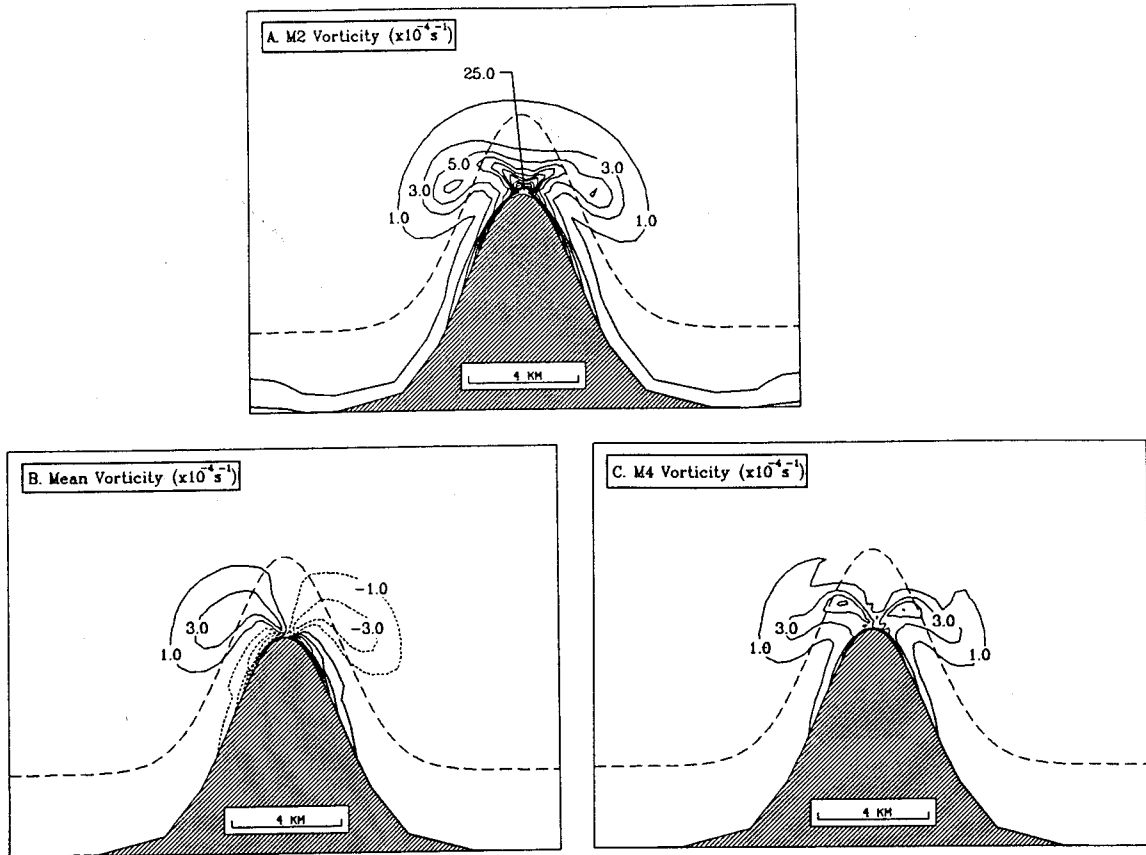


Figure 3-15: Contours of (a) M_2 vorticity, (b) mean vorticity, and (c) M_4 vorticity fields. Dashed lines indicate negative vorticity, and the contour interval is $2 \times 10^{-4} \text{ s}^{-1}$.

3.4 The vorticity balance

3.4.1 The depth-averaged vorticity equation

The model results presented thus far have indicated that vorticity is an important descriptor of tidal flow around headlands. The formation of the time-dependent eddies, which characterize strongly nonlinear flow around headlands, can be understood most easily in terms of vorticity production, advection and dissipation. To identify the important aspects of the vorticity dynamics, the depth-averaged vorticity equation is explored, then specific examples of the vorticity balance at fixed points and following the path of a water parcel will be presented for Case A.

The depth-averaged vorticity equation is obtained by taking the curl of the momentum equation (2.8). Dropping the bars denoting depth-averaging, the result is

$$\frac{\partial \omega}{\partial t} + \mathbf{u} \cdot \nabla \omega - \frac{\omega + f}{h + \eta} \left[\frac{\partial \eta}{\partial t} + \mathbf{u} \cdot \nabla (h + \eta) \right] + \left[\nabla \times \left(\frac{C_D |\mathbf{u}| \mathbf{u}}{h + \eta} \right) \right] \cdot \hat{\mathbf{k}} - A_h \nabla^2 \omega = 0, \quad (3.2)$$

where ω is the vertical component of vorticity defined by

$$\omega = \frac{\partial v}{\partial x} - \frac{\partial u}{\partial y}. \quad (3.3)$$

The first three terms represent the time rate-of-change of vorticity, advection of vorticity, and vortex stretching. The fourth term represents the curl of the depth-distributed bottom stress and the fifth term, lateral diffusion.

The curl of the depth-distributed bottom stress contains both vorticity production and dissipation mechanisms. To see this, the term can be divided into three parts:

$$\left[\nabla \times \left(\frac{C_D |\mathbf{u}| \mathbf{u}}{h + \eta} \right) \right] \cdot \hat{\mathbf{k}} = \frac{C_D |\mathbf{u}|}{(h + \eta)^2} [\mathbf{u} \times \nabla (h + \eta)] \cdot \hat{\mathbf{k}} - \frac{C_D (\mathbf{u} \times \nabla |\mathbf{u}|) \cdot \hat{\mathbf{k}}}{h + \eta} + \frac{C_D |\mathbf{u}| \omega}{h + \eta} \quad (3.4)$$

The first term on the right hand side, “slope torque”, acts as a source of vorticity when there is a component of velocity normal to the depth gradient (e.g., x -directed flow over a y -directed bottom slope). Physically, the flow in shallower water feels a greater depth-distributed drag force than the flow in deeper water, resulting in a torque on the fluid column. The second term, “speed torque”, generates vorticity when there is a component of velocity perpendicular to the gradient of speed. This term arises from the quadratic nature of the bottom stress, which exerts a torque due to the fact that stronger flow is

relatively more retarded than weaker flow. The third term represents vorticity dissipation by bottom friction, with a frictional decay time scale equal to $[h/C_D|u|]$.

As a simple example of the vorticity generated and dissipated by the curl of the depth-distributed bottom stress, consider the vorticity balance in a steady parallel shear flow over a transverse slope. For a flow driven by a constant x -directed pressure gradient over y -directed bottom slope, there is no x variation in the flow, and the vorticity is simply given by $\omega = -\partial u/\partial y$. Since u is everywhere positive, the dissipation term and the speed torque term are the same, expressed by

$$\frac{C_D u}{h + \eta} \frac{\partial u}{\partial y} \quad (3.5)$$

Since dissipation must equal production in steady flow, the slope torque term opposes and has twice the magnitude of (3.5). Half the negative vorticity produced by the slope torque is dissipated, and half is negated by the production of positive vorticity resulting from the increasing flow speed with y . The speed torque term always acts to reduce the speed gradient transverse to the flow. For a flat bottom, in the absence of horizontal viscosity, this is the only vorticity generating mechanism.

3.4.2 The Eulerian vorticity balance

In this and the following section, the balance of terms in the vorticity equation is investigated at key locations and along a particular trajectory which characterize the nature of the vorticity production, advection and dissipation. It is found that there are three distinct regions of differing dynamics. The first region is the production region, upstream of the headland, where as the flow travels along the isobaths, production of vorticity by slope torque is in quasi-steady balance with dissipation and speed torque. The second region is over the shoaling region just downstream of the flow separation, where the flow crosses the isobaths, and the vorticity is augmented by vortex stretching. The third region is the flat interior downstream of the flow separation, where vorticity production is negligible, and the vorticity is slowly diminished due to frictional dissipation.

Figure 3-16 shows the location of the three points at which the vorticity balance is quantified. Point D is located in the upstream production region over the first half of the tidal cycle, just to the west of the headland over the sloping bottom. Point E is located

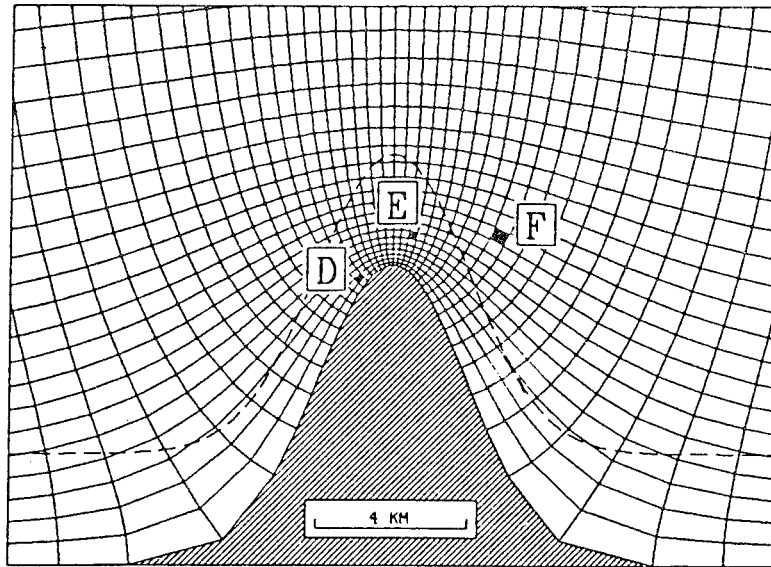


Figure 3-16: Location of points for Eulerian vorticity balance calculation. For the eastward phase of the tide, point D is located on the leading edge of the headland, point E is over the shoaling region downstream of the flow separation and point F is in the flat interior but still within the influence of the eddy formed during eastward flow.

where the vorticity leaving the headland tip during the first half cycle passes over the sloping bottom just downstream of the headland. Point F is located over the flat bottom within the region of influence of the eddy produced during the first half cycle.

At point D, the vorticity has a large negative value over much of the tidal cycle (Figure 3-17a). At the beginning of the cycle, the strong flow to the west of the headland results in a large velocity gradient (Figure 3-2b), and the vorticity has nearly obtained its peak magnitude of $13 \times 10^{-4} \text{ s}^{-1}$. The vorticity balance is quasi-steady over much of the first half cycle as can be seen from the small magnitude of $\partial\omega/\partial t$. The diffusive flux is also small. Slope torque produces a large amount of negative vorticity as the flow passes over the transverse bottom slope, but this production is balanced by roughly equal contributions of dissipation, speed torque, vortex squashing, and downstream flux of negative vorticity. The vortex squashing arises from the fact that the flow is not traveling strictly along the isobaths but has a small onshore component. The downstream flux of vorticity indicates that this region is a net exporter of negative vorticity. At the beginning of the second half cycle (6 hours), the vorticity becomes positive for a short time before the westward

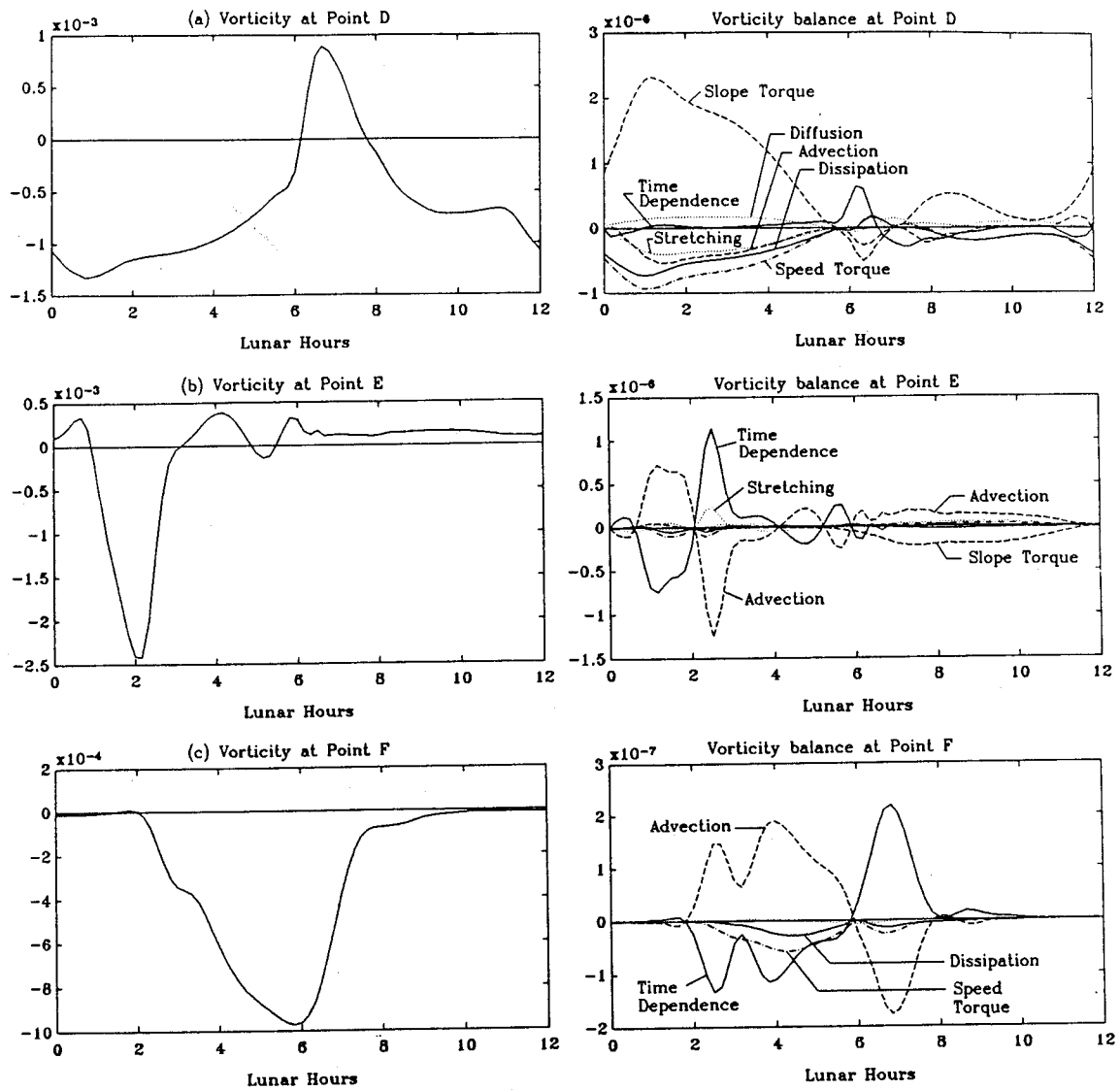


Figure 3-17: Vorticity ω and the Eulerian vorticity balance (terms in Equation 3.2) at Points D, E and F (see Figure 3-16 for locations).

flow around the headland tip separates. When the flow separates, the current at this point is in the recirculation zone of the counter-clockwise eddy, and eastward flow once again commences, again resulting in negative vorticity in the boundary layer.

At point E, the vorticity balance changes dramatically (Figure 3-17b). While the balance at Point D is quasi-steady, here the local rate-of-change and advection terms dominate the balance, and the production and dissipation terms are minimal with the exception of a peak in the vortex stretching term between two and three hours. This peak occurs as strong flow crosses the bathymetry at nearly right angles. For most of the first half cycle, the local time derivative balances advection, indicating the passage of vorticity through the region. The large oscillation in the time dependence and advection between one and three hours indicates the passage of the eddy generated at the headland tip. This is clearly seen in the vorticity magnitude at 2 hours of nearly $25 \times 10^{-4} \text{ s}^{-1}$. As the vorticity maximum associated with the eddy core moves through the region, the time rate-of-change first becomes negative as the magnitude of the negative vorticity increases, then becomes positive as the magnitude decreases following the passage of the core. During the second half cycle, the vorticity is relatively small, as the flow is essentially irrotational at this point. The small amount of vorticity that is produced is advected downstream.

At point F, there is again a dominance of the local rate-of-change and advection terms, although the peak is not as sharp due to the reduced spatial gradients (Figure 3-17c). Dissipation is significant, however, and it limits the growth in magnitude of the negative vorticity. Due to the increased distance from the headland, the vorticity maximum does not occur until the end of the half cycle (4 hours later than at point E) and has a reduced magnitude of $10 \times 10^{-4} \text{ s}^{-1}$. At the beginning of the second half cycle (6 hours), the vorticity begins to advect back toward the west, and nearly irrotational flow is again established.

3.4.3 The Lagrangian vorticity balance

An alternative and perhaps more intuitive picture of the vorticity dynamics is obtained from the Lagrangian viewpoint, following the change in vorticity of a water parcel over a tidal cycle. Using the particle tracking technique described in section 2.3.2, Figure 3-18a shows the path of a water parcel tracked from the beginning of the tidal cycle, initially located

upstream of the headland tip in the flat interior region. The path passes through the regions just discussed from the Eulerian reference frame, and it illustrates the essential character of the vorticity balance. During the first half cycle, the particle moves onto the sloping bottom region, passes close to the tip of the headland, rapidly crosses into the flat interior and wraps around the clockwise eddy. During the second half cycle, the particle stays well outside the region of flow separation, being swept by the flow around the headland far into the western interior.

The most obvious aspect of the Lagrangian vorticity balance over the entire tidal excursion is that the production terms are large only between 1 and 3 hours, when the parcel is in the immediate vicinity of the headland tip (Figure 3-18b). Once the parcel leaves the headland, the vorticity magnitude begins to diminish due to the effect of frictional damping (Figure 3-18c). During the first hour, the parcel travels over the flat interior. The terms in the vorticity balance, and the vorticity itself, are close to zero. The parcel then moves diagonally across the sloping bottom as it approaches the headland tip, and the vorticity magnitude increases, primarily as the result of slope torque. After the parcel passes the headland tip (2.2 hours), it crosses nearly orthogonal to the bathymetry. The slope torque decreases rapidly, but the vortex stretching term takes over as the dominant production mechanism, and the vorticity magnitude continues to grow until the parcel is over the flat interior (2.7 hours). In the interior, the vorticity magnitude gradually decays due to frictional drag. Diffusion is negligible. The contributions of the dissipation and speed torque terms vary over the cycle, but have similar shape and magnitude. The vorticity magnitude decreases from 10 to $3 \times 10^{-4} \text{ s}^{-1}$ between 2.7 and 5.7 hours, indicating a frictional time scale of 3 hours. A similar decay scale is obtained from scaling, if it is assumed that the dissipation and speed torque act equally to damp the vorticity magnitude:

$$\frac{h}{2C_D|u|} \approx \frac{[20 \text{ m}]}{2[2.5 \times 10^{-3}][0.5 \text{ m s}^{-1}]} = 2.3 \text{ hours.} \quad (3.6)$$

3.5 Summary and discussion

The model results in this chapter have shown that for a headland with a length scale comparable to the tidal excursion, the flow may be highly nonlinear; snapshots of the

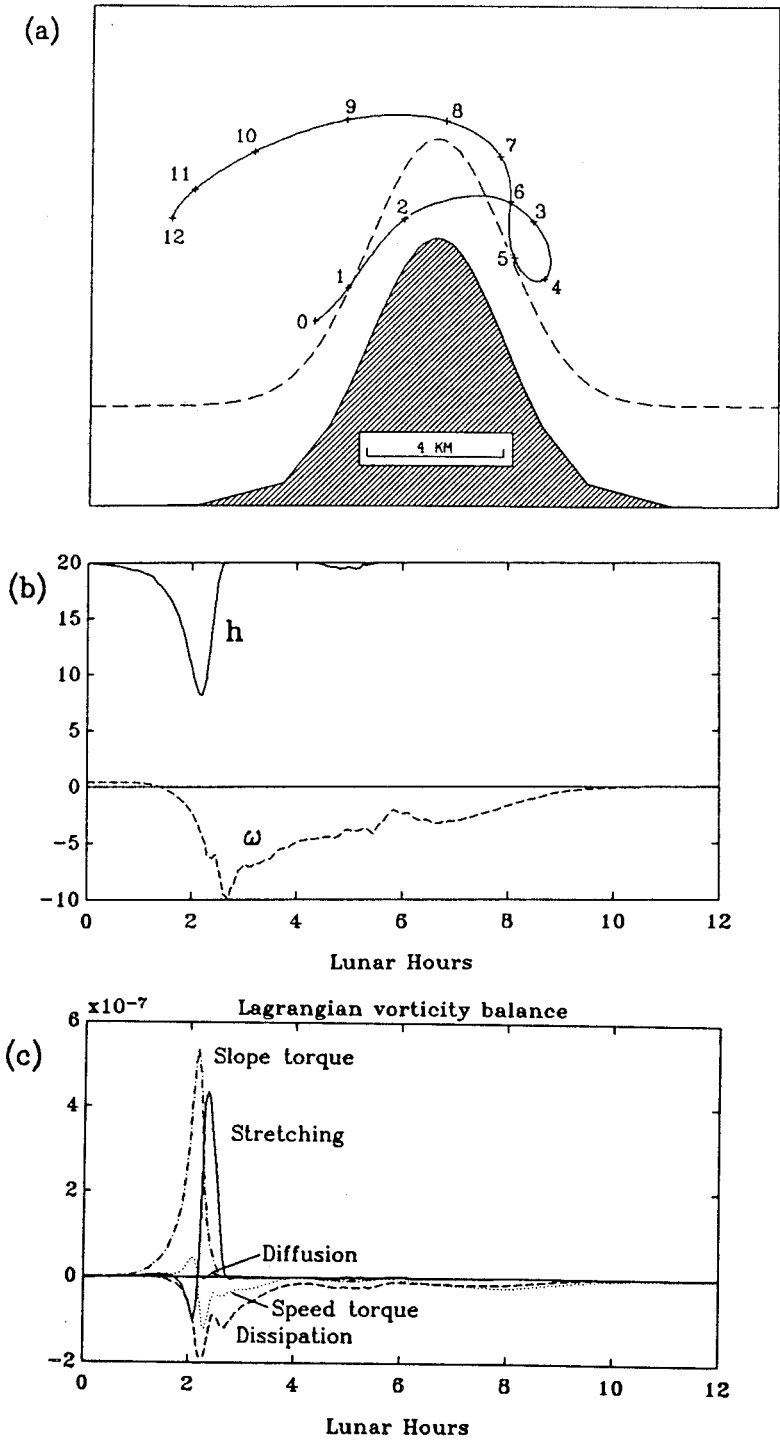


Figure 3-18: Lagrangian vorticity balance. (a) The path of the tracked parcel, released at the start of the tidal cycle (0 lunar hours). The locations of the parcel at hourly intervals are labeled. (b) Vorticity ($\times 10^{-4} \text{ s}^{-1}$) and depth (m) following the tracked parcel from 0-12 hours. (c) Vorticity balance following the parcel from 0-12 hours.

flow reveal the generation and decay of transient eddies and time-series of velocity and vorticity at fixed locations are strongly asymmetric. These characteristics of the flow can be conceptually understood by considering the production, advection and dissipation of vorticity.

From the snapshots of the vorticity field and the Eulerian and Lagrangian vorticity balance, the following picture emerges. During each half cycle, vorticity is generated predominantly by slope torque in the boundary layer along the leading edge of the headland. Near the headland tip, the flow separates and the vorticity from the boundary layer is advected into the interior. As the vortex tubes composing this thin strip move into deeper water, the vorticity magnitude increases as the tubes are stretched. As the free tip of this high vorticity strip advects downstream, it begins to curl up, forming a concentrated blob of vorticity which marks the center of a transient eddy. During the remainder of the half cycle, the vorticity production at the tip decreases, and damping due to bottom frictional dissipation and speed torque begin to erode the eddy. After the tide turns, the eddy is swept around to the opposite side of the headland, but the friction is strong enough that by the time a new eddy is formed on the opposite side of the headland, the strength of the old eddy is negligible. Since the advection of vorticity is limited by the tidal excursion, the dynamics are essentially linear at a distance greater than one tidal excursion from the headland. In this region, the currents and elevation are nearly sinusoidal, and the currents are nearly rectilinear.

From the analysis of the transient eddy formation in this chapter, the "phase eddy" mechanism for eddy generation proposed by Black and Gay (1987) seems conceptually incorrect. They argued that flow separation had little to do with transient eddy formation, claiming that eddies form as the result of the oscillatory pressure gradient, which near the end of the half cycle, reverses the frictionally controlled flow near the coast before the free-stream flow. The numerical results show, however, that the vorticity which forms transient eddies is produced near the headland tip and that flow separation is critical to transport this vorticity into the interior.

Chapter 4

Tidal Dynamics

4.1 Introduction

In this chapter, the dynamics of tidal flow around coastal headlands are investigated. Idealized models of flow separation and eddy evolution are first used to identify the important parameters that control these processes. The nature of the dependence on these parameters is then determined by a series of numerical model runs. These model runs indicate a wide range of behavior, from quasi-linear flow to highly nonlinear separating flow with interacting eddies shed during consecutive half cycles. For the case where eddies formed during subsequent half cycles do not interact, a model of the wake strength is developed, based on the vorticity flux at the headland tip and bottom frictional damping in the interior. In the last section, the tidal flow around a headland is compared and contrasted with lab results of two-dimensional viscous flow around bluff bodies.

4.2 An idealized model of flow separation

In the previous chapter it was demonstrated that flow separation played a critical role in the generation of transient eddies, as it allowed vorticity produced in a narrow layer along the headland to penetrate the interior. In this section, the parameters determining flow separation are obtained from an idealized model of the flow separation process. The flow upstream of the point of separation is assumed to be irrotational except for a thin

boundary layer of high vorticity. The irrotational flow solution is used to find the pressure gradient along the boundary, and the flow is shown to separate close to the point where the alongshore pressure gradient begins to decelerate the flow. Using an approximate analytic solution for the irrotational flow, the pressure gradient along the boundary is determined, which indicates the parameter dependence of flow separation.

4.2.1 Potential flow

Potential flow represents the solution for the tidal flow around a headland in a frictionless, narrow channel of constant depth, where the scale of the headland is much less than the tidal wavelength. If the ratio of the channel breadth B to the Rossby radius $R_r = \sqrt{gh}/f$ is small, then the effects of the earth's rotation can be neglected to order $[B/R_r]$. Since the flow is inviscid, there are no vorticity production mechanisms, and the flow is irrotational. If the Froude number $[U_o/\sqrt{gh}]$ is much less than one, then the tidal excursion $2U_o/\sigma$ is much less than the tidal wavelength. In this case, the time dependent free surface term $\partial\eta/\partial t$ in the continuity equation is negligible compared to the horizontal divergence terms $\partial u/\partial x, \partial v/\partial y$, and the rigid lid approximation is appropriate in the vicinity of the headland.

With the rigid lid approximation, the flow is strictly two-dimensional and the depth-averaged flow can be expressed in terms of a velocity potential ϕ (where $\nabla\phi = (u, v)$) that satisfies Laplace's equation. The tidal flow around the headland is therefore approximated by flow in a channel bounded by frictionless plates at the sides, surface and bottom forced sinusoidally by a plunger at one end, so that

$$\mathbf{u}(x, y, t) = \hat{\mathbf{u}}(x, y) \cos(\sigma t). \quad (4.1)$$

The potential flow solution is determined by requiring

$$\nabla^2\phi = 0, \quad (4.2)$$

subject to boundary conditions of no normal flow through the channel walls and $\hat{u} = U_o \cos(\sigma t)$ at the ends of the channel (Figure 4-1). The potential flow solution can be determined by analytic means for some simple geometries and by numerical means for more complex cases. For the problem posed here, the streamlines and equipotential lines of the

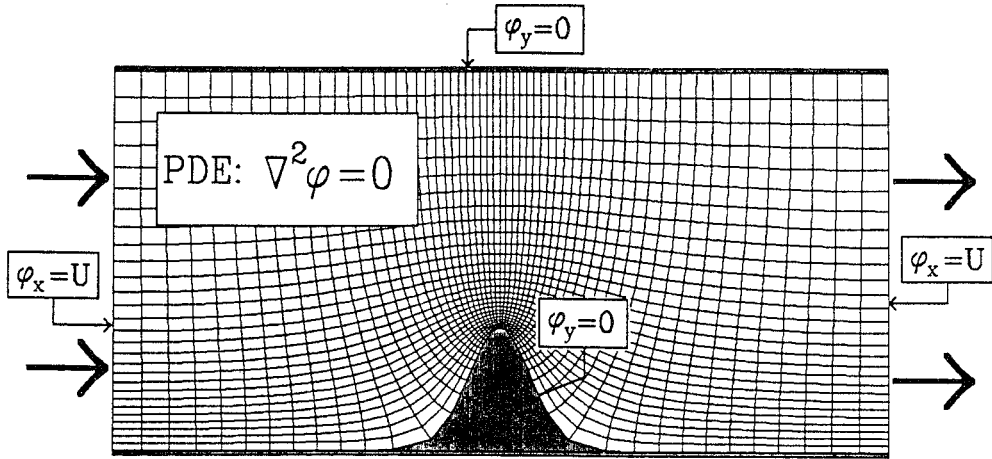


Figure 4-1: Schematic of potential flow calculation around a bump in a channel wall. The flow is fully specified by Laplace's equation for the velocity potential ϕ , normal flux boundary conditions at the open boundaries and no-flux conditions at the solid boundaries. The curvilinear orthogonal grid is the natural coordinate system of this flow.

potential flow coincide with the grid lines of the orthogonal curvilinear grid. Thus the curvilinear grid represents the natural coordinate system for irrotational flow: the flow is exclusively along x_1 grid lines and the component u_2 is identically zero everywhere. Once the velocity solution has been determined, the pressure field can be obtained by the momentum equation.

The irrotational flow field around an elliptic headland

Although the solution for potential flow around a Gaussian headland must be obtained numerically, an analytic solution exists for the potential flow around an elliptic headland, which has a similar potential flow solution around the headland tip. This facilitates the identification of the important parameters in the irrotational flow and the pressure gradient along the boundary. The coastline of the elliptic headland is defined by

$$y_E = b \left[1 - \left(\frac{x}{a} \right)^2 \right]^{\frac{1}{2}} ; |x| < a \quad (4.3)$$

$$y_E = 0 ; |x| > a$$

where a and b denote the x and y -directed semi-axes of the ellipse. If the same values for

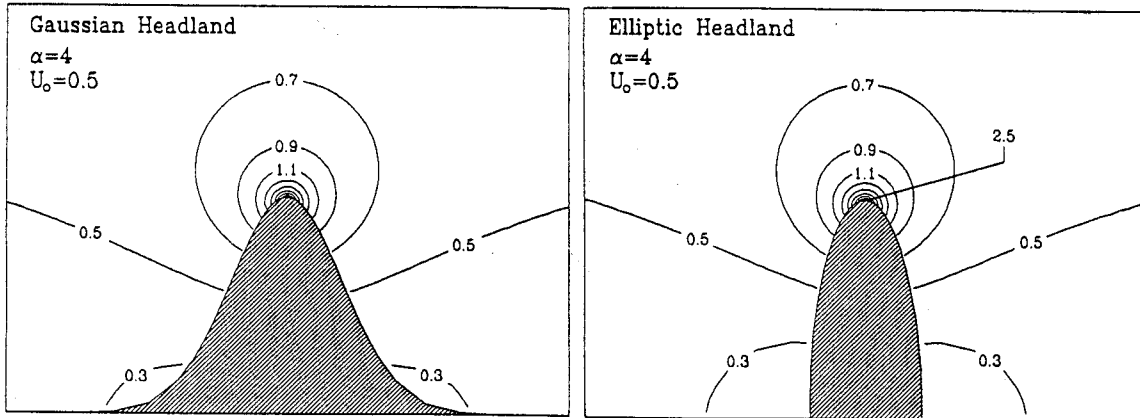


Figure 4-2: Potential flow solution around (a) Gaussian, and (b) elliptic headlands of aspect ratio $\alpha = 4$ for a uniform x -directed flow of $U_o = 0.5 \text{ m s}^{-1}$ at $x = -\infty$.

a and b are used to describe the Gaussian headland, the coastline is given by

$$y_G = b \exp \left[-\frac{1}{2} \left(\frac{x}{a} \right)^2 \right], \quad (4.4)$$

where a defines the length (equivalent to the standard deviation in a Gaussian probability distribution) and b defines the width.

The Gaussian and elliptic headlands are completely described by the length scale a and the width scale b . The irrotational velocity \hat{u}/U_o , therefore, is a function of the nondimensional position x/a and the aspect ratio of the headland only, where the aspect ratio α is defined by

$$\alpha \equiv \left[\frac{b}{a} \right]. \quad (4.5)$$

The exact potential flow solution for a x -directed uniform flow of U_o at $x = -\infty$ around an elliptical cylinder is given in Milne-Thompson (1938). The magnitude of the irrotational velocity around elliptic and Gaussian headlands with $\alpha = 4$ and a far-field flow of $U_o = 0.5 \text{ m s}^{-1}$ is shown in Figure 4-2. The solutions are nearly identical in the vicinity of the tip, indicating that the geometry of the headland away from the tip has little effect on the flow near the tip. The velocity gradients near the tip and the velocity at the tip both increase with the aspect ratio, as described below.

The potential flow along the boundary of an elliptic headland can be conveniently expressed by defining the angular coordinate θ , where $x/a = \cos \theta$ and $y/b = \sin \theta$ (Schlichting, 1968, p. 401). θ varies from 0 to π along the boundary of the headland. The velocity U_1 along the boundary is then given by

$$U_1 = U_o \frac{1 + \alpha}{\sqrt{1 + \alpha^2 \cot^2 \theta}}. \quad (4.6)$$

The maximum velocity occurs at $\theta = \pi/2$ (the headland tip), where the velocity is given by

$$\frac{U_1}{U_o} = 1 + \alpha, \quad (4.7)$$

which states that the flow at the tip increases linearly with increasing headland aspect ratio.

In summary, the solution to the irrotational tidal flow around an isolated coastal headland is determined exclusively by the headland geometry and the flow at the open boundaries. The solution for a Gaussian or elliptic headland depends only on the aspect ratio $\alpha = b/a$. There is a strong increase in flow near the tip of the headland, which for the elliptic headland results in a flow maximum of $(1 + \alpha)$ times the far-field flow.

The pressure field associated with irrotational flow

The pressure gradient associated with potential flow is important because it will later be shown to play a critical role in determining the point of flow separation (sections 4.2.2 and 4.2.3). The pressure gradient associated with potential flow can be determined by substituting the potential flow solution into the appropriate momentum equation and solving for the streamwise pressure gradient.

A momentum equation in which the solutions satisfy Laplace's equation is given by

$$\frac{\partial U_1}{\partial t} + U_1 \frac{\partial U_1}{\partial x_1} = -g \frac{\partial \eta}{\partial x_1} - \frac{C_D |U_o| U_1}{H}, \quad (4.8)$$

where U_1 is the irrotational velocity along the boundary and the bottom drag has been linearized by replacing $|U_1|$ with $|U_o|$, the far-field velocity. The expression for the pressure gradient along the boundary, from (4.6) and (4.8), is

$$g \frac{\partial \eta}{\partial x_1} = -\frac{U_o(1 + \alpha)}{\sqrt{1 + \alpha^2 \cot^2 \theta}} \left[\sigma \cos(\sigma t) + \frac{U_o}{a} \frac{(1 + \alpha)\alpha^2 \cos \theta}{(\sin^2 \theta + \alpha^2 \cos^2 \theta)^2} \sin^2(\sigma t) - \frac{C_D U_o}{H} \sin(\sigma t) \right]. \quad (4.9)$$

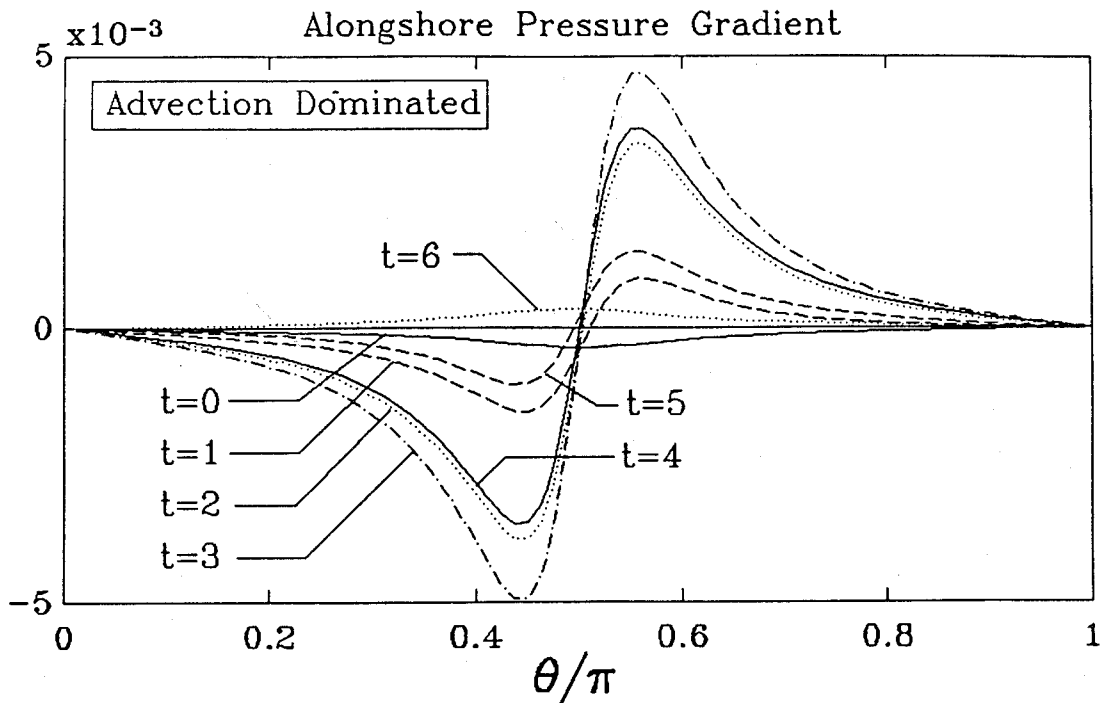


Figure 4-3: Pressure gradient along the boundary of an elliptic headland for an advection dominated case. θ/π is a dimensionless coordinate along the boundary of the headland, where 0.5 signifies the headland tip.

The three terms inside square brackets represent the contributions of time-dependence, advection, and friction to the pressure gradient. The nature of the pressure gradient along the boundary depends on the relative size of the terms in (4.9).

Figure 4-3 shows the pressure gradient along the boundary of the elliptic headland over the first half cycle when the dominant balance in the momentum equation is between advection and pressure gradient. This case indicates that when advection dominates the contributions of friction and time-dependence, the pressure gradient over much of the tidal cycle changes from strongly favoring (accelerating) to strongly adverse (decelerating) near the tip of the headland. The only exception is at the beginning of the cycle ($t = 0$ hours), when the pressure gradient is negative along the entire boundary, accelerating the flow from slack water.

Figure 4-4 illustrates the case where frictional effects dominate advective and time de-

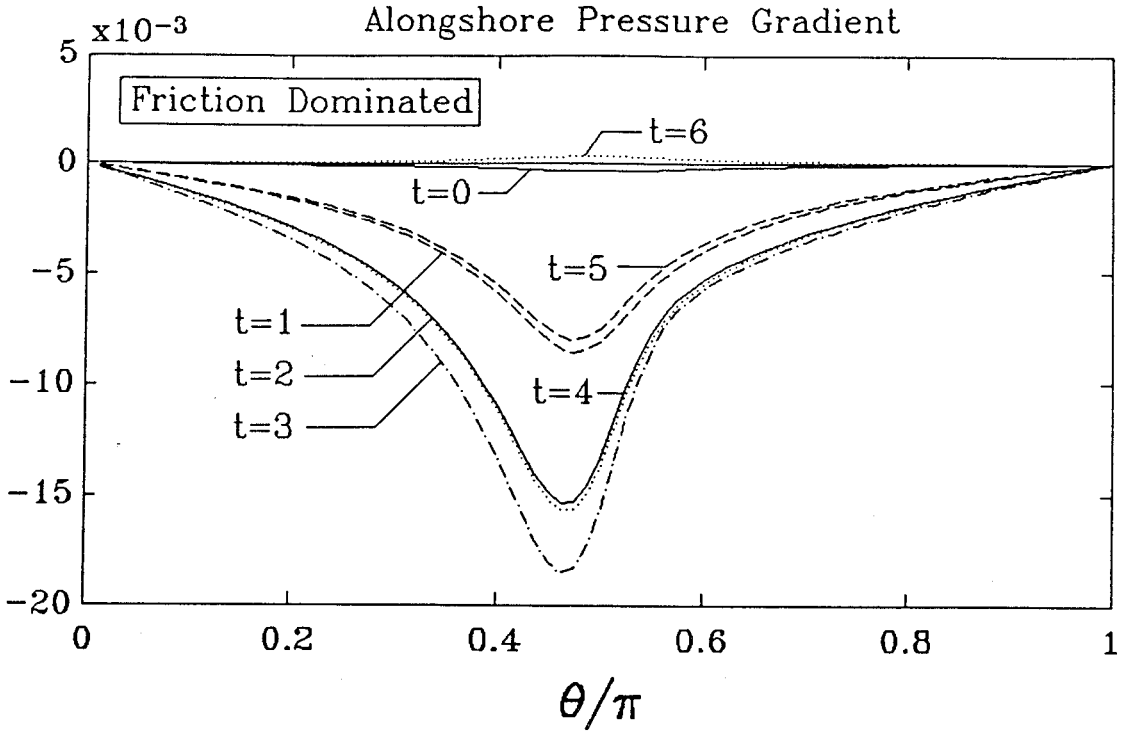


Figure 4-4: Pressure gradient along the boundary of an elliptic headland for a friction dominated case. θ/π is a dimensionless coordinate along the boundary of the headland, where 0.5 signifies the headland tip.

pendent effects. Because of the dominance of friction, the free-stream pressure gradient is nearly in phase with the flow around the headland. A negative free-stream pressure gradient occurs over the entire half cycle which is strong enough to overcome the positive contribution downstream of the headland. An adverse pressure gradient at the tip, therefore, never occurs.

Figure 4-5 illustrates the case where time-dependence dominates advective and frictional effects. Because of the dominance of time-dependence, the free-stream pressure gradient is nearly out of phase with the flow around the headland. A negative free-stream pressure gradient exists over the first half of the half cycle, followed by a positive pressure gradient over the second half. A pressure minimum exists at the headland only at $t = 3$ hours, since the sign of the pressure gradient changes at nearly the same time along the entire headland.

In order for an adverse pressure gradient to occur at the tip of the headland over most of

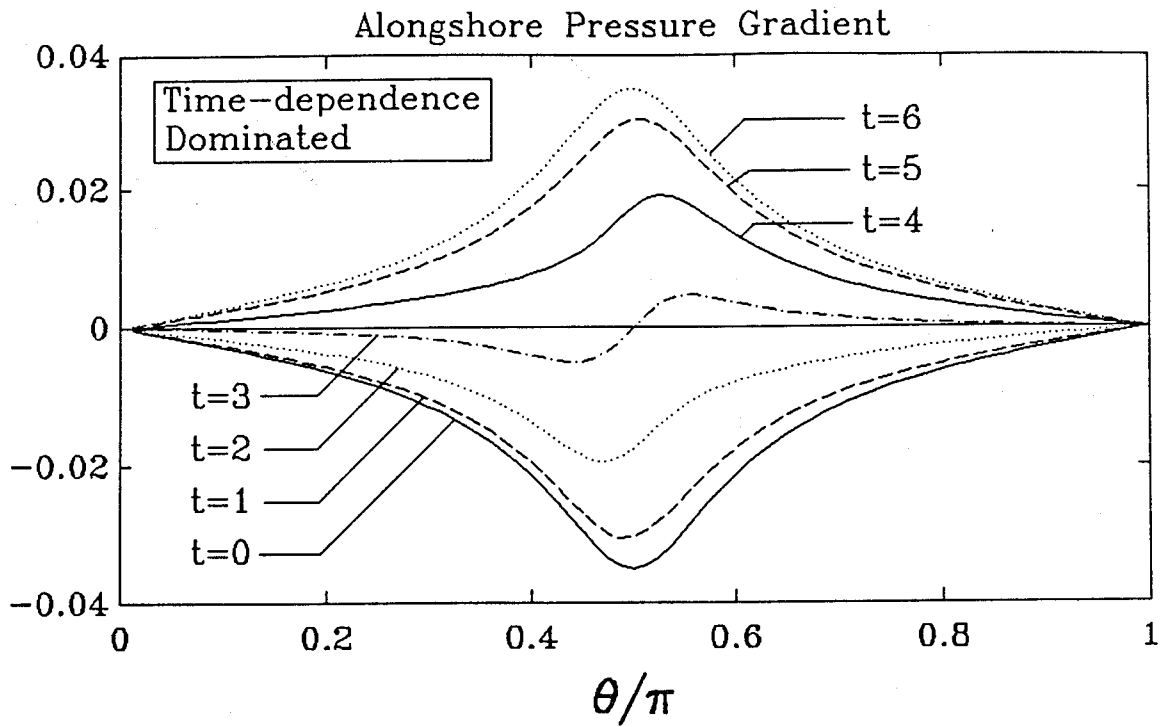


Figure 4-5: Pressure gradient along the boundary of an elliptic headland for a time-dependence dominated case. θ/π is a dimensionless coordinate along the boundary of the headland, where 0.5 signifies the headland tip.

the tidal cycle, the advection term must dominate the friction and time-dependence terms in (4.9). Evaluating the ratio of terms at the point where the velocity gradient is largest and taking cases where $\alpha > 4/3$, the resulting ratios are

$$\frac{\text{advection}}{\text{friction}} = \frac{H}{C_D a} \frac{3\sqrt{3}}{16} \frac{\alpha^2(1+\alpha)}{\sqrt{\alpha^2-1}} \approx \left[\frac{H}{C_D a} \right] \frac{\alpha(1+\alpha)}{3}, \quad (4.10)$$

$$\frac{\text{advection}}{\text{time dependence}} = \frac{U_o}{\sigma a} \frac{3\sqrt{3}}{16} \frac{\alpha^2(1+\alpha)}{\sqrt{\alpha^2-1}} \approx \left[\frac{U_o}{\sigma a} \right] \frac{\alpha(1+\alpha)}{3}. \quad (4.11)$$

The essentially quadratic dependence on the aspect ratio α in both (4.10) and (4.11) indicates that advection will quickly dominate friction and time dependence as the aspect ratio increases. The physical interpretation is that as the sharpness of the headland increases, the increased irrotational velocity at the headland tip causes the pressure to drop as the square of the velocity through the Bernoulli effect.

Equations (4.10) and (4.11) indicate that two nondimensional parameters are important in addition to α . For a fixed headland shape, the importance of advection to friction, from (4.10), is measured by the nondimensional quantity

$$Re_f \equiv \left[\frac{H}{C_D a} \right], \quad (4.12)$$

which is an equivalent Reynolds number based on bottom friction instead of viscosity. This is directly analogous to the ‘‘island wake parameter’’ defined by Wolanski et al. (1984). Increasing depth, decreasing drag coefficient and decreasing headland length all act to increase the importance of advection relative to friction. The importance of advection to time dependence for a fixed headland shape, from (4.11), is measured by

$$K_c \equiv \left[\frac{U_o}{\sigma a} \right], \quad (4.13)$$

the Keulegan-Carpenter number, which has been shown to indicate the nature of oscillatory viscous flow around cylinders at high Reynolds number (Keulegan and Carpenter, 1958). Increasing flow speed, decreasing frequency, and decreasing headland length all act to increase the importance of advection relative to time dependence. For a given headland geometry, there are values of Re_f and K_c below which advection is dominated by friction and time-dependence and the transition from favoring to adverse pressure gradient near the headland tip will not occur. In the following sections, it will be shown that an equivalent statement is that there are values of Re_f and K_c below which flow separation will not occur.

4.2.2 The boundary layer

In irrotational flow, the currents slip freely along the frictionless side-walls of the channel. In a realistic tidal flow, however, there is some region near the boundary where the speed must approach zero. The decrease in flow speed can result from the influence of bottom friction in the shallow water near the coast, or along steep-sided coasts, from the horizontal momentum flux associated with a no-slip condition at the wall. From the point of view of vorticity dynamics, this boundary shear represents production of vorticity by the slope torque mechanism, and lateral diffusion of vorticity generated by the no-slip boundary condition. If the cross-shore extent of the high vorticity region is small compared to the alongshore scale of variation, then the dynamics are simplified considerably, and the region of high shear may be termed a "boundary layer".

In a boundary layer, derivatives with respect to the alongshore coordinate x_1 are generally much smaller than derivatives with respect to the cross-shore coordinate x_2 , which allows the governing equations to be expressed as

$$\frac{\partial u_1}{\partial t} + \frac{u_1}{s_1} \frac{\partial u_1}{\partial x_1} + \frac{u_2}{s_2} \frac{\partial u_1}{\partial x_2} = -\frac{g}{s_1} \frac{\partial \eta}{\partial x_1} - \frac{C_D |u_1| u_1}{h} + \frac{A_H}{s_2^2} \frac{\partial^2 u_1}{\partial x_2^2}, \quad (4.14)$$

$$-\frac{u_1^2}{s_1} \frac{\partial s_1}{\partial x_2} = -g \frac{\partial \eta}{\partial x_2}, \quad (4.15)$$

$$\frac{1}{s_1} \frac{\partial u_1 h}{\partial x_1} + \frac{1}{s_2} \frac{\partial u_2 h}{\partial x_2} = 0. \quad (4.16)$$

In the absence of bottom friction and bottom topography, these equations are known as Prandtl's boundary layer equations, and a detailed description of their derivation can be found in Batchelor (1967). In addition to a reduction in the number of terms, the equations are further simplified in that the pressure is approximately uniform across the layer. This can be seen by rewriting the x_2 momentum equation

$$-\frac{u_1^2}{r_c} = -\frac{g}{s_2} \frac{\partial \eta}{\partial x_2} \quad (4.17)$$

where r_c is the radius of curvature of the boundary. The difference between the pressure at the coast and at the edge of the boundary layer, from (4.17), is order $[\delta U_o^2 / r_c]$, where U_o is the velocity scale, and δ is the boundary layer scale. Taking the alongshore scale of pressure gradient variation to be a yields a difference in the alongshore pressure gradient

of order $[U_o^2/r_c][\delta/a]$. Assuming that the pressure gradient in the irrotational flow balances advection, the pressure gradient at the edge of the boundary layer is $[U_o^2/a]$. The fractional change of the alongshore pressure gradient across the boundary layer, therefore, is order $[\delta/r_c]$, which is small for the boundary layer theory to be valid. The pressure gradient in the boundary layer, therefore, may be considered constant across the layer. If δ is small compared to the scale of variation of the potential flow solution, then the potential flow solution may be evaluated at the boundary to determine the pressure gradient in the boundary layer.

The boundary layer thickness can be estimated by scaling the alongshore momentum equation (4.14) to determine at what point offshore the balance of terms departs from the dominant balance in the boundary layer. For oscillatory flow along a straight coastline with a vertical wall, the dominant balance at the wall is between the viscous term and the pressure gradient. The local time rate-of-change becomes larger with distance offshore, and becomes comparable to the viscous term when

$$\frac{\partial u_1}{\partial t} \approx \frac{A_H}{s_2^2} \frac{\partial^2 u_1}{\partial x_2^2}. \quad (4.18)$$

Scaling t by $1/\sigma$ and x_2 by δ_v , where δ_v is the viscous boundary layer thickness, results in the estimate

$$\delta_v = \sqrt{A_H/\sigma}. \quad (4.19)$$

For M_2 tides ($\sigma = 1.4 \times 10^{-4} \text{ s}^{-1}$) and eddy viscosity representing tidal turbulence ($A_H = 0.1\text{--}1 \text{ m}^2 \text{ s}^{-1}$, see section 3.2), (4.19) yields viscous boundary layer thicknesses of 25–85 m. If instead of viscous effects, the boundary layer is due to the effect of bottom friction and a shoaling bottom, the dominant balance near the boundary is between the bottom friction term and the pressure gradient. The local time rate-of-change term becomes comparable to the bottom friction term when

$$\frac{\partial u_1}{\partial t} \approx \frac{C_D |u_1| u_1}{h}. \quad (4.20)$$

For a linearly sloping bottom, the depth increases from 0 to depth H over a width W , and (4.20) is satisfied at a distance

$$\delta_f = \left[\frac{C_D U_o}{\sigma H} \right] W \quad (4.21)$$

from the boundary. Using the Case A values of $C_D = 2.5 \times 10^{-3}$, $U_o = 0.5 \text{ m s}^{-1}$, $\sigma = 1.4 \times 10^{-4} \text{ s}^{-1}$, $H = 20 \text{ m}$, and $W = 1000 \text{ m}$ (the width of the shoaling region along the leading edge of the headland), a width of 500 m is obtained, smaller than the width of the sloping region, but much larger than the width of the viscous boundary layer.

The estimates of boundary layer thickness (4.19) and (4.21) apply to straight coastlines, where advection is weak. Around a headland, however, advection dominates time-dependence when the expression in (4.11) is larger than one. In this case, for a shoaling bottom with bottom friction, the dominant balance near the coast is between bottom friction and the pressure gradient, and the boundary layer scale is estimated by the distance offshore at which bottom friction becomes comparable to advection. The ratio of advection to bottom friction is given by the expression in (4.10), and is equal to one at a distance

$$\delta_f = \left[\frac{C_D a}{H} \right] \frac{3}{\alpha(1 + \alpha)} W \quad (4.22)$$

from the boundary.

Determining the boundary layer thickness allows the average vorticity in the boundary layer to be estimated. Since the alongshore length scale is much greater than the thickness of the boundary layer, the vorticity is approximated by $\omega = -\partial u_1 / \partial x_2$. Thus the average vorticity in the boundary layer is simply U_1 / δ , where U_1 is the velocity at the edge of the boundary layer. Since U_1 scales with the forcing velocity U_o , the vorticity scales with U_o / δ .

One limitation of using the potential flow solution to estimate the nature of the boundary layer is that for tidal flow around sharp headlands, the boundary layer thickness estimated from (4.19-4.22) can be comparable to the spatial scale of variation in the potential flow solution. More accurate estimates of the pressure gradient and velocity at the edge of the boundary layer could be obtained by evaluating the potential flow solution at a distance δ from the boundary. The goal of this thesis, however, is to understand the physics rather than make quantitative predictions, and evaluation of the potential flow solution at the coast succeeds at identifying the important parameters controlling the pressure gradient along the boundary.

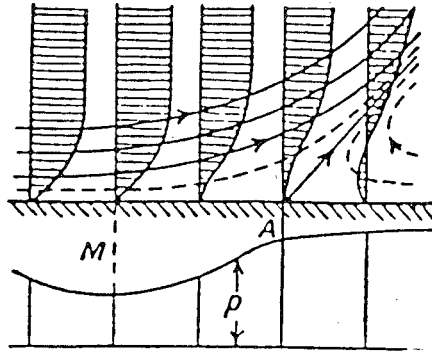


Figure 4-6: Schematic of flow separation. The figure shows profiles and streamlines of the current in the boundary layer, together with the pressure distribution at the edge of the layer. The point M is the point of minimum pressure, and the point A is the point of flow separation. From Prandtl (1952).

4.2.3 Flow separation with bottom friction

When flow separation occurs, boundary layer vorticity is injected into the interior, which dramatically affects the nature of the flow. As previously discussed, whether or not the flow separates depends critically upon the pressure gradient along the edge of the boundary layer. To illustrate the basic mechanism of boundary layer separation, consider the flow in a steady, viscous boundary layer under the influence of a pressure gradient that varies along the boundary as shown in Figure 4-6. Initially, the velocity at the edge of the boundary layer is increasing, and the pressure is decreasing. This favoring pressure gradient supplies the force necessary to balance the momentum flux into the boundary and keeps the flow in the boundary layer moving downstream. After the point where the flow at the edge of the boundary layer is at a maximum, however, the pressure increases, indicating an adverse pressure gradient. The flow in the boundary layer experiences an opposing force, and unless the momentum flux from offshore is strong enough, the flow eventually is made to turn back. The decrease in alongshore flow near the boundary must also be accompanied by an offshore flow to maintain continuity, which forces the interior flow away from the boundary. Thus the interior flow becomes “separated” from the boundary. The distance between the point of minimum pressure and the point of separation depends on the momentum flux into the

boundary layer from the offshore flow, as well as upstream characteristics of the boundary layer and the strength of the adverse pressure gradient. For viscous flow with no bottom friction, very close to the boundary the advection terms are small, and the momentum balance is between the pressure gradient and the horizontal stress divergence

$$\frac{dp}{dx_1} = A_H \frac{\partial^2 u_1}{\partial x_2^2}. \quad (4.23)$$

Note that an adverse pressure gradient requires only that the flow have negative curvature near the boundary, which in turn requires that the alongshore velocity profile have an inflection point – the flow need not reverse. Physically, this means that the flow does not separate if the cross-shore momentum flux is strong enough to balance the deceleration due to the adverse pressure gradient. In typical situations, however, separation occurs soon after pressure gradient reversal (Schlichting, 1968).

The discussion of flow separation to this point has not considered the effect of bottom friction. In shallow water, bottom friction plays an important role in the momentum equations, typically dominating except in the case of very large transverse shears. Including bottom friction has two effects on the boundary layer solution. The addition of friction changes the pressure gradient in relation to the velocity in the interior, as discussed in section 4.2.1, causing the point of minimum pressure to occur downstream of the point of maximum velocity. The second effect of friction is to alter the way momentum is extracted from the boundary layer, which changes the point of separation relative to the point of minimum pressure.

The relationship between the point of minimum pressure and the point of flow separation in a boundary layer controlled by bottom friction can be seen from an analysis of the boundary layer equations in the immediate vicinity of the boundary. If the depth goes to zero at the coast, the advective terms in (4.14) become negligibly small at some small distance from the coast, and if viscous effects are also negligible, the pressure gradient balances the bottom drag term

$$\frac{dp}{dx_1} = -\frac{C_D |u_1| u_1}{h}. \quad (4.24)$$

With no momentum flux from offshore to accelerate the flow, the flow must have the opposite sign as the pressure gradient. This means that in the absence of viscosity, bottom friction

causes the flow to separate at the point of minimum pressure (as soon as an adverse pressure gradient is established).

To investigate the combined effects of viscosity, headland shape, bottom friction and topography on the point of separation around a coastal headland, the steady forms of the boundary layer equations (4.14–4.16) were numerically integrated around an elliptic headland for a variety of different parameters. Starting from the upstream stagnation point ($\theta = 0$), the equations were marched downstream using the explicit finite-difference method of Schlichting (1968, p. 408). The velocity and pressure gradient at the edge of the boundary layer were specified by the potential flow results (4.6) and (4.9). The calculation proceeded until a flow reversal was encountered, indicating flow separation. The model breaks down past the point of flow separation as the boundary layer approximation becomes invalid, but this is of little concern since the primary goal is to study the point of flow separation itself.

The point of minimum pressure x_{mp} and the point of flow separation x_s were calculated for aspect ratios α of 1, 2 and 4. This was accomplished by holding the headland width b fixed at 8 km, and varying the length a . In each case, the width of the sloping region W (when present) was 1 km, and the boundary conditions were applied as 1.5 km. For each value of α , four cases were explored:

1. Flat bottom, eddy viscosity, no bottom friction ($H = 20$ m, $A_H = 1$ m² s⁻¹, and $C_D = 0$). This case represents separation of a lateral viscous boundary layer.
2. Flat bottom, eddy viscosity, bottom friction ($H = 20$ m, $A_H = 1$ m² s⁻¹, and $C_D = 2.5 \times 10^{-3}$). This case illustrates how friction causes a larger negative pressure gradient which shifts the point of minimum pressure downstream, but the boundary layer structure is still due to viscosity, since the bottom is flat.
3. Sloping bottom, no eddy viscosity, bottom friction ($H = 1$ m at coast, $H = 20$ m at 1 km, $A_H = 0$ m² s⁻¹, and $C_D = 2.5 \times 10^{-3}$). In this case, the bottom slopes to 1 m at the coast, and represents separation of a bottom frictional boundary layer. Since the eddy viscosity is zero, the no-slip boundary condition is not satisfied.
4. Sloping bottom, eddy viscosity, bottom friction ($H = 1$ m at coast, $H = 20$ m at 1 km, $A_H = 1$ m² s⁻¹, and $C_D = 2.5 \times 10^{-3}$). This case assesses the impact of satisfying the

Run	Headland Shape	Bottom Type	Eddy Viscosity	Bottom Friction	x_{mp} (km)	x_s (km)	$x_s - x_{mp}$ (km)
A1	smoothest ($\alpha = 1$)	flat	yes	no	0.00	2.29	2.29
A2	smoothest ($\alpha = 1$)	flat	yes	yes	6.28	7.53	1.25
A3	smoothest ($\alpha = 1$)	slope	no	yes	6.28	6.50	0.22
A4	smoothest ($\alpha = 1$)	slope	yes	yes	6.28	6.65	0.37
B1	smooth ($\alpha = 2$)	flat	yes	no	0.00	0.66	0.66
B2	smooth ($\alpha = 2$)	flat	yes	yes	0.55	1.40	0.85
B3	smooth ($\alpha = 2$)	slope	no	yes	0.55	0.69	0.14
B4	smooth ($\alpha = 2$)	slope	yes	yes	0.55	0.78	0.23
C1	regular ($\alpha = 4$)	flat	yes	no	0.00	0.29	0.29
C2	regular ($\alpha = 4$)	flat	yes	yes	0.03	0.32	0.29
C3	regular ($\alpha = 4$)	slope	no	yes	0.03	0.11	0.08
C4	regular ($\alpha = 4$)	slope	yes	yes	0.03	0.16	0.13

Table 4.1: Results of boundary layer model for flow separation around an elliptic cylinder with a width (offshore extent) b of 8 km. x_{mp} is the point of minimum pressure in km relative to the tip of the headland tip. x_s is the point of flow separation in km relative to the headland tip.

no-slip boundary condition.

Table 4.1 shows the results from these runs. The first set of runs was for the semi-circular headland ($\alpha = 1$). In the absence of friction (Run A1), the minimum pressure x_{mp} occurs at the headland tip, coinciding with the maximum potential flow. The distance between x_{mp} and the point of separation x_s is 2.29 km, which compares reasonably well with the 2.56 km result obtained by an approximate analytic technique (Schlichting, 1968). When the bottom remains flat, but friction is included (Run A2), x_{mp} moves downstream 6.28 km, and the distance between x_{mp} and x_s decreases to 1.25 km. This indicates that bottom friction not only causes the point of minimum pressure to move downstream, but causes the distance between the point of minimum pressure and flow separation to decrease. For a sloping bottom with 1 m water depth at the coast, bottom friction, and no eddy viscosity (Run A3), the distance between x_{mp} and x_s decreases further to 0.22 km. This reflects the fact that bottom friction causes the flow to separate at the point of minimum pressure as the depth at the coast goes to zero. With the inclusion of eddy viscosity and the no-slip boundary condition (Run A4), the distance between x_{mp} and x_s increases slightly

to 0.37 km. As previously discussed, including eddy viscosity allows momentum flux to maintain the boundary layer flow in the face of an adverse pressure gradient. The difference in the location of the separation point, however, is only 0.15 km. Thus when the depth at the coast is shallow, and the viscous layer thickness is less than the frictional layer thickness, bottom friction causes the flow to separate close to the point of minimum pressure, and eddy viscosity is relatively unimportant.

From the sharper headland runs, the principal results are that as the aspect ratio is increased, the point of minimum pressure rapidly approaches the headland tip, and the distance between the point of minimum pressure and the point of flow separation decreases. For example, with an aspect ratio $\alpha = 4$ and the same values of bottom friction, eddy viscosity, and bottom slope as the smoother headland cases (Case C4), the point of minimum pressure occurs only 30 m from the headland tip, and the flow separates 130 m downstream.

For practical purposes it can be stated that for shallow depths at the coast, the flow separates near the point of minimum pressure (where the pressure gradient becomes adverse). In all the runs where the depth is shallow at the coast, the flow separates within a few hundred meters of the the point of minimum pressure, and as the aspect ratio increases, this distance decreases. While the location of the point of minimum pressure x_{mp} from section 4.2.1 depends on the the frictional Reynolds number $[H/C_D a]$ and the Keulegan-Carpenter number $[U_o/\sigma a]$, it is especially sensitive to the aspect ratio α , and it approaches the tip of the headland as α increases. Thus the point of flow separation also approaches the tip as the aspect ratio increases.

4.3 Vorticity evolution in the interior

Once it is determined that flow separation occurs, the next important step is to investigate the evolution of boundary layer vorticity injected into the interior at the point of flow separation. The evolving distribution of the injected vorticity depends on wrapping up of the vorticity sheet to form a start-up eddy, advection by the interior tidal flow, interaction of the eddy with other eddies, damping by bottom friction, and diffusion by horizontal viscosity.

The maximum distance the vorticity can travel from the headland as the result of tidal

advection is set by the tidal excursion ℓ_t defined by $[2U_o/\sigma]$. The bottom frictional decay scale ℓ_f is equal to $H/2C_D$ (see section 3.4.1), and if the decay scale is less than the tidal excursion, the extent of the vorticity is limited to this length. The ratio of these length scales is proportional to $K_c/Re_f = [C_D U_o/\sigma H]$, the ratio of the Keulegan-Carpenter number to the frictional Reynolds number. If $[K_c/Re_f]$ is small, then vorticity produced during subsequent half cycles can interact. If $[K_c/Re_f]$ is large, then vorticity is effectively damped within a half cycle, and vorticity produced during subsequent half cycles cannot interact.

When the frictional decay scale is much shorter than the tidal excursion ($[K_c/Re_f] \ll 1$), then the vorticity extent is limited by bottom friction. The vorticity distribution is quasi-steady, and vorticity produced during one half cycle is effectively damped over the course of a tidal cycle. Vorticity produced on succeeding tidal cycles, therefore, will not interact. The extent of the vorticity relative to the headland length scale a is expressed by $Re_f = [H/C_D a]$, the frictional Reynolds number. This is the same parameter that appeared in section 4.2.1, where it determined the occurrence of flow separation when friction was more important than time-dependence. Thus if the frictional decay scale is much shorter than the tidal excursion, the structure of the wake for a given headland shape (a fixed aspect ratio) primarily depends on the frictional Reynolds number Re_f . An analogous parameter was proposed by Wolanski et al. (1984) to control the nature of island wakes in steady flow. For $Re_f \ll 1$, the flow does not separate since an adverse pressure gradient cannot develop. For $Re_f \approx 1$ the maximum extent of the vorticity injected at the point of flow separation becomes comparable to the length scale a of the headland, while for $Re_f \gg 1$, the vorticity plume extends many headland lengths downstream. The initial roll-up of the vortex sheet is unimportant in this regime, due to the quasi-steady nature of the frictionally controlled flow. The separation streamline, therefore, bounds a weak recirculation region downstream of the headland.

When the frictional decay scale is much larger than the tidal excursion ($K_c/Re_f \gg 1$), then vorticity produced during subsequent tidal cycles can interact, and the nature of the flow is controlled by the ratio of the tidal excursion to the headland length scale, or the Keulegan-Carpenter number $K_c = [U_o/\sigma a]$. This is the same parameter that appeared

in section 4.2.1, where it determined the occurrence of flow separation for the case where time-dependence dominated the effect of friction. This parameter has also been found to control the nature of oscillatory viscous flow past cylinders (Keulegan and Carpenter, 1958). For $K_c \ll 1$, the flow does not separate, since the curvature of the coastline is negligible over the length of the tidal excursion. For $K_c \approx 1$ the extent of the vorticity downstream is comparable to the length scale of the headland, and is thus dominated by the start-up eddy. Since vorticity is minimally damped over a tidal cycle, this eddy will interact with eddies produced on other cycles, and complex flow patterns result. For $K_c \gg 1$, the start-up eddy moves away from the headland, resulting in a wake that extends many headland lengths downstream. This whole wake structure is affected by the wake produced during the previous cycles, which again results in complicated flow patterns.

When the frictional length scale is comparable to the tidal excursion ($K_c/Re_f \approx 1$), both time dependence and friction are important in determining the structure of the vorticity in the interior. Friction is strong enough to prevent vorticity produced during subsequent half cycles to interact, but not strong enough to make time-dependent effects negligible. When the frictional length scale and the the tidal excursion are much smaller than the length scale of the headland ($K_c \ll 1$ and $Re_f \ll 1$), then flow separation will not occur. If the frictional length scale and the tidal excursion are comparable to the headland length a ($K_c \approx 1$ and $Re_f \approx 1$), then as the vorticity layer peels away from the boundary, it wraps up, forming a large blob of vorticity defining the start-up eddy. The start-up eddy grows to a size comparable to the headland scale, forming a strong recirculation region downstream of the headland. When the frictional length scale and the tidal excursion are much larger than the length scale of the headland, the start-up eddy may move downstream of the headland so that a weak recirculation zone behind the headland is again established.

4.4 Parameter dependence

4.4.1 Introduction

The preceding sections have identified important parameters relating to flow separation and the evolution of vorticity in the interior. In this section, the parameters are first

reviewed, then a number of numerical simulations are presented which illustrate the effect these parameters have on the nature of the flow.

4.4.2 Important length scales and dimensionless parameters

The numerical model is fully specified by 10 physical parameters. The model geometry is described by the headland length a and width b , the depth of the interior H , the depth at the coast H_o , and the width of the sloping bottom region W . Bottom friction and horizontal eddy viscosity are specified by C_D and A_H . The tidal forcing is specified by U_o and σ . The Earth's rotation is specified by the Coriolis parameter f .

The idealized model of flow separation and consideration of transport and damping of vorticity in the interior have indicated that three nondimensional parameters are of primary importance in determining the nature of the flow. To review, these parameters are:

1. The aspect ratio $\alpha = [b/a]$. The ratio of the headland width (offshore extent) to headland length (alongshore extent), which strongly influences the pressure gradient in the vicinity of the headland tip, which in turn is an important quantity in determining flow separation.
2. The frictional Reynolds number $Re_f = [H/C_D a]$. The ratio of the frictional length scale to the headland length scale, which determines whether flow separation occurs and determines the nature vorticity in the interior when the frictional length scale is much less than the tidal excursion.
3. The Keulegan-Carpenter number $K_c = [U_o/\sigma a]$. The length of the tidal excursion relative to the length scale of the headland, which determines whether flow separation occurs and determines the nature of vorticity in the interior when the frictional length scale is much greater than the tidal excursion.

The ratio $[K_c/Re_f] = [C_D U_o/\sigma H]$ is also a useful parameter, as it indicates the degree to which vorticity produced during successive half-cycles can interact. If $[K_c/Re_f] \ll 1$, then frictional damping is negligible over the tidal cycle and eddies may interact. If $[K_c/Re_f] \gg 1$, then vorticity is strongly damped over the tidal cycle and eddies decay before they can interact.

Associated with these three parameters are four important length scales: the headland length a (the alongshore extent), the headland width b (the offshore extent), the frictional length scale $\ell_f \equiv [H/2C_D]$, and the tidal excursion $\ell_t \equiv [2U_o/\sigma]$.

Other length scales that have a less pronounced effect on the solution are the width of the sloping bottom region W , and the viscous length scale $\ell_v = \sqrt{A_H/\sigma}$. The effect of horizontal viscosity can also be measured by the Reynolds number $Re = [U_o a/A_H]$, measuring the importance of advection relative to viscosity. In investigating the parameter dependence, the nondimensional parameters are varied by changing the dimensional quantities C_D , a , A_H , U_o , and σ .

4.4.3 Simulations with varying parameters

The object of the parameter dependence study was to investigate the nature of the flow for a range of variables representing typically occurring headland tidal flows in coastal embayments. Most parameters were varied by factors of four, corresponding to water depths of 10–40 m, current amplitudes of 0.25–1.00 m s⁻¹, tidal frequencies of diurnal to quarter-diurnal, and headland aspect ratios of 2–8. The eddy viscosity was varied by a factor of 10, and a few additional runs were performed with very high and very low friction, mainly to compare with the results of viscous flow around bluff bodies, which will be discussed in section 4.7. The relevant length scales for the simulations are displayed in Table 4.2. The equivalent information, expressed in terms of physical variables and nondimensional parameters, is listed in Table 4.3. The cases are grouped into four categories: frictional variation, headland length variation, eddy viscosity variation and tidal excursion variation. The effect on the solution is assessed by the effect on the vorticity field at the end of eastward flow, as this represents the maximum extent of vorticity away from the headland and indicates whether flow separation has occurred.

Basic case

For the basic case, the tidal excursion is 7.2 km, the frictional length scale is 4.0 km and the length of the headland is 2.0 km. Case 1 is equivalent to the case study described in detail in Chapter 3 except that to facilitate comparison with the varying aspect ratio cases, the bathymetry is parallel to the coast, and the width of the shoaling region W is 1 km.

Case	a	b	ℓ_t	ℓ_f	ℓ_v	W	Description
1	2	8	7.1	4.0	0.09	1	basic case
2	2	8	7.1	2.0	0.09	1	high friction
3	2	8	7.1	0.4	0.09	1	very high friction
4	2	8	7.1	8.0	0.09	1	low friction
5	2	8	7.1	8.0	0.27	1	low friction, high viscosity
6	2	8	7.1	40.0	0.19	1	very low friction
7	4	8	7.1	4.0	0.09	1	smooth headland
8	1	8	7.1	4.0	0.09	1	sharp headland
9	2	8	7.1	4.0	0.12	1	more viscosity
10	2	8	7.1	4.0	0.27	1	high viscosity
11	2	8	7.1	4.0	0.06	1	high frequency, strong current
12	2	8	14.2	4.0	0.12	1	low frequency
13	2	8	3.5	4.0	0.06	1	high frequency
14	2	8	∞	4.0	∞	1	steady flow
15	2	8	28.4	16.0	0.38	1	very low frequency & friction

Table 4.2: Length scales varied in simulations, all expressed in km, where a is the headland length (alongshore) scale, b is the headland width (offshore) scale, ℓ_t is the tidal excursion $[2U_o/\sigma]$, ℓ_f is the frictional decay scale $[H/2C_D]$, ℓ_v is the viscous scale \sqrt{AH}/σ , and W is the width of the sloping bottom.

The vorticity field at the end of the half cycle (slack water) shows that the start-up eddy is represented by a elongated blob of negative vorticity extending 5 km east of the headland tip with the eddy core ($-13 \times 10^{-4} \text{ s}^{-1}$) located 3 km east of the tip (Figure 4-7). The presence of the negative vorticity blob in the interior indicates that flow separation has occurred. The position of the blob indicates that friction is limiting the extent of vorticity. No vorticity from the eddy formed on the previous half cycle is observed, as the frictional length scale is smaller than the tidal excursion.

Frictional variation

In Cases 2-6, the drag coefficient was varied, changing the frictional length scale ℓ_f relative to the tidal excursion ℓ_t , the headland length a , and the other scales. Since ℓ_f is defined by $[H/2C_D]$, doubling the drag coefficient and holding the depth fixed is equivalent to holding the drag coefficient constant and halving the water depth. Thus the high friction cases can be alternatively viewed as shallow water cases, and the low friction cases as deep water cases.

Case	a	b	U_o	σ	C_D	A_H	α	Re_f	K_c	K_c/Re_f	Re
1	2	8	0.5	1.41	2.50	1	4	4.0	1.78	0.44	1000
2	2	8	0.5	1.41	5.00	1	4	2.0	1.78	0.88	1000
3	2	8	0.5	1.41	25.0	1	4	0.4	1.78	4.43	1000
4	2	8	0.5	1.41	1.25	1	4	8.3	1.78	0.22	1000
5	2	8	0.5	1.41	1.25	10	4	8.3	1.78	0.22	100
6	2	8	0.5	1.41	0.25	5	4	50.0	1.78	0.04	500
7	4	8	0.5	1.41	2.50	1	2	2.0	0.89	0.44	2000
8	1	8	0.5	1.41	2.50	1	8	8.3	3.56	0.44	500
9	2	8	0.5	1.41	2.50	2	4	4.0	1.78	0.44	500
10	2	8	0.5	1.41	2.50	10	4	4.0	1.78	0.44	100
11	2	8	1.0	2.82	2.50	1	4	4.0	1.78	0.44	1000
12	2	8	0.5	0.70	2.50	1	4	4.0	3.56	0.88	1000
13	2	8	0.5	2.82	2.50	1	4	4.0	0.89	0.22	1000
14	2	8	0.5	0.0	2.50	1	4	4.0	∞	∞	1000
15	2	8	0.5	0.35	2.50	1	4	16.0	7.12	0.44	1000

Table 4.3: Parameters varied in simulations. The physical variables are listed first, where a is the headland length scale (km), b is the headland width scale (km), U_o is the amplitude of the forcing tidal current (m s^{-1}), σ is the tidal frequency ($\times 10^{-4} \text{ s}^{-1}$), C_D is the depth-averaged drag coefficient ($\times 10^{-3}$), A_H is the horizontal eddy viscosity ($\text{m}^2 \text{ s}^{-1}$). The nondimensional parameters are also listed, where α is the aspect ratio of the headland [b/a], Re_f is the frictional Reynolds number [$H/C_D a$], K_c is the Keulegan-Carpenter number [$U_o/\sigma a$], and Re is the Reynolds number [$U_o a/A_H$].

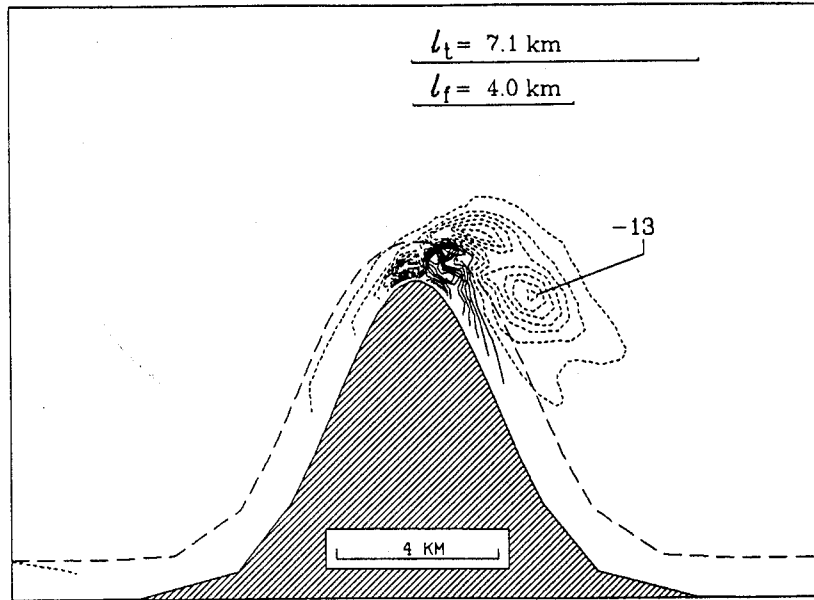


Figure 4-7: Vorticity at slack water (6 lunar hours) for Case 1, the basic case. Solid contours indicate positive vorticity, dashed contours indicate negative vorticity, and the contour interval is $2 \times 10^{-4} \text{ s}^{-1}$.

When l_f is decreased to 2 km (Case 2), the vorticity patch at the end of the half cycle has a reduced extent, and the extremum of $-9 \times 10^{-4} \text{ s}^{-1}$ is 30% weaker than in Case 1 (Figure 4-8). The flow has clearly separated, and again l_f is small enough to limit the extent of the vorticity patch, but not small enough to prevent flow separation.

When l_f is decreased to 0.4 km (Case 3), the vorticity at slack is limited to the sloping region around the headland tip, with a minimum value of only $-5 \times 10^{-4} \text{ s}^{-1}$ (Figure 4-9). The vorticity is completely contained over the sloping bottom region, and the friction is strong enough that flow separation does not occur. The vorticity field is nearly symmetric with respect to the headland, reflecting the fact that the vorticity produced over the sloping bottom is damped over a scale (0.4 km) that is much less than the headland length scale a (2 km).

When l_f is increased to 8.0 km (Case 4), the maximum magnitude ($-25 \times 10^{-4} \text{ s}^{-1}$) and extent (7 km) of the negative vorticity patch increase, and a positive vorticity blob of $3 \times 10^{-4} \text{ s}^{-1}$ generated during the previous half cycle is evident (Figure 4-10). With the

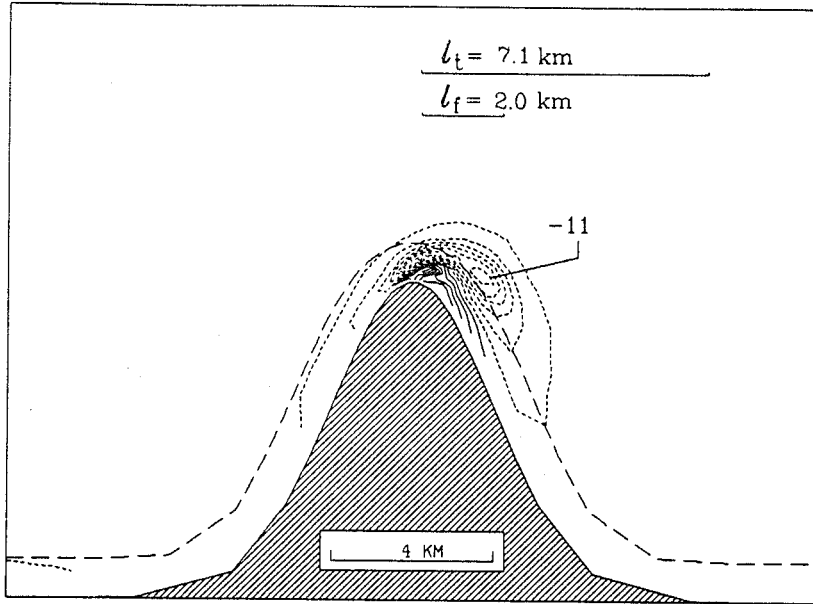


Figure 4-8: Vorticity at slack water for Case 2, which has a frictional length scale half that of Case 1.

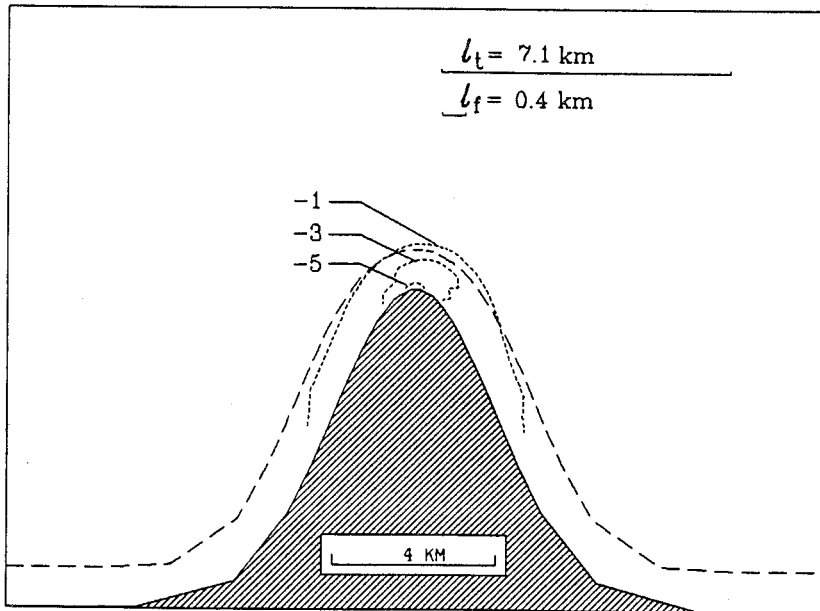


Figure 4-9: Vorticity at slack water for Case 3, which has a frictional length scale one tenth that of Case 1.

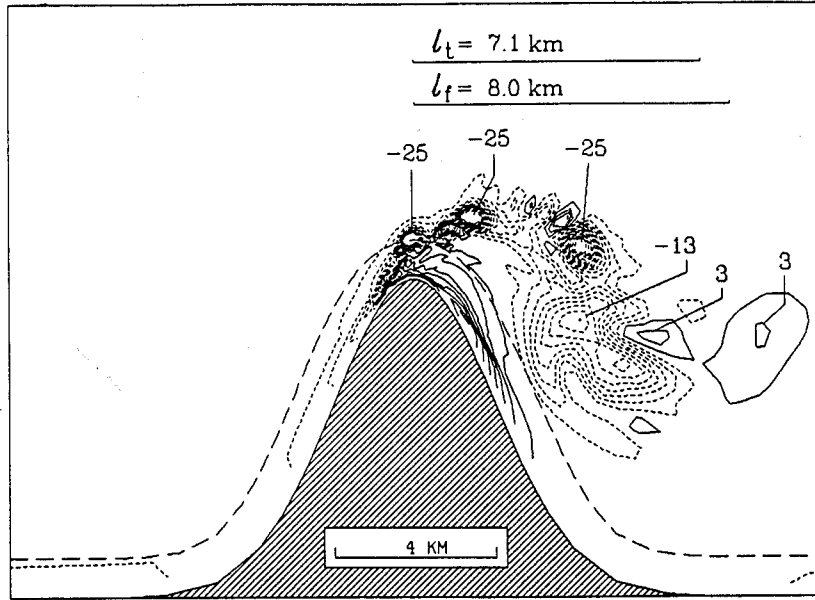


Figure 4-10: Vorticity at slack water for Case 4, which has a frictional length scale twice that of Case 1.

frictional decay scale slightly larger than the tidal excursion (7.1 km), the extent of the vorticity is no longer limited by ℓ_f . The most striking aspect of Figure 4-10 is, however, that instead of forming one large patch, the vorticity pinches off into four distinct blobs at intervals of 1–2 km, resulting in a markedly different distribution of vorticity. The peak vorticity in the three blobs nearest the headland is less than $-25 \times 10^{-4} \text{ s}^{-1}$, while the blob with the furthest downstream extent has a value of $-13 \times 10^{-4} \text{ s}^{-1}$. The formation of these blobs is a result of instability of the free shear layer formed when the flow separates, as will be discussed in section 4.5.

To see if horizontal eddy viscosity affected the generation of multiple eddies, Case 4 was rerun with an eddy viscosity of $10 \text{ m}^2 \text{ s}^{-1}$ (Case 5). Figure 4-11 shows that the mechanism responsible for the small-scale roll-up of the shear layer is destroyed, and the vorticity forms a large smoothly varying patch with a minimum value of $-13 \times 10^{-4} \text{ s}^{-1}$. It is apparent that in addition to smoothing high-wavenumber structure, increasing eddy viscosity stabilizes the shear layer, preventing the formation of multiple eddies.

When ℓ_f is increased to 40 km (Case 6), the vorticity decays over a length scale much

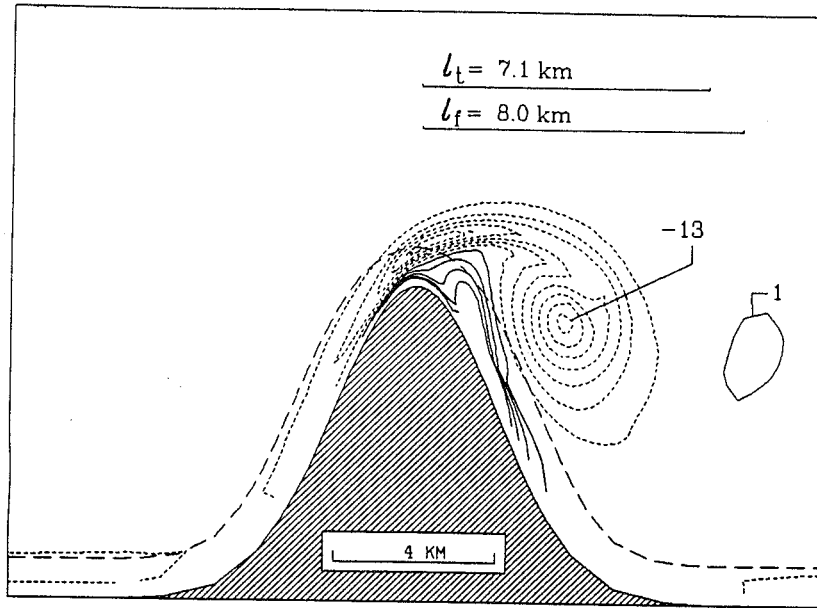


Figure 4-11: Vorticity at slack water for Case 5, which has a frictional length scale twice that of Case 1, but with ten times the level of eddy viscosity.

longer than the tidal excursion, and an eddy produced on a given half cycle can significantly interact with eddies formed during subsequent half cycles. The vorticity at the end of eastward flow shows that the clockwise start-up eddy produced on the eastward flow has paired with the counterclockwise eddy produced on the preceding westward flow, and the self-induced velocity of these eddies is propelling them toward the east like a smoke ring (Figure 4-12). In this run the eddy viscosity was set at $5 \text{ m}^2 \text{ s}^{-1}$ to prevent multiple eddies from forming on each half cycle. The generation of multiple eddies during each half cycle was suppressed because the model cannot accurately reproduce the long-term behavior of these small-scale structures. A sequence of snapshots of the vorticity field over a full tidal cycle shows the interaction of eddies formed on opposite sides of the headland (Figure 4-13). At the beginning of the tidal cycle (0 hours) there is a strong counterclockwise eddy signified by a blob of strong positive vorticity ($> 25 \times 10^{-4} \text{ s}^{-1}$) located to the west of the headland tip (Figure 4-13a). At maximum eastward flow (3 hours), this counterclockwise eddy interacts with the forming clockwise eddy (Figure 4-13b). The induced motion of these eddies on each other propels them to the east, so that by the end of the half cycle

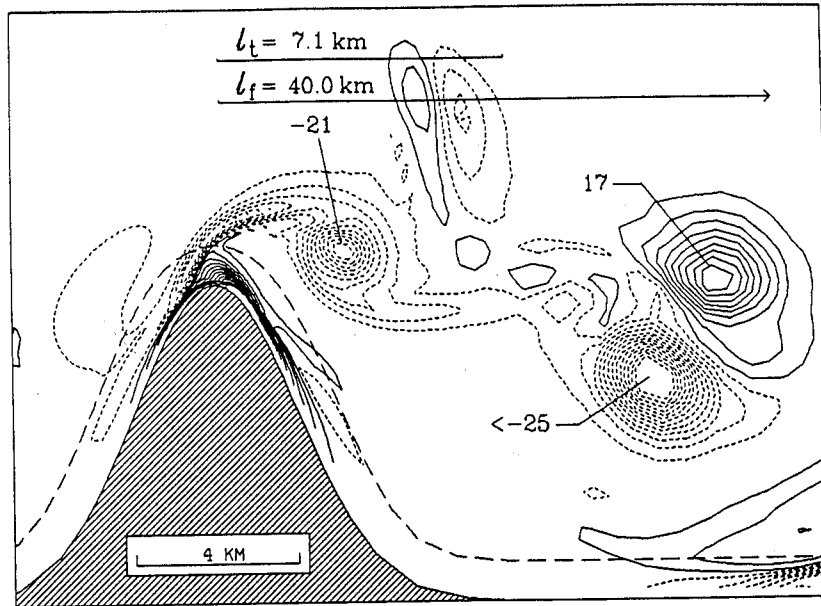


Figure 4-12: Vorticity at slack water for Case 6, which has a frictional length scale ten times that of Case 1 and five times the level of eddy viscosity as Case 1.

they have moved 10 km downstream (Figure 4-13c). After the eddy pair has advected away from the headland, the flow is still eastward at the tip, and a second clockwise eddy forms with a considerably diminished strength. This eddy advects around the tip of the headland when the tide turns, but it is much weaker than the developing counterclockwise eddy and therefore has no significant influence on its behavior (Figure 4-13d). Since the induced velocity of the clockwise eddy is weak, the counterclockwise eddy remains close to the headland (Figure 4-13e). Thus on the following half cycle, the strong counterclockwise eddy will interact with the clockwise eddy, the pair will migrate off to the east, and the whole cycle will repeat. The solution to this very low friction case is therefore an asymmetric one in which a pair of eddies propagates off to the east during each tidal cycle.

Headland length variation

In Cases 7 and 8, the headland length a is varied. Changing the length scale a changes the aspect ratio α , which was shown in section 4.2.1 to have a strong influence on the pressure gradient along the headland. The pressure gradient, in turn, plays an important role in flow separation.

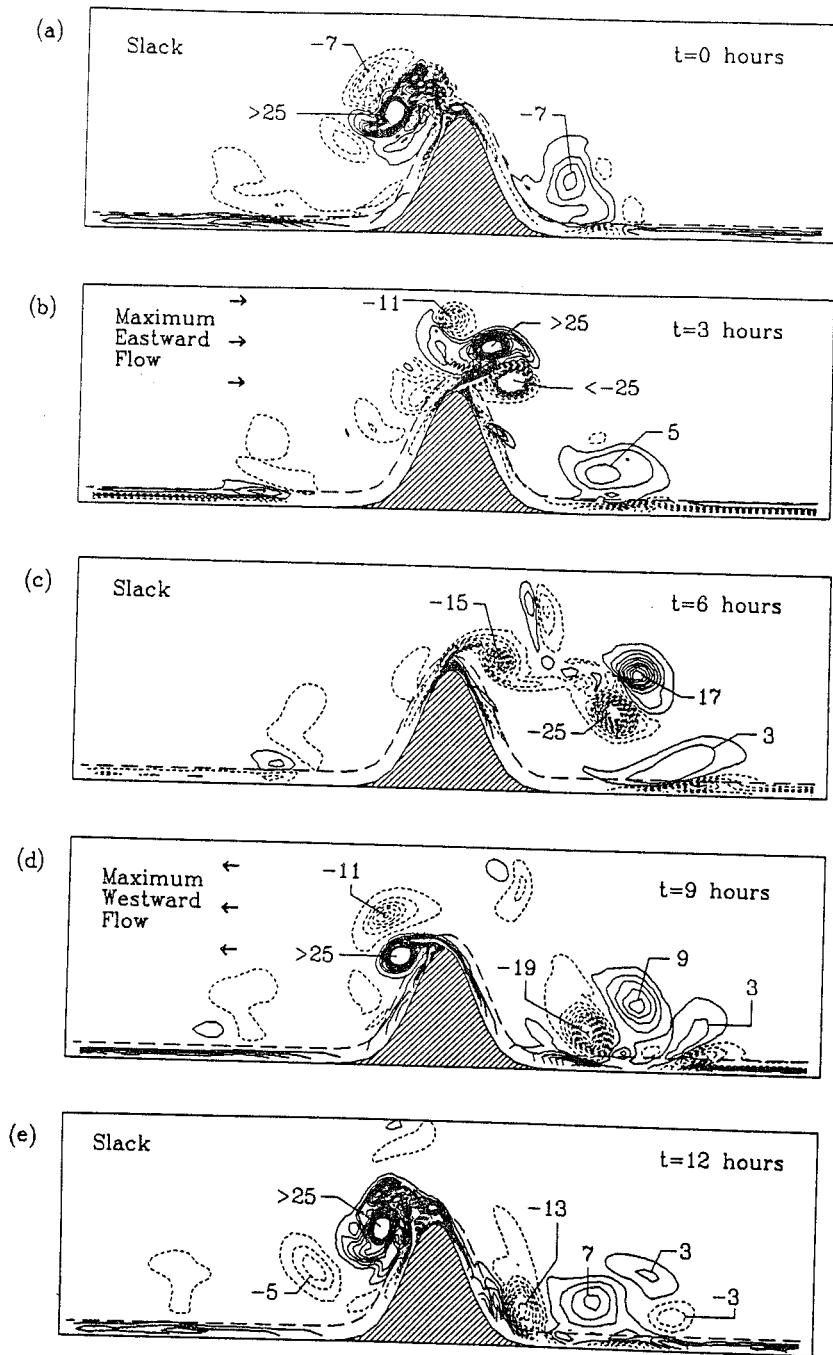


Figure 4-13: Vorticity at (a) 0 hours, (b) 3 hours, (c) 6 hours, (d) 9 hours and (e) 12 hours for Case 6. This case has ten times the frictional length scale and five times the eddy viscosity of Case 1.

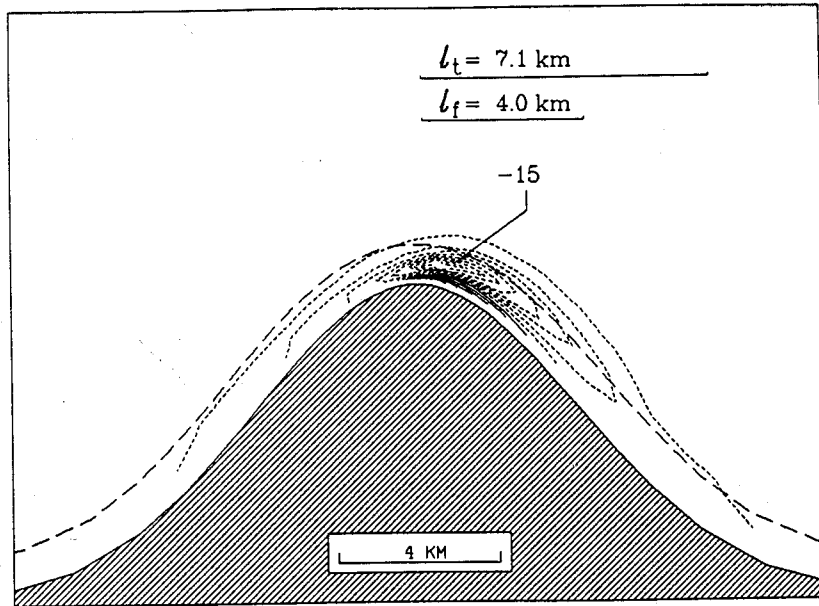


Figure 4-14: Vorticity at slack water for Case 7, which has a headland length scale twice that of Case 1 (half the aspect ratio).

When a is increased to 4 km (Case 7), the vorticity has a minimum of $-15 \times 10^{-4} \text{ s}^{-1}$, but remains chiefly in the boundary layer (Figure 4-14). Decreasing the aspect ratio to $\alpha = 2$ has reduced the magnitude of the pressure gradient at the tip enough so that flow separation does not occur.

When a is decreased to 1 km (Case 8), the nature of the vorticity is not much different from Case 1 (Figure 4-15). The extent of the patch is somewhat larger than in Case 1, while the maximum magnitude is slightly reduced ($11 \times 10^{-4} \text{ s}^{-1}$). The shape of the patch is more circular and although the location of the maximum relative to the headland tip is the same as in Case 1, it is further from the lee boundary due to the sharper turning of the coast. Thus it appears likely that above a certain value, higher aspect ratios do not significantly affect the solution.

Eddy viscosity variation

In the low friction cases, increasing eddy viscosity by a factor of 10 was seen to change the nature of the solution dramatically (Cases 4 and 5). Changing the viscosity by a factor of 2 or so, however, has little effect at the Case 1 parameter setting. Case 9 has twice the

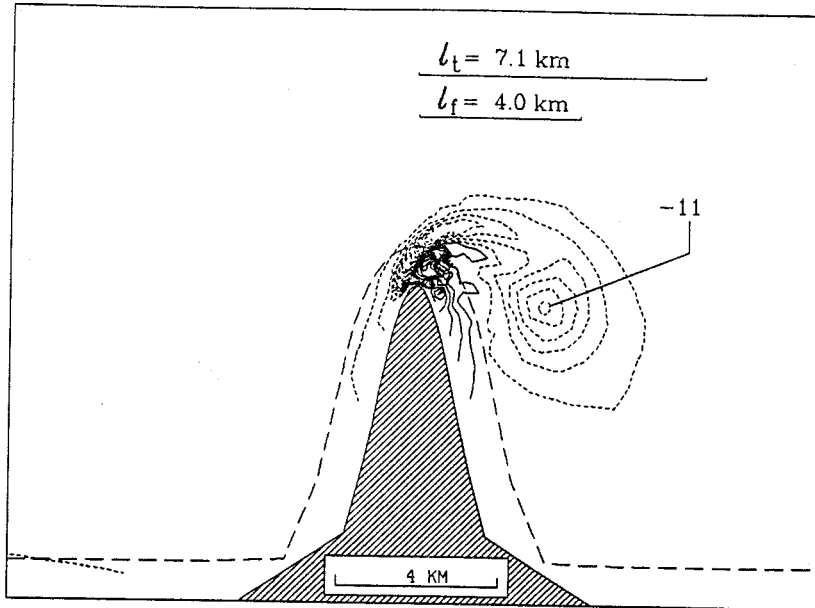


Figure 4-15: Vorticity at slack water for Case 8, which has a headland length scale half that of Case 1 (twice the aspect ratio).

eddy viscosity of Case 1, but the only observable difference is a slight smoothing of the peak vorticity (Figure 4-16). Increasing the eddy viscosity by a factor of 10 over Case 1 (Case 10) wipes out the high-wavenumber structure near the headland tip and leads to a smoothly varying vorticity field, as in Case 5 (Figure 4-17).

Tidal excursion variation

The tidal excursion $l_t \equiv [2U_o/\sigma]$ depends on both the frequency and amplitude of the forcing velocity. While changing the amplitude affects only the tidal excursion, changing the frequency affects the viscous scale $l_v \equiv [\sqrt{A_H/\sigma}]$ as well. Case 8 showed that the solution is relatively insensitive to changing l_v by factors of two, however, so that the principal effect of varying σ is to alter l_t . This is illustrated by Case 11, in which both the velocity and frequency are doubled, leaving the tidal excursion and frictional length scales unaffected. Figure 4-18 shows that the vorticity field is very similar in structure to that of Case 1. The vorticity minimum in Case 11 is $-25 \times 10^{-4} \text{ s}^{-1}$, nearly twice that of Case 1. This is because the vorticity scales as U_o/δ , where δ is the boundary layer thickness. Since δ was nearly the same in Cases 1 and 11, doubling U_o doubles the vorticity.

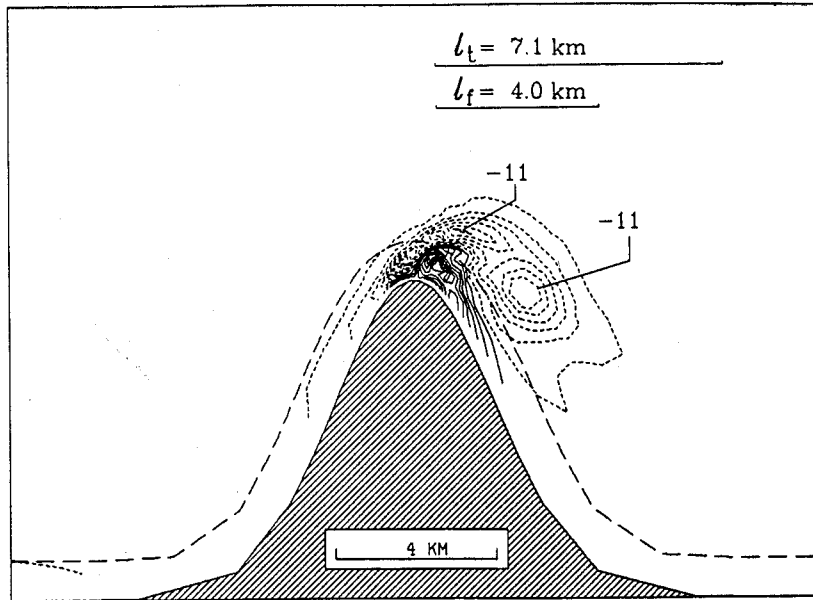


Figure 4-16: Vorticity at slack water for Case 9, which has twice the eddy viscosity of Case 1.

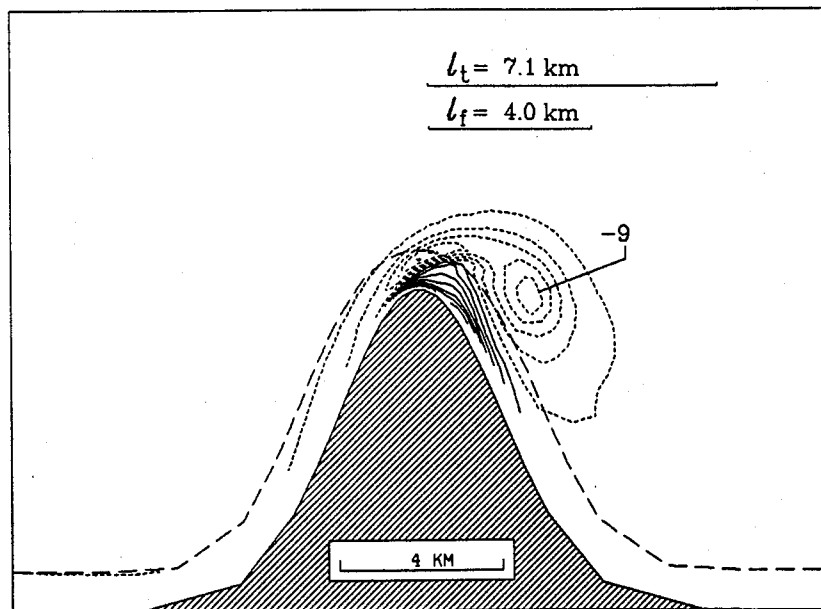


Figure 4-17: Vorticity at slack water for Case 10, which has ten times the eddy viscosity of Case 1.

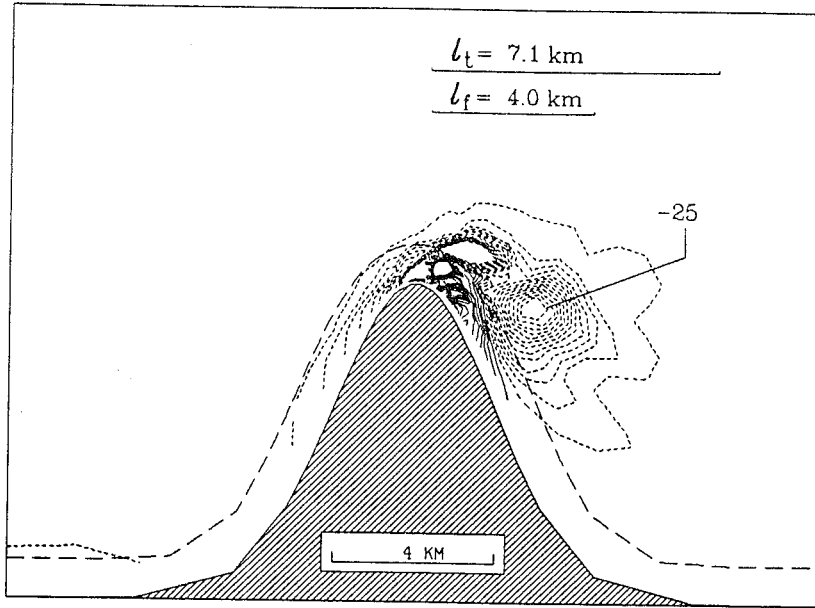


Figure 4-18: Vorticity at slack water for Case 11, which has twice the forcing amplitude and frequency of Case 1, hence the same tidal excursion (and frictional scale).

If U_o or σ is varied separately, the primary effect of changing the tidal excursion is to alter the spatial extent of the vorticity patch. When the tidal excursion is increased to 14 km (Case 12), the vorticity patch extends 6 km downstream and has a maximum magnitude of $5 \times 10^{-4} \text{ s}^{-1}$ located 4 km downstream (Figure 4-19). Though the tidal excursion is twice that of Case 1, the location of the minimum vorticity in Case 12 is less than 1 km different than the location of the minimum in Case 1. This is because l_f is less than l_t , and thus the frictional length scale limits the downstream extent of vorticity. The vorticity is weaker because the ratio of the frictional length scale to the tidal excursion has decreased (K_c/Re_f has increased).

When the tidal excursion is decreased to 3.5 km (Case 13), the vorticity extends to the length of the tidal excursion and has a minimum of $-25 \times 10^{-4} \text{ s}^{-1}$ (Figure 4-20). The vorticity is stronger because the ratio of the frictional length scale to the tidal excursion has increased (K_c/Re_f has decreased).

When the tidal excursion is increased to the point where it is much larger than the frictional length scale, the limit of steady flow (Case 14) is approached (Figure 4-21). The

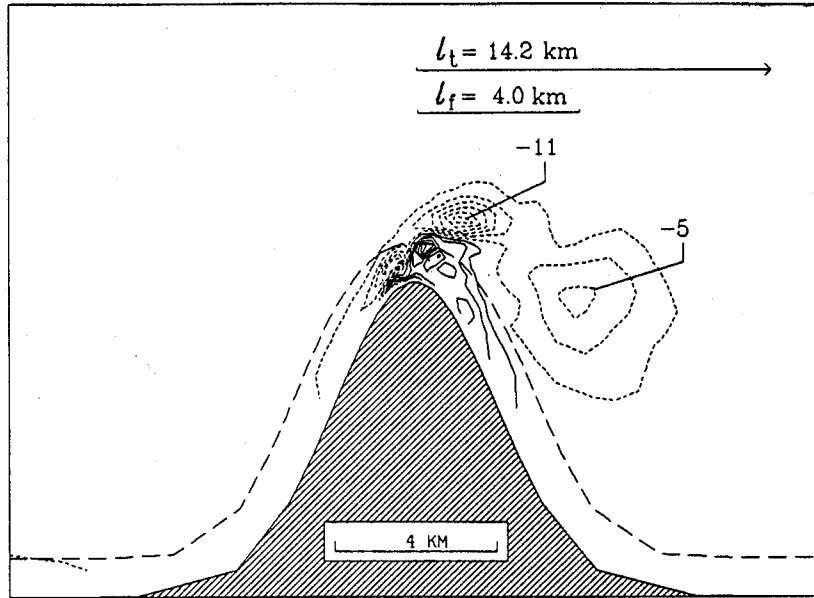


Figure 4-19: Vorticity at slack water for Case 12, which has half the forcing frequency of Case 1, hence twice the tidal excursion.

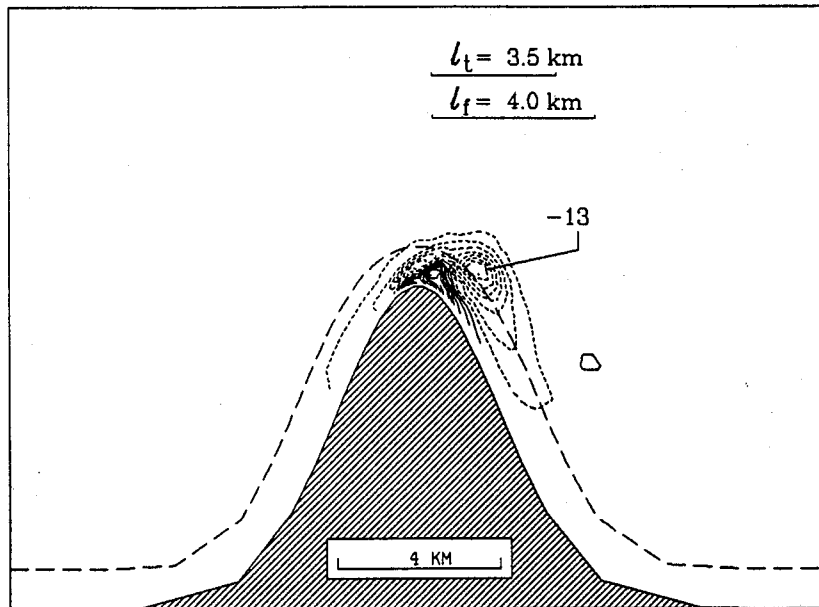


Figure 4-20: Vorticity at slack water for Case 13, which has twice the forcing frequency of Case 1, hence half the tidal excursion.

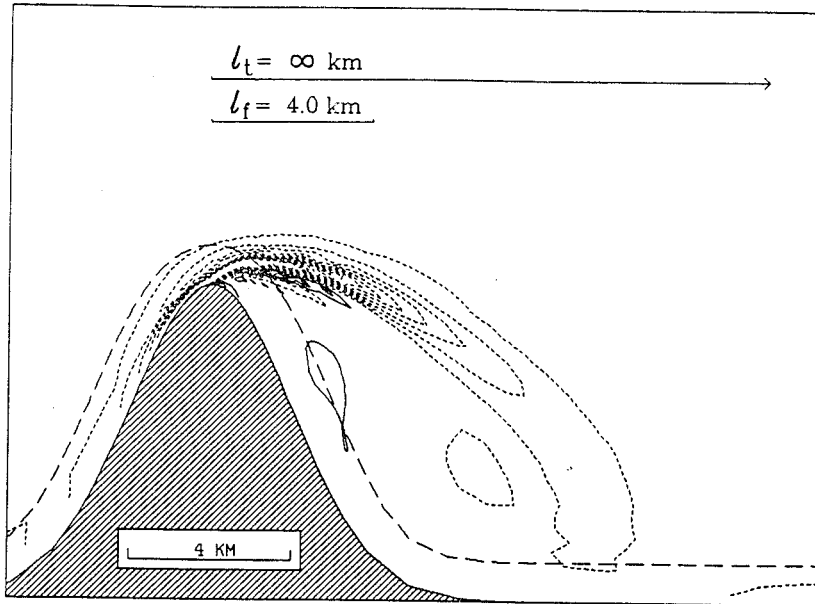


Figure 4-21: Vorticity for Case 14, steady flow. The frictional length scale is the same as in Case 1.

concentrated vorticity associated with the start-up eddy is not apparent, and the extent of the vorticity is limited by the frictional length scale.

When both the tidal excursion and the frictional length scale become much larger than the headland length scale (Case 15), the vorticity field illustrates how the start-up eddy moves away from the headland (Figure 4-22). The position of the eddy at slack water is about half a tidal excursion downstream of the headland, which indicates that the eddy travels more slowly than the far-field flow. Examining the vorticity field for the same case at maximum eastward flow reveals that the eddy had already reached the position it occupied at slack water (Figure 4-23). This indicates that as the eastward current weakens after maximum flow, the eddy ceases to propagate downstream. While the interior flow acts to move the eddy toward the east, the interaction of the eddy with its image vortex across the southern boundary acts to move the eddy toward the west. The result is that the extent of the eddy is significantly less than either the frictional length scale or the tidal excursion.

The results of the parameter dependence study confirm the importance of the length scales and nondimensional parameters identified in the idealized models of flow separation

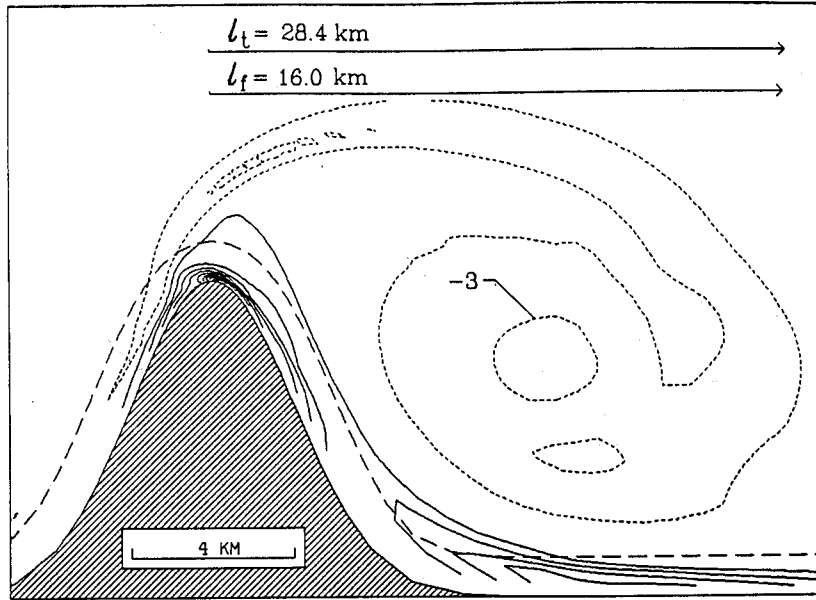


Figure 4-22: Vorticity at slack water for Case 15, which has four times the tidal excursion and four times the frictional decay scale of Case 1.

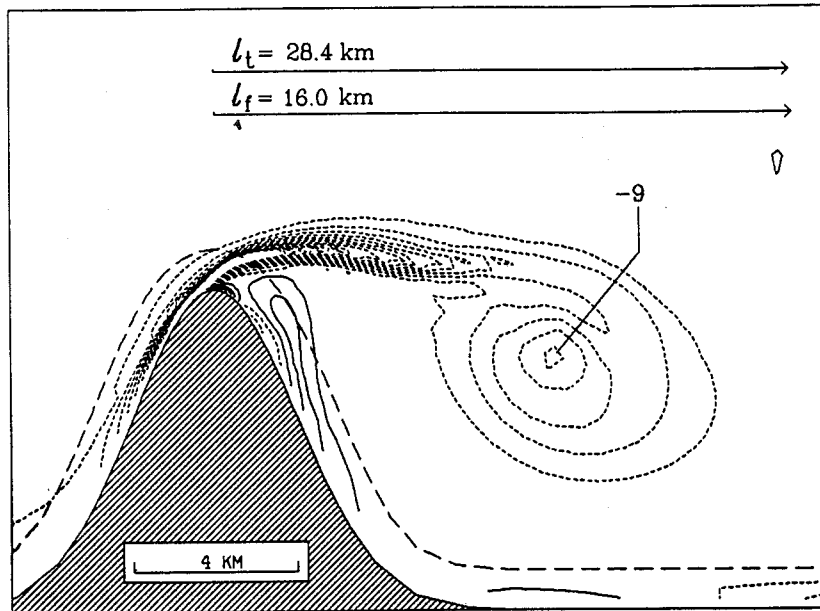


Figure 4-23: Vorticity at maximum eastward flow for Case 15, which has four times the tidal excursion and four times the frictional decay scale of Case 1.

and vorticity transport in the interior. In particular, it has been demonstrated that flow separation is sensitive to the aspect ratio, and that for a fixed headland geometry, much of the nature of the vorticity distribution is controlled by the size of the tidal excursion and the frictional length scale relative to the length of the headland. For a fixed aspect ratio, the dependence on these three length scales can also be expressed as a dependence on the two parameters $Re_f = [H/CDa]$ and $K_c = [U_o/\sigma a]$, since Re_f is proportional ℓ_f/a and K_c is proportional to ℓ_t/a . The approximate dependence of the flow structure on these two parameters, based on the numerical simulations, is shown schematically Figure 4-24 for an aspect ratio of 4. There are six basic dynamical regimes, indicated by the numbers on the headlands. The large circles indicate vorticity associated with large-scale start-up eddies, while the chains of small circles indicate vorticity in a free-shear layer or in a chain of small-scale eddies if the shear layer is unstable. The six regimes are described below.

1. The frictional decay scale is considerably shorter than the tidal excursion ($Re_f \ll K_c$), so that quasi-steady conditions exist and Re_f controls the nature of the flow. Re_f is small, indicating that the frictional length scale is much less than the headland length. This means that friction dominates advection, and the flow does not separate.
2. The flow is quasi-steady ($Re_f \ll K_c$), but the frictional length scale is comparable to the headland length scale, which allows the flow to separate. The extent of the vorticity is comparable to the headland length scale, since it is controlled by the frictional length scale.
3. The tidal excursion is much smaller than the frictional length scale ($K_c \ll Re_f$), so K_c controls the nature of the flow. K_c is small, indicating that the tidal excursion is much less than the headland length. This means that time-dependence dominates advection, the flow is weakly nonlinear, and the flow does not separate.
4. The flow is again controlled by K_c , but now the tidal excursion is comparable to the headland length scale. This allows the flow to separate, and a start-up eddy is formed during each half cycle of the tide. Since the friction is weak, successive start-up eddies can interact, and self-interaction of eddy pairs can cause vorticity to extend further than a tidal excursion from the headland.

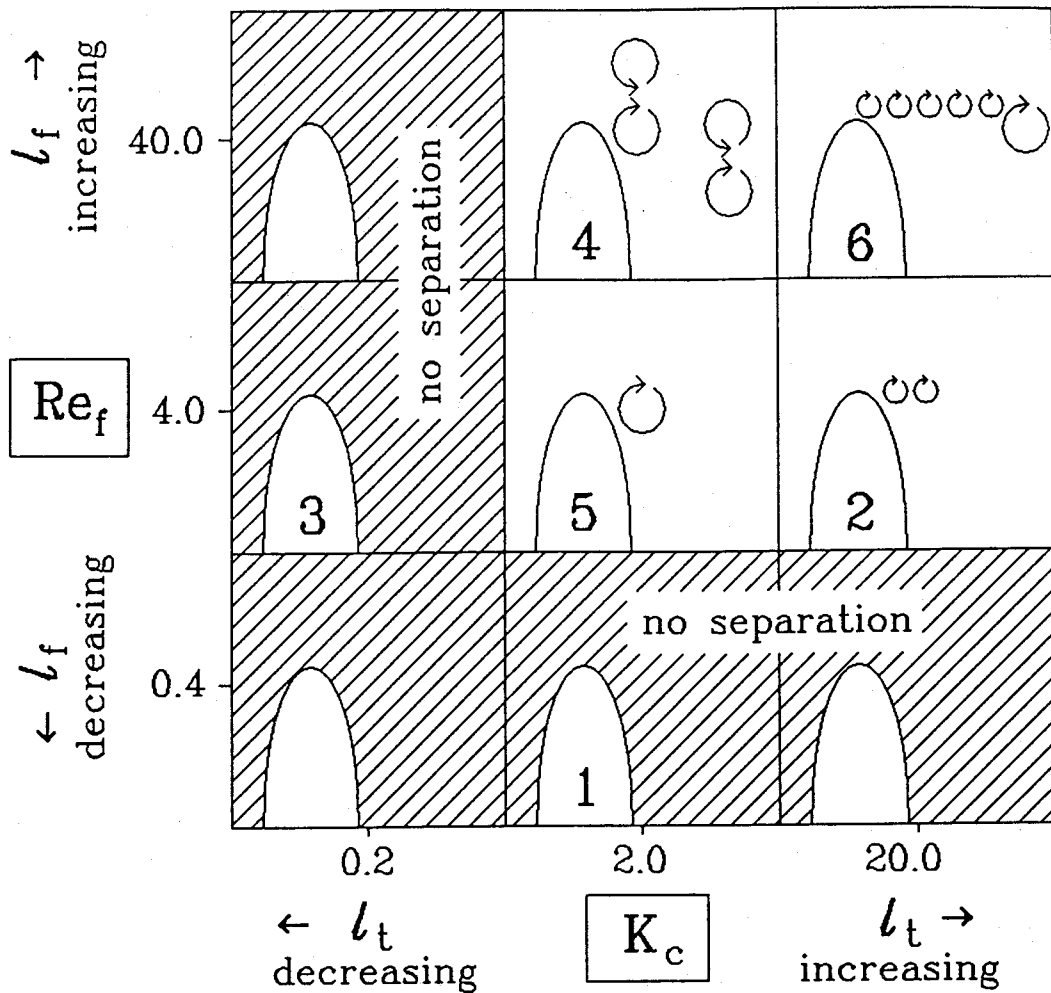


Figure 4-24: Schematic of the tidal structure as a function of $Re_f = [H/C_D a]$, and $K_c = [U_o/\sigma a]$ for aspect ratio 4. There six basic dynamical regimes, indicated by the numbers on the headlands, are described in the text. The large circles indicate vorticity associated with large-scale start-up eddies, while the chains of small circles indicate vorticity in a shear layer or in a chain of small-scale eddies if the shear layer is unstable.

5. The frictional decay scale is comparable to the tidal excursion ($Re_f \approx K_c$), so that while time-dependent effects are important, friction is strong enough so that vorticity decays over the course of a tidal cycle. Both the tidal excursion and the frictional length scale are comparable to the headland length scale, so a start-up eddy forms during each half cycle, but the eddy does not interact with the start-up eddy formed during the subsequent half cycle.
6. The frictional decay scale is again comparable to the tidal excursion, but both scales are considerably larger than the headland length scale. The start-up eddy moves downstream of the headland, leaving a nearly stagnant region in the lee of the headland. The eddy moves more slowly than the free-stream flow due to interaction with its image eddy, so that the vorticity extent is considerably less than the tidal excursion.

These regimes span a broad range of parameter space, covering several orders of magnitude variation in the tidal excursion and frictional length scale. There are many common tidal flows in which time-dependence is important, yet friction is strong enough to strongly damp vorticity over a tidal cycle (Regimes 5 and 6). For M_2 tides of $0.5\text{--}1.5\text{ m s}^{-1}$ magnitude, water depths of $10\text{--}40\text{ m}$ deep, and a drag coefficient of $C_D = 2.5 \times 10^{-3}$, tidal excursions range from $7\text{ to }21\text{ km}$ and frictional length scales range from $2\text{ to }8\text{ km}$. Thus for this common range of tidal flows, vortices do not interact. This fact is used in the section 4.6 to form a simple model describing the strength of the wake.

4.5 Stability of the separated shear layer

One aspect of the vorticity distribution that is not determined by the frictional, tidal and headland length scales is the break-up of the separated shear layer into multiple eddies that was observed in Case 4 (Figure 4-10). It will be shown next that this phenomenon is consistent with wave growth due to instability of the shear layer.

There are some basic characteristics of unstable parallel shear flows that are similar to characteristics of the separated shear layer off the headland. For inviscid parallel flow, Reynolds (1883) showed that an inflection point in the shear profile was a necessary condition for instability. The shear associated with the thin strip of vorticity that is created

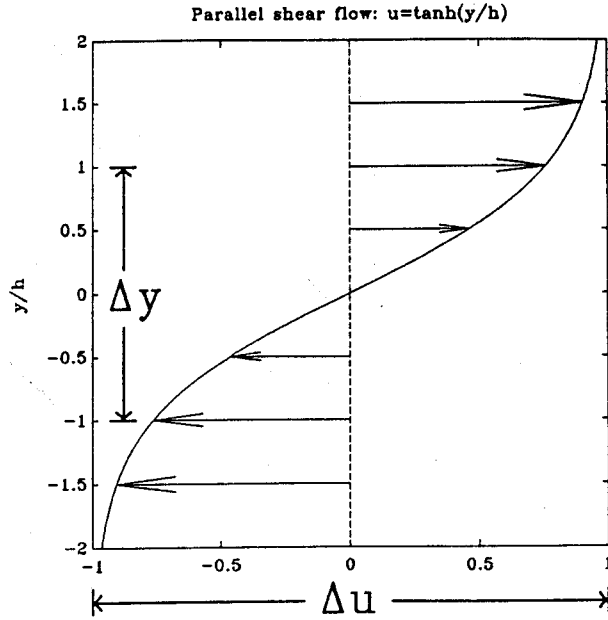


Figure 4-25: Schematic of $u(y) = \tanh(y/h)$ shear layer.

when the boundary layer separates from the headland has such an inflection point. Another basic result is that increasing viscosity can stabilize the layer: in viscous flow, critical Reynolds numbers are defined below which the flow is stable (e.g., Schlichting, 1968). This was confirmed in the headland problem, as when Re was decreased from 1000 (Case 4) to 100 (Case 5), the break-up of the shear layer was not observed.

A rough indication of the spacing between eddies can be obtained by the wavelength of the fastest growing wave based on linear stability analysis. In an inviscid shear layer, the spacing between eddies must depend on the thickness of the shear layer, as this is the only length scale available. Hazel (1972) analyzed the linear stability of a steady inviscid shear profile

$$u(y) = \frac{\Delta u}{2} \tanh\left(\frac{y}{\Delta y/2}\right), \quad (4.25)$$

where Δu and Δy measure the velocity difference and distance across the shear layer (Figure 4-25). The wavelength of the fastest growing mode is approximately $2\pi\Delta y$, which suggests a distance between eddies of about six times the width of the shear layer. In section 4.6, the boundary layer scale is shown to be on the order of 0.5-1.0 km. Since

this determines the width of the shear layer at the point of separation, the fastest growing wavelengths should be 3-6 km. In Case 4, the boundary layer thickness is 0.7 km, which should correspond to a fastest growing wavelength of 4.3 km. The observed spacing between eddies, from Figure 4-10, is about 2.0 km. The comparison is close enough to suggest that the formation of multiple eddies is consistent with instability of the shear layer; the reduced spacing of the eddies in the numerical model may be due to the influence of a more complex velocity structure and frictional and viscous effects.

4.6 Strength of the wake

Another aspect of the tidal flow not explained by the tidal, frictional and headland length scales is the strength of the wake. Here the wake is defined as the region around the headland where significant vorticity levels occur, exclusive of the shoaling region where vorticity is produced. The wake strength is defined as the integrated vorticity, or circulation Γ of the wake. In this section, an idealized model of the wake strength is presented which applies when the frictional length scale is comparable to or less than the tidal excursion so that vorticity produced during successive tidal cycles does not interact. The model is based on the assumption that the vorticity balance is dominated by vorticity flux at the headland tip and frictional damping in the interior.

The circulation of the wake is a useful descriptor of the degree to which the flow departs from purely sinusoidal irrotational flow. Very low values of Γ indicate nearly irrotational conditions, lacking eddies, residual and harmonic current components. There is virtually no mixing or dispersion associated with these flows, as will be shown in section 5.4.2. High values of circulation, on the other hand, indicate the presence of time dependent eddies and strong residual and harmonic current components. Section 5.4.2 shows that horizontal dispersion in these cases can be orders of magnitude greater than the dispersion due to tidal turbulence.

The circulation Γ is the integrated vorticity over the region A bounded by a fixed path S , and can be expressed as

$$\Gamma = \iint \omega dA = \oint_S u_{||} dl, \quad (4.26)$$

where u_{\parallel} is the velocity component parallel to the circuit S , and $d\ell$ is the differential length along S . The equation governing the time rate-of-change of the circulation can be found by integrating the vorticity equation (3.2) over the area A . The result is

$$\frac{d\Gamma}{dt} = \oint_S (f + \omega) u_{\perp} d\ell - \oint_S \frac{C_D |\bar{u}| \bar{u}_{\parallel}}{h + \eta} d\ell - \oint_S A_H \nabla \omega_{\perp} d\ell, \quad (4.27)$$

where u_{\perp} is the velocity component perpendicular to the circuit. The first term on the right hand side represents the net flux of vorticity into the circuit due to advection, the second term represents the total production and dissipation of vorticity in the circuit due to bottom friction, and the third term represents the net diffusive flux of vorticity out of the circuit.

If the circuit S is chosen to bound an area A which includes the entire wake region, but excludes the shoaling region of strong vorticity production near the boundary, then the strength of the circulation in the wake is chiefly determined by the supply of vorticity and frictional damping. A circuit that approximately satisfies these conditions is shown in Figure 4-26, superimposed on the vorticity at the end of eastward flow from Case 10. Diffusive effects are small due to the absence of large vorticity gradients normal to the circuit at the periphery of the defined wake region. Figure 4-27 shows the circulation and the balance of terms in the equation (4.27) for Case 10. At the beginning of the tidal cycle ($t = 0$ hours), there is a flux of negative vorticity into the region A which grows with time, generating a negative circulation. The vorticity flux reaches a maximum at $t = 3$ hours. As damping (dissipation and speed torque) increases in strength, the magnitude of the vorticity flux decreases, resulting in a maximum circulation at $t = 5$ hours. After the tide turns at $t = 6$ hours, the vorticity flux changes sign due to the advection of the eddy out of the circuit.

Since the circulation in the wake depends chiefly on the advective flux of vorticity into the circuit and damping in the interior, a simple model involving only these terms can be constructed in order to identify the parameter dependence of the circulation strength. Over each half cycle, the flux of vorticity into the circuit is dominated by the flux of vorticity off the tip of the headland. Diffusion is neglected and the circulation balance is expressed as

$$\frac{d\Gamma}{dt} \approx \int_0^{\delta} (f + \omega) u_{\perp} d\ell - 2 \frac{C_D |\bar{u}|}{H} \Gamma, \quad (4.28)$$

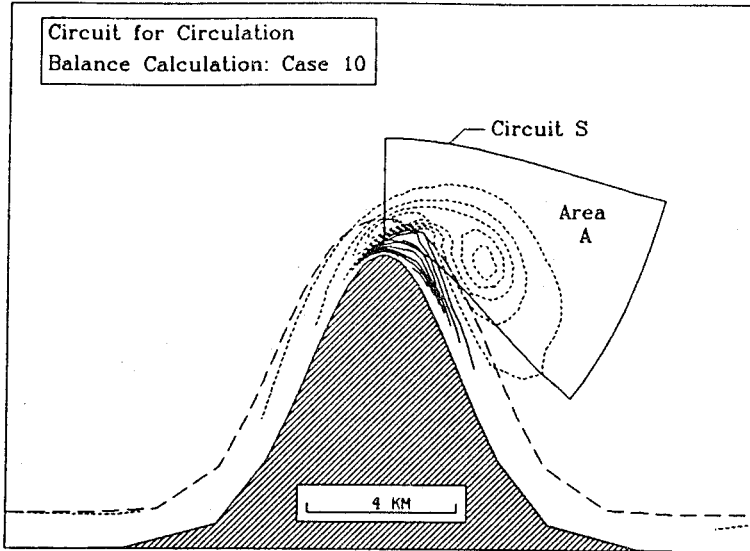


Figure 4-26: Circuit for circulation balance calculation. The fixed circuit S bounds most of the negative vorticity that was injected at the point of flow separation. The vorticity flux from the tip of the headland drives a circulation around S whose magnitude depends on the frictional dissipation over the area A .

where δ is the offshore extent of vorticity production at the tip of the headland, and the dissipation term has been multiplied by 2 to parameterize speed torque effects and modified so that \bar{u} represents the mean speed over the wake region. If \bar{u} is approximated by the far-field flow strength, then the circulation in the interior can be estimated if the vorticity flux at the headland tip is known.

If boundary layer theory applies to the headland (if the radius of curvature of the headland is much larger than the boundary layer thickness), the advective flux can be easily expressed in terms of the far-field flow. The first step is to use boundary layer scaling to approximate the vorticity in the boundary layer by

$$\omega \approx -\frac{\partial u_1}{\partial x_2}. \quad (4.29)$$

For $\omega \gg f$, then, the integrated vorticity flux across the boundary layer has a particularly simple form:

$$\int_0^\delta (f + \omega) u_\perp dl \approx -\int_0^\delta u_1 \left(\frac{\partial u_1}{\partial x_2} \right) dx_2 = -\frac{1}{2} u_1^2 \Big|_{x_2=\delta}. \quad (4.30)$$

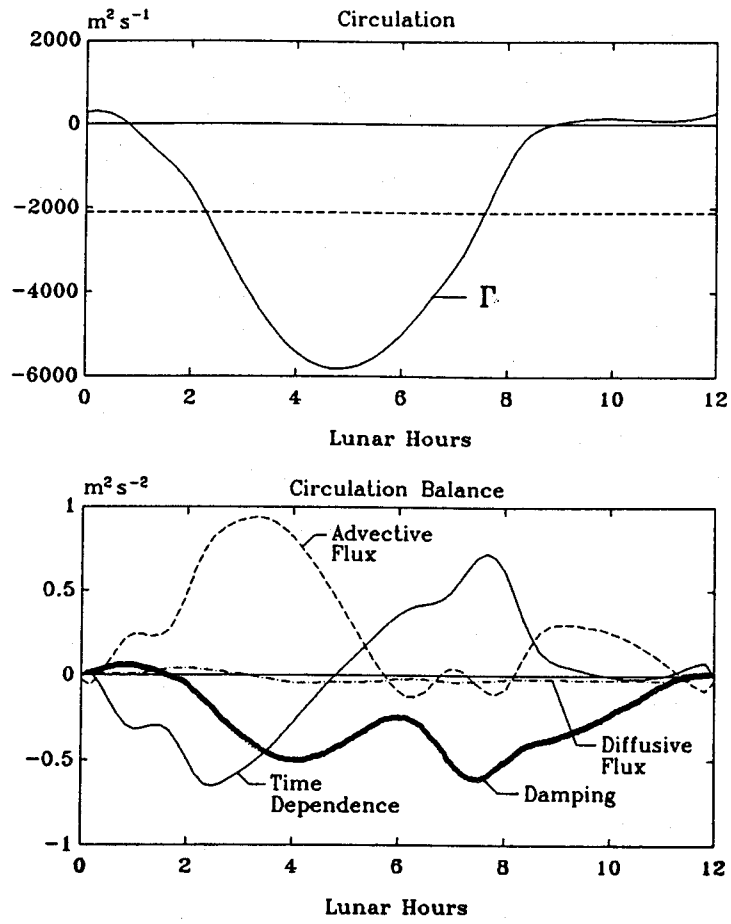


Figure 4-27: Circulation and circulation balance for Case 10.

Thus the integrated flux does not depend on the thickness of the boundary layer, but only on the velocity at the edge of the layer. From the potential flow solution for the elliptic cylinder, (4.7) this velocity is given by

$$u_{x_2=\delta} = U_{tip} = U_o(1 + \alpha), \quad (4.31)$$

where U_o is the far-field flow strength and α is the aspect ratio of the headland. The total vorticity flux from the tip of the headland is thus

$$\text{Vorticity flux} = -\frac{U_o^2(1 + \alpha)^2}{2}. \quad (4.32)$$

Determining the velocity at the edge of the boundary layer by evaluating the potential flow solution at the wall identifies important parameters in the problem, but does not yield reasonable estimates of the vorticity flux when the headland is sharp enough that the potential flow solution varies strongly over the thickness of the boundary layer. For example, if (4.32) is used to estimate the vorticity flux for Case 1, in which $\alpha = 4$, the velocity obtained from the potential flow solution is twice as large as the value obtained in the full numerical model. Figure 4-28 shows the vorticity flux obtained from the numerical model for Case 1 at different distances offshore. The peak flux occurs close to the peak tidal strength, as assumed, but significant flux occurs as far as 800 m offshore. The potential flow solution varies rapidly over this distance (Figure 4-2), so that the magnitude of the potential flow at the coast is not a good estimate of the flow at the edge of the region of vorticity flux. From the full numerical model results, however, it was determined that the velocity at the edge of the boundary layer $u_2|_{x_2=\delta}$ corresponds quite closely to the value obtained from the potential flow solution evaluated at the same point. It was also observed that although the flux is proportional to the square of this velocity, it is roughly twice the value predicted by (4.30). This merely reflects that the boundary layer approximation used in (4.30) is not strictly applicable, and that the curvature of the streamlines make a significant contribution to the vorticity at the tip.

Comparison of the flux obtained in the full numerical model suggest that a reasonable estimate of the vorticity flux can be obtained by evaluating the potential flow solution at the edge of the boundary layer instead of at the boundary. Evaluating the velocity of the potential flow at some distance δ from the coast leads to an interesting and important result.

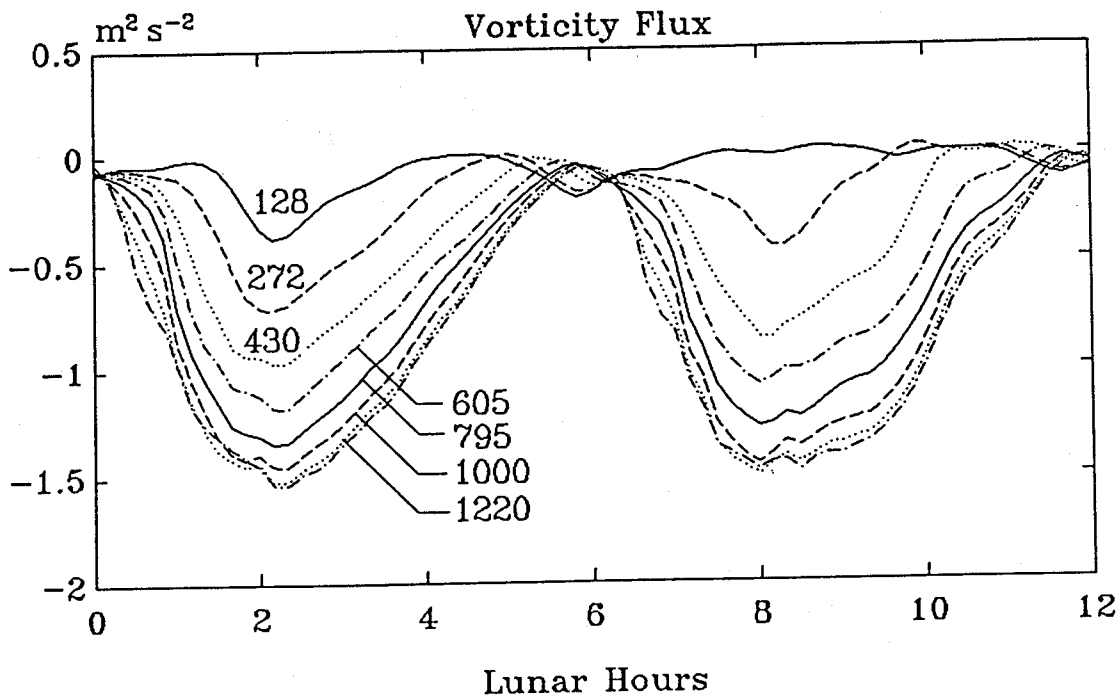


Figure 4-28: Vorticity flux off headland tip for Case 1 at different distances (m) offshore. The total vorticity flux shoreward of the first 8 grid points is plotted as a function of time. The peak vorticity flux occurs near the time of maximum far-field flow and reaches a magnitude of $1.5 \text{ m}^2 \text{ s}^{-1}$. 90% of the flux occurs within 800 m of shore.

If δ is normalized by the headland width b , then in the limit $\delta/b \gg 1/(2\alpha^2)$, and $\alpha \gg 1$, the velocity at δ is

$$u_1(\delta) \approx U_o F_1(\delta/b), \quad (4.33)$$

$$F_1(\delta/b) = \frac{1 + \delta/b}{\sqrt{2\delta/b + (\delta/b)^2}}. \quad (4.34)$$

The approximate expression (4.33) is compared to the exact potential flow solution in Figure 4-29. The top panel shows that as δ/b approaches zero, the velocity is strongly dependent on the aspect ratio, but at a distance δ/b of only 0.1, headlands with aspect ratios of 2, 4 and 8 have nearly the same velocity. The lower panel shows how for a given distance offshore, the flow speed depends primarily on δ/b as α increases. At a short distance offshore, therefore, the potential flow solution ceases to be a function of the aspect ratio α , and is simply a function of the boundary layer thickness δ divided by the width of the headland b . The distance offshore at which this approximation is reasonable becomes shorter for increasing aspect ratio. This means that increasing the aspect ratio beyond the point where (4.33) is valid has virtually no effect on the vorticity flux. This is consistent with the results of the parameter dependence study in which it was found that increasing the aspect ratio from 4 to 8 did not appreciably change the magnitude of the vorticity blob associated with the start-up eddy.

Using the result of the numerical model that the vorticity flux is directly proportional to the velocity squared at the edge of the boundary layer, the expression for the vorticity flux becomes

$$\text{Vorticity flux} = -U_o^2 \sin^2 \sigma t F_1^2(\delta/b) = -U_o^2 \sin^2 \sigma t \left[1 + \frac{1}{2\delta/b + (\delta/b)^2} \right], \quad (4.35)$$

which indicates that the vorticity flux depends primarily on the thickness of the boundary layer relative to the headland amplitude. This shows that that as the boundary layer thickness decreases, the vorticity flux increases due to the increasing potential flow effect.

The circulation balance (4.28), with the advective flux specified by (4.35) becomes

$$\frac{d\Gamma}{dt} = -U_o^2 F_1^2(\delta/b) + \frac{2C_D U_o \Gamma}{H}, \quad (4.36)$$

where the mean speed in the wake has been parameterized by U_o .

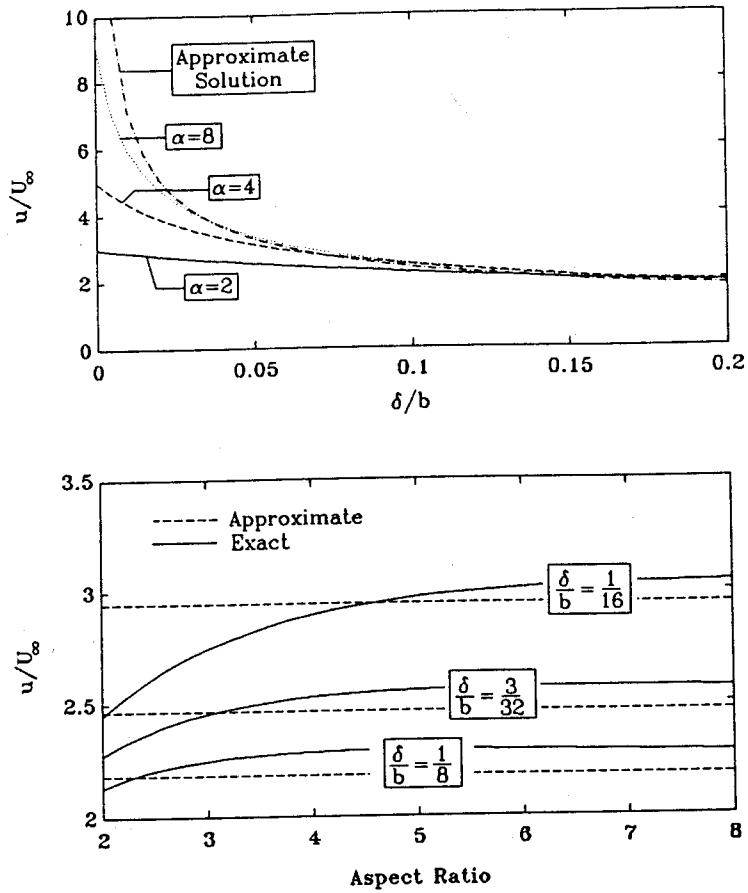


Figure 4-29: Irrotational flow velocity at distance δ off the headland tip. The upper panel shows the nondimensional velocity calculated from the potential flow solution for an elliptic cylinder as a function of δ/b for three different aspect ratios. The upper curve is the approximate solution valid when $\delta/b \gg 1/2\alpha^2$. The lower panel shows the velocity as a function of aspect ratio for three different distances from the tip. The dashed lines indicate the approximate solutions that are independent of aspect ratio.

For a far-field flow given by $U_o \sin \sigma t$, (4.36) becomes

$$\frac{d\Gamma}{dt} = -U_o^2 F_1^2(\delta/b) \sin^2 \sigma t + \frac{2C_D U_o \Gamma}{H} \sin \sigma t; \quad 0 < \sigma t < \pi. \quad (4.37)$$

This equation can be nondimensionalized by letting

$$t = \frac{1}{\sigma} t', \quad \Gamma = \frac{U_o^2}{\sigma} \Gamma', \quad (4.38)$$

which yields

$$\frac{d\Gamma'}{dt'} = \sin t' \left\{ (-\sin t') F_1^2(\delta/b) + 2 \left[\frac{C_D U_o}{\sigma H} \right] \Gamma' \right\}. \quad (4.39)$$

Thus the strength of the nondimensional circulation $[\Gamma \sigma / U_o^2]$ depends on the ratio of the boundary layer thickness δ to the headland width b , which controls the vorticity flux, and the ratio of the tidal excursion $[2U_o/\sigma]$ to the frictional decay scale $[H/2C_D]$, which determines the damping.

The boundary layer thickness δ cannot be quantitatively determined *a priori*, but from (4.21) and (4.22), the thickness should scale with $[C_D U_o / \sigma H] W$ and $[C_D a / H] W$, where W is the width of the shoaling region. Therefore increasing the tidal excursion $[2U_o/\sigma]$ relative to the frictional decay scale $[H/2C_D]$ thickens the boundary layer, and increasing the width of the frictional sloping bottom region also thickens the boundary layer. This dependence was confirmed in the model runs, as δ was determined for the numerical simulations using the distance from the headland which bounded 90% of the peak vorticity flux. These estimates of δ are shown in (Table 4.4).

4.6.1 Comparison of the idealized wake strength model to numerical simulation results

The idealized flux/damping model of the wake strength represented by (4.36) compares favorably to the observed wake strength in the full numerical model when δ is obtained from the numerical model. The circulation balance for Case 10 using (4.37) is shown in Figure 4-30. The general features compare quite well with Figure 4-27. A maximum vorticity flux is about $1.5 \text{ m}^2 \text{ s}^{-2}$, and the maximum circulation occurs at 5 hours with a magnitude of $8000 \text{ m}^2 \text{ s}^{-1}$ (20% higher than the full model). The circulation is not quite

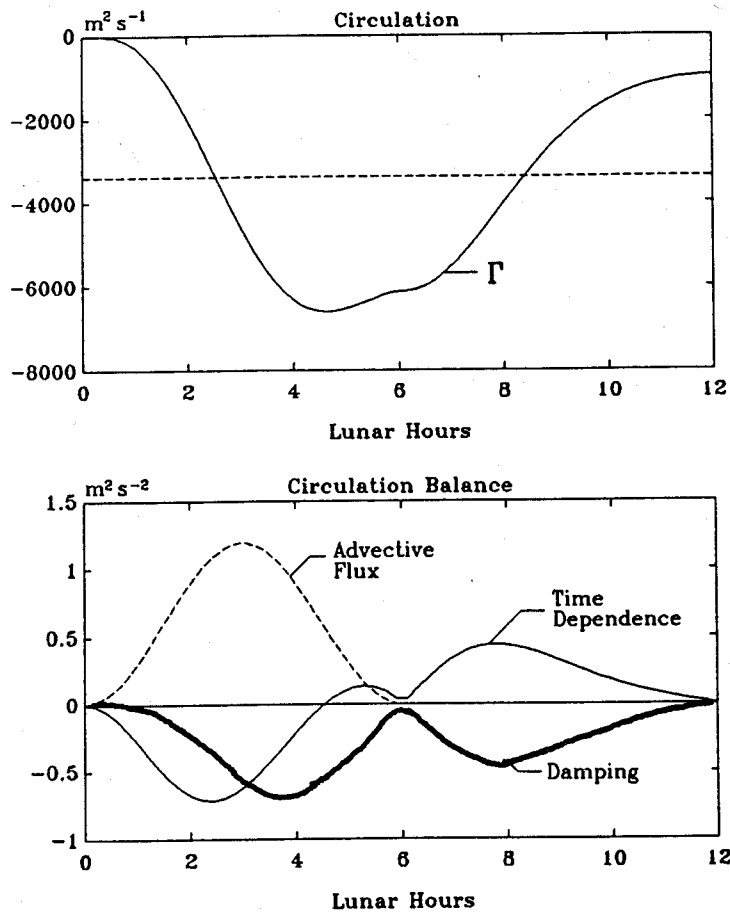


Figure 4-30: Circulation balance for Case 10 from idealized flux/damping model.

Case	a	b	ℓ_t	ℓ_f	α	K_c/Re_f	δ	F_{max}	F_{max}^{fd}	Γ_{max}	Γ_{max}^{fd}
1	2	8	7.1	4.0	4	0.44	0.8	1.5	1.4	7.0	8.0
2	2	8	7.1	2.0	4	0.89	1.0	1.3	1.2	3.4	4.2
4	2	8	7.1	8.0	4	0.22	0.7	2.0	1.6	1.1	1.2
7	4	8	7.1	4.0	2	0.44	1.2	1.0	1.0	2.1	5.7
8	1	8	7.1	4.0	8	0.44	0.7	2.0	1.6	8.5	9.0
12	2	8	14.2	4.0	4	0.88	1.0	1.0	1.2	8.2	8.3
13	2	8	3.5	4.0	4	0.22	0.6	2.5	1.9	4.2	7.0

Table 4.4: Boundary layer thickness δ , maximum vorticity flux F and maximum wake strength Γ from the full numerical model, together with results of an idealized model of the wake in which advective vorticity flux balances bottom frictional damping. F_{max} and Γ_{max} are the maximum vorticity flux and circulation from the numerical model. F_{max}^{fd} and Γ_{max}^{fd} is the maximum vorticity flux from the idealized flux/damping model. The units for a , b , ℓ_t , ℓ_f and δ are km. The units for F are m^2s^{-2} , and the units for Γ are $(\times 10^3 m^2s^{-1})$.

periodic, due to the neglect of advective flux out of the region during the second half cycle and the crude representation of frictional damping.

The parameter dependence suggested by the simple flux/damping model (4.37) is largely confirmed by the full numerical model results. Table 4.4 and Figure 4-31 compare the peak flux F_{max} and circulation Γ_{max} obtained from the full numerical model with F_{max}^{fd} and Γ_{max}^{fd} from the flux/damping model. The values of δ used in the flux/damping model were obtained from analysis of the full numerical model.

Cases 2 and 4 show the effect of changing the frictional scale relative to fixed tidal excursion and headland scales. Changing the frictional scale changes the boundary layer thickness and the peak advective flux, as well as changing the parameter K_c/Re_f (the ratio of the tidal excursion to the frictional scale) which determines the level of damping. In Case 2, the strong friction case, the frictional length scale decreases, creating a thicker boundary layer and diminishing the peak vorticity flux by 13% relative to Case 1. The peak circulation, however, decreases by 51% due to increased damping in the wake. In Case 3, the decreased friction causes a thinner boundary layer, a 33% larger peak vorticity flux, and less damping, leading to a 57% increase in the peak circulation relative to Case 1.

Cases 7 and 8 show the effect of changing the headland scale a relative to the fixed tidal excursion and frictional scales. Changing a , therefore, does not effect K_c/Re_f . In

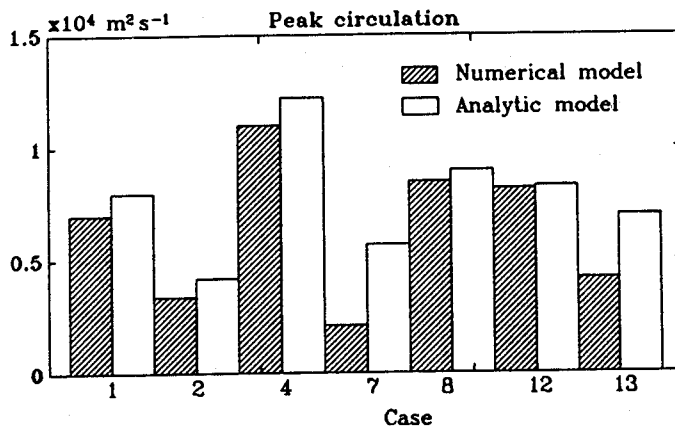
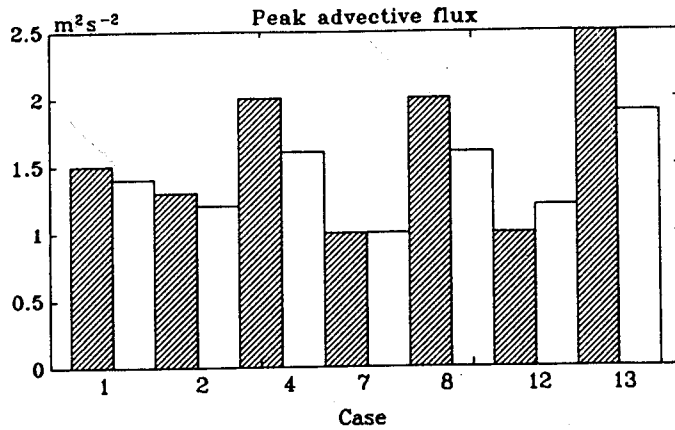


Figure 4-31: Comparison of peak vorticity flux and circulation between the full numerical model and the flux/damping model. The shaded bars indicate the numerical model and the open bars indicate the flux/damping model.

Case 7, the smooth headland case, the boundary layer is thicker and the peak vorticity flux is reduced by 33% compared to Case 1. The peak circulation observed in the numerical model, however, is reduced by 70%, even though the frictional and tidal excursion scales are the same as in Case 1. This is because Case 7 does not separate, and the vorticity flux at the headland tip remains largely in the boundary layer/sloping bottom region. The flux/damping model, which assumes that the flow separates so that the vorticity flux at the headland tip reaches the interior, predicts a circulation that is nearly 3 times too large. Case 8, with a sharper headland than Case 1, has a 33% larger peak vorticity flux and a 21% larger peak circulation. The increases are comparable since in both Case 1 and Case 8, the flow separates for most of the tidal cycle, and thus the greater vorticity flux leads to proportionally greater circulation, since the frictional scale and tidal excursion are the same in both cases (K_c/Re_f is the same).

Cases 12 and 13 show the effect of changing the tidal excursion relative to the fixed frictional and headland scales. This changes the boundary layer thickness, the advective flux, and the damping parameter K_c/Re_f . Case 12, with a frequency half that of Case 1, has a thicker boundary layer, a 33% smaller peak vorticity flux, and an increased damping parameter K_c/Re_f . The peak circulation is 17% higher than Case 1, due to the fact that the flux persists for twice the duration. The peak nondimensional circulation ($\Gamma_{max}\sigma/U_o^2$), which takes into account the lower frequency of forcing, is 41% lower than Case 1, due to the decreased advective flux and the increased value of K_c/Re_f . Case 13, with a frequency twice that of Case 1, has a thinner boundary layer, a 68% larger peak vorticity flux, and a smaller damping parameter K_c/Re_f . Since the duration of the flux is only half as long, the flux/damping model predicts the same dimensional circulation as observed in Case 1. The peak dimensional circulation from the numerical model shows a 40% reduction, but this is attributable to the short tidal excursion (3.5 km) which limits much of the vorticity to remain over the sloping bottom which is excluded from the calculation. The nondimensional peak circulation, taking into consideration the difference in frequencies, is 100% greater than Case 1, owing to the larger vorticity flux and the decreased value of K_c/Re_f .

The results in this section have shown that when friction is strong enough to damp vorticity over a tidal cycle, the strength of the wake, as measured by the circulation is

determined by three factors.

1. Vorticity flux. Vorticity flux depends on the square of the far-field velocity, and on the ratio of the boundary layer thickness δ to the offshore extent b of the headland. The boundary layer thickness, from (4.21) and (4.22), depends on the frictional decay scale, the tidal excursion, the headland length scale, the width of the shoaling region, and the aspect ratio. (gook) Increasing the frictional length scale and the aspect ratio decreases δ , which increases the vorticity flux. Increasing the tidal excursion and the width of the shoaling region increases δ , which decreases the vorticity flux.
2. Boundary layer separation. If the boundary layer does not separate, vorticity remains primarily in the shoaling region along the coast, and a wake in the interior does not develop. Flow separation is a strong function of the headland aspect ratio, and for fixed geometry depends on K_c and Re_f .
3. Damping. Damping due to bottom friction limits the circulation driven by the vorticity flux, and is determined by K_c/Re_f . The parameter K_c/Re_f represents the ratio of the tidal excursion relative to the frictional decay scale, with increasing values corresponding to stronger damping and weaker circulation.

4.7 Results from viscous flow around bluff bodies

Wakes around islands in shallow water have been compared to laboratory studies of two dimensional viscous flow around bluff bodies (Wolanski et al., 1984). In this section, additional insight into the nature of the wake is obtained by comparing and contrasting the tidal headland flow to 2-D viscous flow around bluff bodies. Many of the important aspects of these problems, flow separation, vorticity transport, eddy formation, and stability of the free shear layer, are similar. The principal difference is the importance of bottom friction in the shallow tidal flow.

The study of 2-D viscous flow around bluff bodies has an extensive literature and is similar in many ways to the problem of tidal flow around headlands. This area of research concerns the flow around bodies of infinite extent in one dimension, but with fairly abrupt

geometry in the plane normal to this dimension (i.e. not streamlined). The resulting flow is strictly two-dimensional, and can be interpreted as the result of vorticity production, advection and diffusion. In the interior of the fluid, vorticity is transported by advection and diffusion but cannot be produced or destroyed. Vorticity is only produced along the boundary of the body where the flow satisfies the no-slip condition. The behavior of steady, impulsive, and oscillatory flow past a variety of geometrical objects and flow conditions has been investigated, and the principal results are summarized in sections 4.7.1–4.7.3. The relevance of these findings to the tidal headland flow is then discussed in section 4.7.4.

4.7.1 Steady flow

In steady viscous flow, the behavior of the flow past the body is determined by the Reynolds number $Re = [UL/\nu]$, which expresses the ratio of advection to viscosity. In this expression U is a characteristic velocity scale usually chosen as the imposed magnitude of the far-field flow, L is a characteristic length scale of the obstacle, and ν is the kinematic viscosity of the fluid. For steady flow around a body of a given geometry, Re is the only available parameter that appears when the governing equations are nondimensionalized, and therefore completely describes the flow. The progressively changing nature of the flow field for $Re = 1$ –500,000 is described below for flow around a circular cylinder based on the review paper by Gerrard (1978). This range brackets the range of expected values of Reynolds number for the tidal headland, since a Reynolds number based on the headland length, horizontal eddy viscosity, and the current amplitude ($Re \equiv [U_o a/A_H]$), yields $Re = 500$ –60,000 for flow amplitudes of 0.5–1.5 m s⁻¹, headland lengths of 1–4 km, and an eddy viscosity of 0.1–1 m² s⁻¹. The frictional Reynolds number $[H/C_D a]$, however, is order 1–10 m² s⁻¹.

When $Re \ll 1$, diffusion dominates advection to such a degree that the vorticity generated at the boundary diffuses outward as if the flow were stationary. If the body is symmetrical about the axis perpendicular to the far-field flow, then the corresponding flow field is also symmetrical. No adverse pressure gradients exist and no flow separation occurs. This is similar to the case with strong frictional damping where $Re_f \ll 1$ (Case 3), which revealed the vorticity field to be symmetrical under strong frictional damping. In both cases, the advection of vorticity is dominated by friction and asymmetry cannot develop.

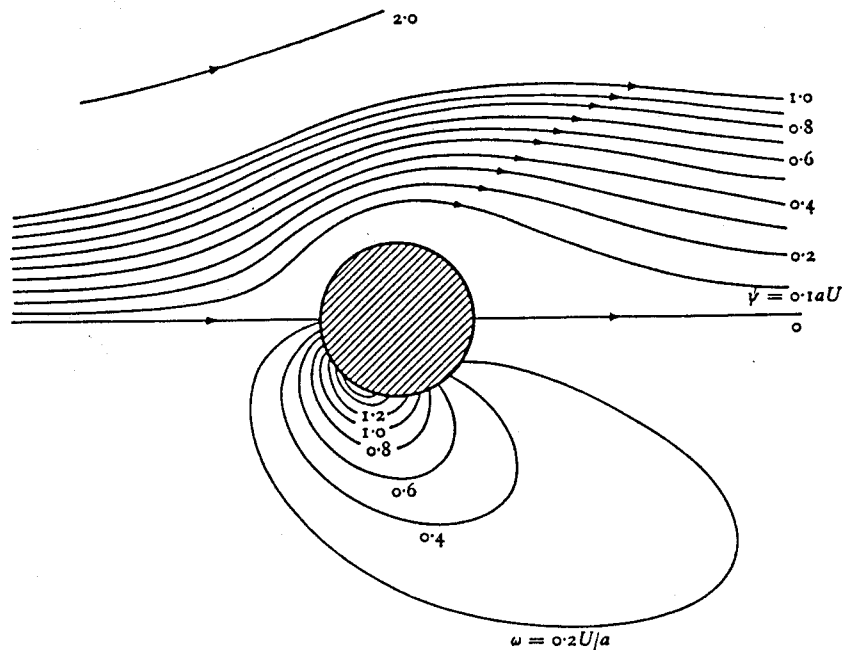


Figure 4-32: Streamlines (upper half plane) and vorticity contours (lower half plane) for flow past a cylinder at Reynolds number $Re = 4$. Calculations by Keller and Takami (1966), figure from Batchelor (1967).

As $Re > 1$, advection begins to play a role in the steady vorticity distribution. As vorticity diffuses away from the boundary it is also advected downstream, and an asymmetric flow field results. Figure 4-32 shows the streamlines and vorticity distribution for flow around a cylinder at $Re = 4$. Diffusion is large enough so that the vorticity on the leading face extends outward over a distance comparable to the diameter of the cylinder. Advection is clearly apparent by the tongue of vorticity extending downstream, and the asymmetry of the flow is evident in the greater separation between streamlines on the trailing side of the cylinder.

Once Re reaches about 5, the advective influence on the pressure gradient is strong enough so that the flow separates near the rear stagnation point of the cylinder. The streamlines that leave the boundary at the point of separation merge downstream, enclosing a weak recirculating region in which flow speeds are a few percent of the far-field value. As

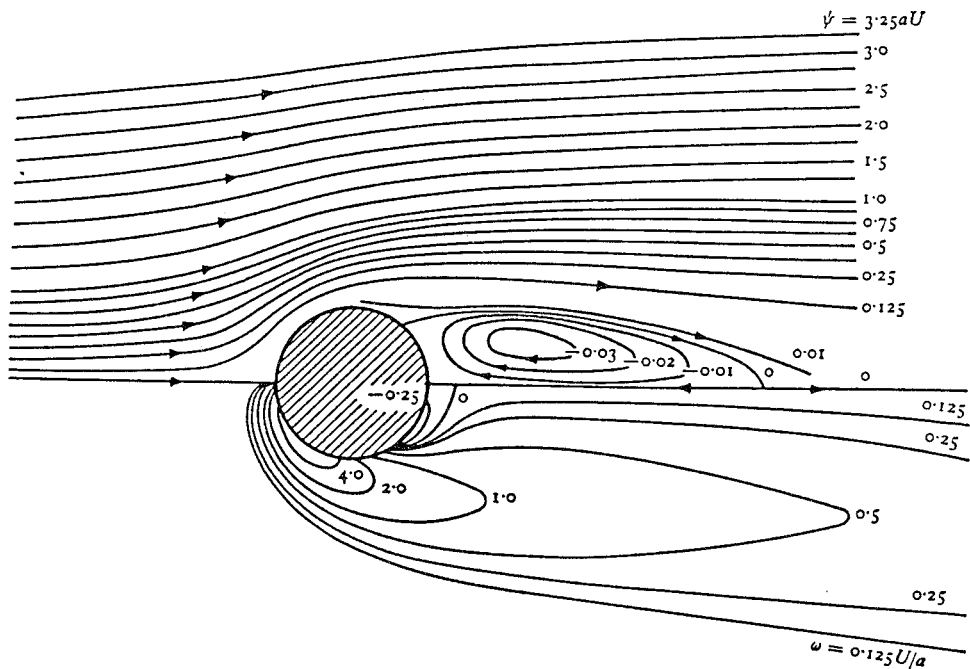


Figure 4-33: Streamlines (upper half plane) and vorticity contours (lower half plane) for flow past a cylinder at Reynolds number $Re = 40$. Calculations by Apelt (1961), figure from Batchelor (1967).

Re increases further, the region of backflow increases, the point of separation moves back along the cylinder, and the recirculating region grows in downstream extent. Figure 4-33 shows the streamlines and vorticity distribution around a cylinder at $Re = 40$. Flow separation occurs at approximately 130° , and the standing eddy extends two diameters downstream. From the streamfunction contours, it can be seen that the flow in the eddy has a magnitude about 10% of the far-field flow. Note also that the thickness of the vorticity layer on the leading face has decreased considerably compared to $Re = 4$.

At about $Re = 50$, the wake downstream of the standing eddies develops time dependent fluctuations, which gradually work their way back toward the cylinder as Re increases. At $Re = 70$, the standing eddies begin to oscillate back and forth and periodically shed eddies of alternate sign forming the well-known "Karman vortex street". The formation of the Karman vortex street depends critically on the interaction of the vorticity produced

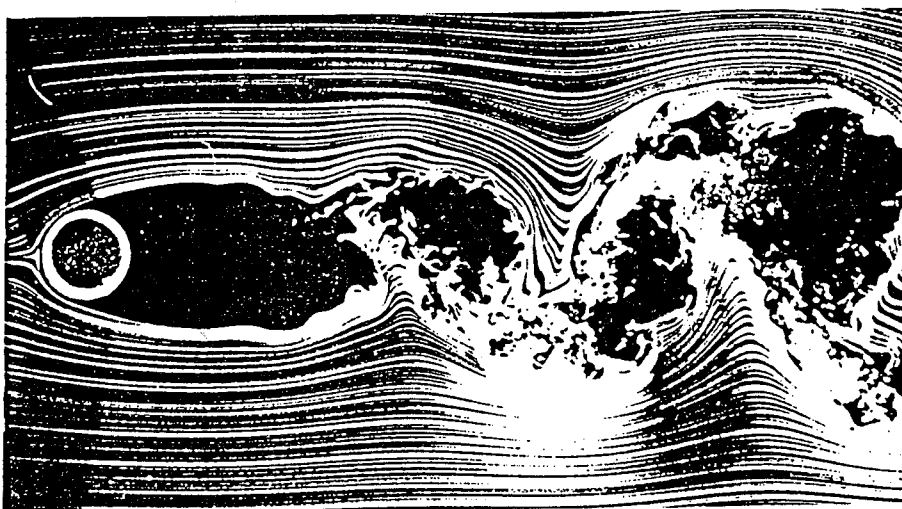


Figure 4-34: Streakline for flow past a cylinder at Reynolds number $Re = 10,000$. Photographed by Thomas Corke and Hassan Nagib. Reproduced from Van Dyke (1982).

on opposite sides of the cylinder. If a splitter plate is inserted downstream, the street disappears. This is analogous to the tidal headland case, in which vorticity of a single sign only is generated during a given half cycle.

For Re above about 100, advection of vorticity on the leading face of the cylinder dominates diffusion to such a degree that the thickness of the vorticity layer is much less than the cylinder radius. Boundary layer theory then may be used to predict the point of separation and the structure of the flow upstream of this point.

At Re above 350, waves appear on the shear layers emanating from the point of flow separation which grow downstream (Gerrard, 1978). These oscillations cause the wake many lengths downstream of the cylinder becomes turbulent. For Re around 2000, these waves roll up to form small scale vortices.

Above about $Re = 2000$, a plateau is reached where the the solution does not appreciably change until the boundary layer becomes turbulent at about $Re = 500,000$. Figure 4-34 illustrates this regime for flow around a cylinder at $Re = 10,000$. The boundary layer is laminar over the front of the cylinder, separates, and breaks up several cylinder diameters downstream into a turbulent wake. Flow separation has reached its upstream limit, at

about 80° . The fact that the flow separates upstream of 90° illustrates the effect of the flow separation on the upstream pressure distribution. While the potential flow predicts a minimum pressure at 90° , actual measurements reveal that the minimum pressure occurs at about 70° , about 10° upstream of the point of flow separation.

In summary, asymmetry in steady flow around a symmetrical body occurs when the advection of vorticity is a significant term in the vorticity balance. Above a critical Reynolds number, the flow separates and the separation streamlines bounds a region of weak circulation that extends several body length scales downstream. The flow speeds in the recirculation zone are only a few percent of the free-stream flow speed. Strong eddies are formed by two mechanisms. The first is due to an instability which causes the wake to oscillate back and forth, shedding large scale eddies of alternate sign which form a Karman vortex street. This mechanism disappears when vorticity of only one sign is formed. The second mechanism is due to instability of the free-shear layers that emanate from the points of flow separation, forming small-scale eddies of the same sign as the vorticity rolls up into concentrated lumps.

4.7.2 Adjustment to impulsive start-up

In steady 2-D viscous flow at large Re , vorticity produced at the body affects the flow field many body lengths downstream. This suggests that a time scale of several times L/U is required for the flow to reach steady state. As we are interested in oscillatory flow, a important issue is the start-up process in flow around bluff bodies – how the boundary layer vorticity behaves after separation first occurs, and how flow adjusts to reach steady state.

Many experiments have been performed by other investigators to study the adjustment of impulsively accelerated flow, in which the flow is suddenly brought to a constant velocity from an initial state of rest. Figure 4-35 shows a sequence of snapshots of the start-up process for impulsively accelerated flow around a wedge. Immediately after the start of motion, vorticity leaves the boundary layer in a free-shear layer at the point of flow separation. The snapshots show the roll-up of the layer as it advects downstream. The reason for this roll-up can be understood if the vorticity is conceptualized as a vortex sheet consisting of many closely-space point vortices. The vortex at the free end of the sheet experiences an induced

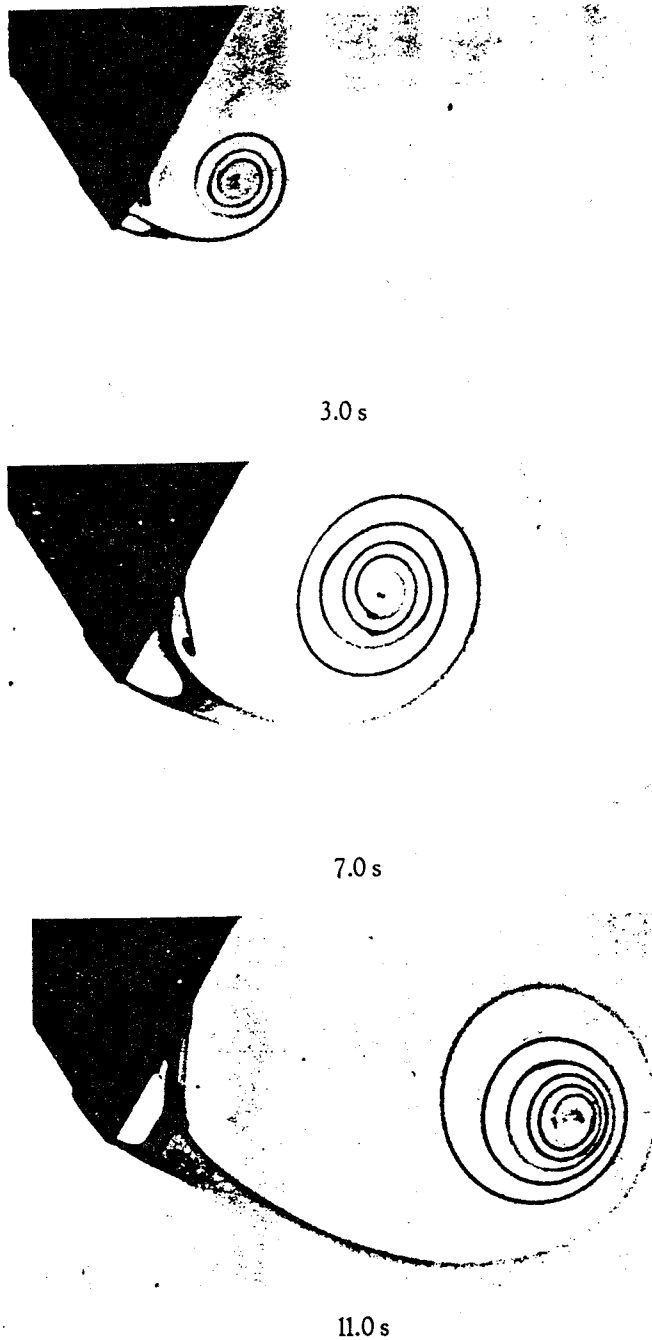
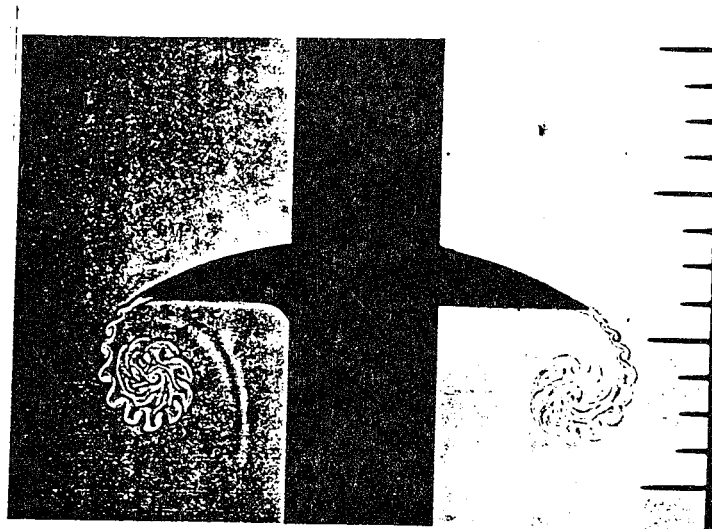


Figure 4-35: Starting vortex on a wedge. Neutrally buoyant dye reveals the wrap-up of the vortex sheet from an impulsively accelerated wedge. From Pullin and Perry (1980). Reproduced from Van Dyke (1982).



$t=6.53 \text{ ms}, v=24.0 \text{ ft/s}$

Figure 4-36: Growth of vortices on an accelerated plate. Spark shadowgraph of the wake formed by a sharp-edged body impulsively accelerated from rest. Small-scale undulations form on the vortex sheet as the large-scale wrap-up takes place. From Pierce (1961).

motion normal to the sheet due to the other vortices (Batchelor, 1967). This motion causes the end of the sheet to curl up, wrapping the rest of the sheet around it. As the sheet wraps up, vorticity is concentrated into a large scale feature known as the start-up vortex. In the third frame, the vortex has advected downstream to the extent that the flow in the immediate vicinity of the wedge is not influenced by its motion. Subsequent pictures of the adjustment process would show the start-up vortex advecting downstream, leaving behind a steady separation streamline bounding a weakly recirculating region behind the wedge.

The small-scale roll-up of separated shear layers is well documented in studies of viscous flow around bluff bodies. An example is shown in Figure 4-36, in which a sharp-edged object is suddenly brought from rest to a constant velocity. As the salient edge moves from its initial location, it leaves a thin sheet of vorticity behind, which exhibits the large scale roll-up described in section 4.7.2. In addition, however, there are small scale roll-ups which form distinct vortices at roughly equal intervals. The small-scale roll-up of vorticity is associated with instability of the shear layer (Pierce, 1961).

4.7.3 Oscillatory flow

Oscillatory flow can be conceptually viewed as an extension of impulsive flow, where a start-up vortex is formed during each half cycle and advects downstream. Since the vorticity at steady state extends many body lengths downstream, the degree to which steady state is achieved during each half cycle depends on the excursion scale of the oscillating flow relative to the body length scale. This ratio is defined by the Keulegan-Carpenter number which for a cylinder is given by $K_c \equiv [U_o T / D]$, where $U_o T$ is an excursion scale, and D is the diameter of the cylinder (Keulegan and Carpenter, 1958). Oscillatory viscous flow is therefore defined by two dimensionless parameters: the Reynolds number, which measures the ratio of advective to viscous effects; and the Keulegan-Carpenter number, which measures the ratio of advective to time-dependent effects.

The nature of oscillatory flow around a circular cylinder for K_c ranging from 0–30 and $Re/K_c = 1685$ has been studied by Graham (1979), who found three basic regimes that describe the flow. For $K_c < 0.3$, the advective term is much smaller than the time-dependent term and flow separation does not develop. For $K_c < 15$, one eddy is generated during each half cycle in a manner analogous to the development of eddies in impulsively accelerated flow. At the beginning of the half cycle, the far-field flow is at rest and the acceleration is at a maximum. Over the first quarter cycle, the flow increases, and the point of flow separation moves upstream from the downstream stagnation point. The vorticity shed from the boundary layer rolls up to form a starting vortex, but before the eddy can advect away from the cylinder the pressure gradient begins to reverse the flow. The presence of the eddy is felt along the boundary, where the velocity reverses well before the free stream, and begins to form a new eddy on the opposite side of the cylinder. When the free-stream flow reverses, the old eddy is swept back around the cylinder. At this point the old eddy may pair with the new eddy and rapidly propagate away from the body (as the result of eddy-eddy interaction), or the new eddy may wrap the old eddy on itself, with cancellation of vorticity. For $K_c > 15$, newly formed eddies interact not only with the previously formed eddies, but with the eddies formed on the opposite side of the cylinder during the same half cycle. In this case, partial Karman vortex streets are formed, which are then swept back on the cylinder during the second half cycle, creating very complicated flow patterns

(Williamson, 1985).

4.7.4 Application to the tidal headland problem

Tidal flow around a headland and 2-D oscillatory flow around a cylinder have the same basic mechanism that produces the strong asymmetry and eddy formation characteristic of these flows: strong advection of vorticity away from a localized production region along the boundary of the body. In both cases, if the advective terms are large enough, the flow separates, forming a free-shear layer, and the vorticity is injected into the interior in a narrow sheet. The sheet then wraps up, forming a large lump of vorticity representing a start-up eddy. If the sheet is unstable, a number of smaller lumps may form. The resulting vorticity distribution (and velocity field) after many cycles depends on the details of how these lumps of vorticity are advected, interact, and are affected by frictional processes.

One difference between 2-D oscillatory flow around a cylinder and tidal headland flow is the formation of the Karman vortex street. For oscillatory flow around the cylinder, opposite signed vortices produced on each side of the cylinder interact downstream to form a Karman vortex street for $K_c > 15$. In the tidal headland case, there is no mechanism to create a Karman vortex street, since there is only one point of flow separation with vorticity produced of a single sign.

The primary difference between the two cases, however, is the influence of bottom friction in tidal flow. In 2-D viscous flow around bluff bodies, vorticity is produced exclusively at the side-wall boundaries of the body as the result of the no-slip condition. Vorticity diffuses as the result of molecular viscosity, and cannot be destroyed in the interior. In tidal flow around a headland, the vorticity is typically produced by bottom torque acting over the sloping sidewalls. Vorticity diffuses as the result of bed-generated tidal turbulence, and vorticity in the interior decays as the result of bottom friction.

Due to the importance of bottom friction, the flow around tidal headlands has a different parameter dependence than viscous flow around bluff bodies. For fixed geometry, both flows depend primarily on the Keulegan-Carpenter number and a type of Reynolds number, but in the case of viscous flow around bluff bodies the Reynolds number expresses the ratio of the viscous decay scale to the body length scale, while for tidal headland flow, the frictional

Reynolds number expresses the ratio of the bottom frictional decay scale to the body length scale.

4.8 Conclusions

This chapter has shown that tidal dynamics around a coastal headland depends strongly on the shape of the headland, represented by the aspect ratio, but that for fixed geometry, much of the nature of the flow depends on the relative sizes of the frictional length scale, the tidal excursion and the length scale of the headland. Taking ratios of these length scales allows the flow to be described in terms of a Keulegan-Carpenter number $K_c = [U_o/\sigma a]$, which expresses the importance of advection relative to time-dependence, and a frictional Reynolds number $Re_f = [H/C_D a]$, which expresses the importance of advection relative to bottom friction. When the frictional decay scale is much less than the tidal excursion, the extent of vorticity advection from the headland is controlled by Re_f , and vorticity produced during subsequent tidal cycles does not interact. When the frictional decay scale is much greater than the tidal excursion, the nature of the vorticity is controlled by K_c , the vorticity produced during subsequent tidal cycles interacts vigorously, and the extent of vorticity from the headland can be greater than the tidal excursion. The model for the strength of the wake, which applies when the frictional length scale is comparable to or shorter than the tidal excursion, shows that the peak circulation is dependent on the vorticity flux at the headland tip and the frictional damping in the interior. For aspect ratios greater than two, the vorticity flux is shown to depend on the square of the far-field velocity, and the thickness of the boundary layer δ relative to the headland width (offshore extent) b . The boundary layer thickness depends on Re_f , K_c/Re_f , the aspect ratio α , and the thickness of the shoaling region W . Higher values of Re_f and α lead to thinner boundary layers and greater vorticity flux, while higher values of W and K_c/Re_f lead to thicker boundary layers and decreased vorticity flux. The frictional damping depends on the ratio of the tidal excursion to the frictional length scale. Decreasing the frictional length scale relative to the tidal excursion reduces the circulation. In Chapter 5 it is demonstrated that the peak circulation gives a good indication of the degree of dispersion that occurs over a tidal cycle due to deformation of the flow.

There are many similarities between oscillatory viscous flow around a cylinder and tidal flow around headlands. In both cases, the vorticity is produced along the boundary of the body: in the viscous case, by the no-slip condition; in the headland flow, by the shallow depths near the coast. Advection of vorticity away from the source region leads to asymmetry in the flow field, which leads to the generation of residual and harmonic current components. The major difference between the viscous bluff body flow and tidal headland flow is that bottom friction is typically more important than viscosity in determining the structure of the vorticity around tidal headlands. Thus for a fixed geometry, viscous bluff body flow around a cylinder of diameter D depends on the Keulegan-Carpenter number $[U_o/D\sigma]$ and the Reynolds number $[U_oD/\nu]$, while flow around a tidal headland with length scale a depends on the Keulegan-Carpenter number $[U_o/\sigma a]$ and the frictional Reynolds number $[H/C_D a]$. The nature of the flow around headlands, of course, also depends on the shape of the headland, specified for Gaussian headlands by the aspect ratio. The dependence on the Keulegan-Carpenter number and the frictional Reynolds number changes with changing aspect ratio.

Chapter 5

Tidal Dispersion

5.1 Introduction

In many shallow estuaries and embayments, tidal dispersion plays an important role in the horizontal transport of pollutants, larvae and other suspended or dissolved material. Zimmerman (1976) found that in the Dutch Wadden Sea, the large effective diffusivities calculated from salinity observations ($100\text{--}1000\text{ m}^2\text{ s}^{-1}$) could be explained by tide-induced dispersion based on an analytic model which considered interactions of a purely oscillatory tidal flow with a spatially varying tide-induced residual eddy field. Awaji et al. (1980) and Awaji (1982) conducted numerical experiments of mixing around a tidally dominated strait and found that even without considering the tide-induced residual effects, the rapid spatial variation in the oscillatory current could give rise to large residual particle displacements and to large dispersion ($800\text{ m}^2\text{ s}^{-1}$) values for material released in the vicinity of the strait.

Insight into dispersion generated in the absence of random motions was obtained by Aref (1984), who showed that a completely deterministic, periodic flow of simple form could give rise to rapid mixing due to chaotic particle trajectories. The efficiency of the mixing was controlled by the strength of a small region of high strain and the frequency with which material interacted with this region of high strain. Building on the work of Aref (1984), Pasmarter (1988) examined particle trajectories in a kinematic tidal flow consisting of a mean and oscillatory current that vary harmonically in space. For some values of the flow parameters, he found that the area of released patches grew linearly with time,

directly analogous to Brownian motion or turbulent diffusion. For other values, however, Pasmanter (1988) found “islands” of unmixed material embedded in the well-mixed regions, and discovered that the area of patches could grow faster or slower than linearly with time, a phenomenon he termed “anomalous diffusion”.

Aref (1984) and Pasmanter (1988) specified kinematic tidal flow fields, studying the nature of mixing over many tidal cycles, and over a range of flow parameters. Awaji et al. (1980) and Awaji (1982) used a numerical model to generate a flow field, and primarily studied the nature of mixing over a single tidal cycle. In this chapter, the technique of Awaji et al. (1980) is used to investigate the tidal dispersion around an idealized headland, but the simulations are extended over multiple tidal cycles to understand better the longer-term mixing behavior. In the first section, the deformational stretching and folding of material following the fluid is described for a tidal flow characterized by flow separation and transient eddy formation. It is shown that in a coarse-grained sense, this represents an effective mixing mechanism in the vicinity of the headland. In the second section, the sensitivity of the dispersion to varying the parameters identified in Chapters 3 and 4 is investigated.

5.2 Stretching and folding: the basic mixing mechanism

The basic mixing mechanism around the headland is illuminated by following the deformation over a tidal cycle of a fixed volume of fluid that travels through the region of high strain near the headland tip. To accomplish this, the outline of a box composed of 480 tagged parcels (particles) was placed upstream of the headland at the start of the tidal cycle (Figure 5-1a) and tracked for 12 lunar hours using the flow field generated in Case 10.

Case 10 was chosen to illustrate the mixing mechanism because the relatively high eddy viscosity ($10 \text{ m}^2 \text{ s}^{-1}$) results in a smoother flow field than the low eddy viscosity cases ($1 \text{ m}^2 \text{ s}^{-1}$). This allows the box to be tracked with fewer particles. The following sequence of snapshots shows the progressive deformation of the box due to the strain field near the headland tip. The corners of the box are marked by the points A, B, C, D.

At the beginning of the cycle, the early reversal of the flow at the headland tip advects point B smoothly around the headland tip, while further away from the headland, the tide

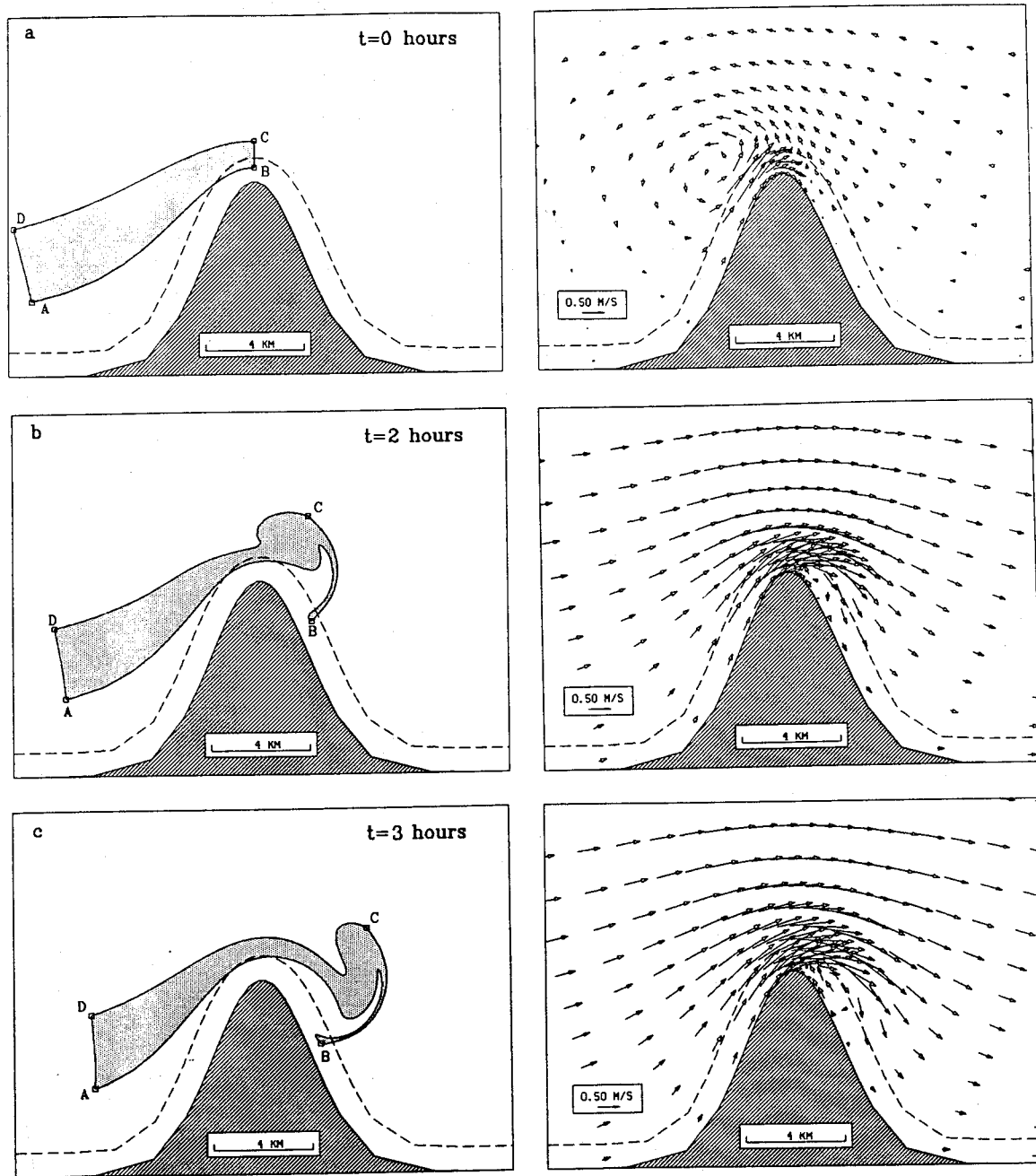


Figure 5-1: Patch deformation over 1 tidal cycle in Case 10. (a) Initial location of 4800 parcels defining the boundary of a four sided patch and the corresponding Eulerian velocity field at 0 lunar hours. (b-f) Patch locations and Eulerian velocity fields at 2,3,6,9 and 12 lunar hours.

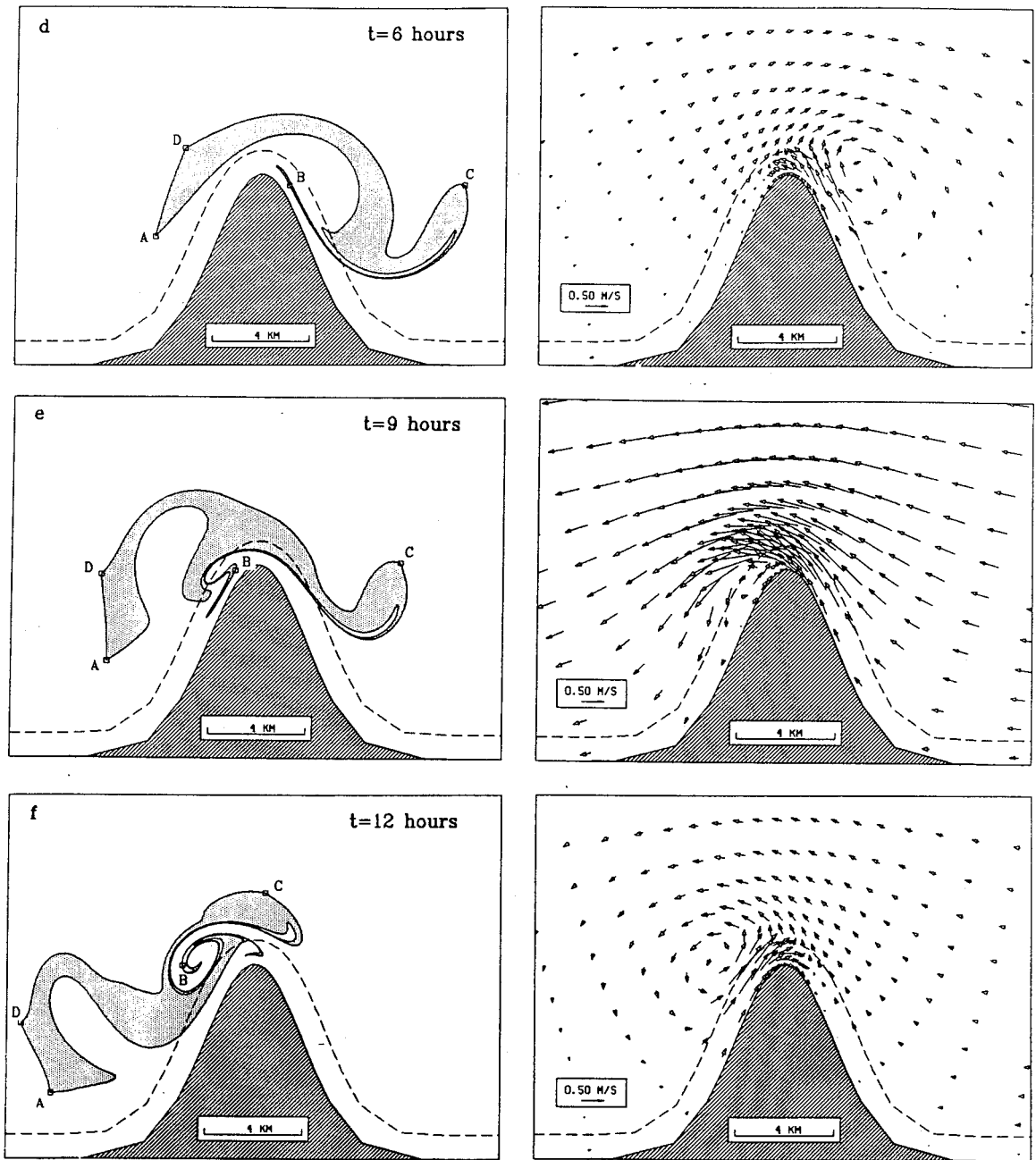


Figure 5-1: Continued.

turns later and is influenced by the counterclockwise eddy formed during the previous half cycle. The result is that the south-east corner of the box is pulled into a long nose of material, while a bulge due to the counterclockwise eddy forms just upstream of the tip (Figure 5-1b). Between 2 and 3 lunar hours, there is strong flow at the headland tip, and the clockwise eddy is beginning to grow at the point of separation (Figure 5-1c). The stronger flow near the headland causes the inshore part of the patch to overtake the offshore part, forming a fold which is clearly seen at 3 lunar hours (Figure 5-1c). The nose meanwhile (with point B), is drawn into the westward return flow of the clockwise eddy, and advects back toward the headland while the rest of the patch is moving eastward. At the end of the half cycle, the shape of the patch is much different than the reflection of the initial patch shape (Figure 5-1d). The effect of the straining near the headland has caused a large fold to form on the eastern side of the patch, as well as a small strand of highly stretched material from the southeast corner of the box. The path length between points B and C has increased from 1 km to 12 km over only 6 lunar hours.

Over the second half cycle, as the patch moves back across the headland tip, the material near the headland moves earlier and more quickly back toward the east, causing a fold to occur in a different part of the patch (Figure 5-1e). The result after 1 complete cycle is a highly deformed patch which is markedly different from the initial shape (Figure 5-1f). Figure 5-2 shows the increase of the patch perimeter over the tidal cycle, and the best fit exponential curve. The e-folding time scale is about 6 lunar hours, roughly equivalent to the half cycle time. Exponential growth of the perimeter (or the distance between neighboring particles) is an indication of mixing, since this implies that if the model were run backwards, small errors in the perimeter of the patch would be magnified in time so that the initial patch could not be recovered. In other words, the process in practice is irreversible even in the absence of diffusion. In addition, the increasingly convoluted boundary of the box allows the bottom generated turbulence, which acts at the scale of the water depth, to break down effectively the high wavenumber structure evidenced by the filaments in Figure 5-1f.

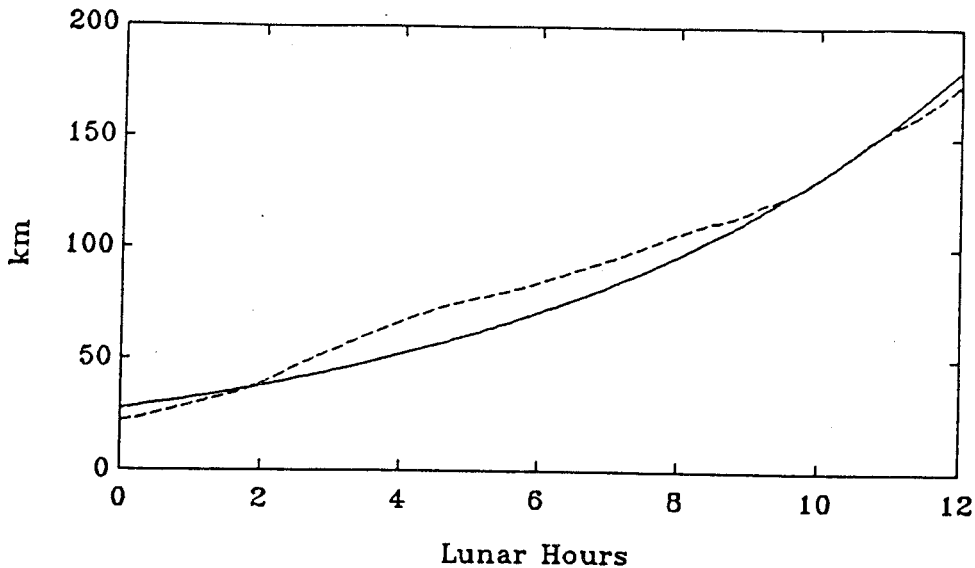


Figure 5-2: Growth of the box perimeter from Figure 5-1 with time, together with the best-fit exponential curve. The e-folding scale is approximately half a tidal cycle.

5.3 The Eulerian and Lagrangian residual currents

The Eulerian residual current is often assumed to yield information about the long term transport of material. As discussed in section 1.2.3, however, if there are substantial variations in the Eulerian velocity field over the length of the tidal excursion, the particle trajectories are strongly affected by these variations, and the Eulerian residual gives little information about the net displacement of particles over a tidal cycle.

This can be clearly seen by comparing the Eulerian residual velocity to the “Lagrangian residual velocity,” a quantity which indicates the average velocity of a particular particle over a tidal cycle (Zimmerman, 1979). This can be defined as the vector quantity formed by dividing the net particle displacements over a tidal cycle by the tidal period:

$$\overline{\mathbf{u}}_L(\mathbf{x}_0, t_0) \equiv \frac{\mathbf{x}(\mathbf{x}_0, t_0 + T) - \mathbf{x}_0}{T} \quad (5.1)$$

where T is the tidal period, \mathbf{x}_0 is the location of the particle at t_0 , and $\mathbf{x}(\mathbf{x}_0, t_0 + T)$ is the location of the particle one tidal cycle later. If the Lagrangian residual velocities are scaled by the tidal period, then this field expresses the transformation which maps particle

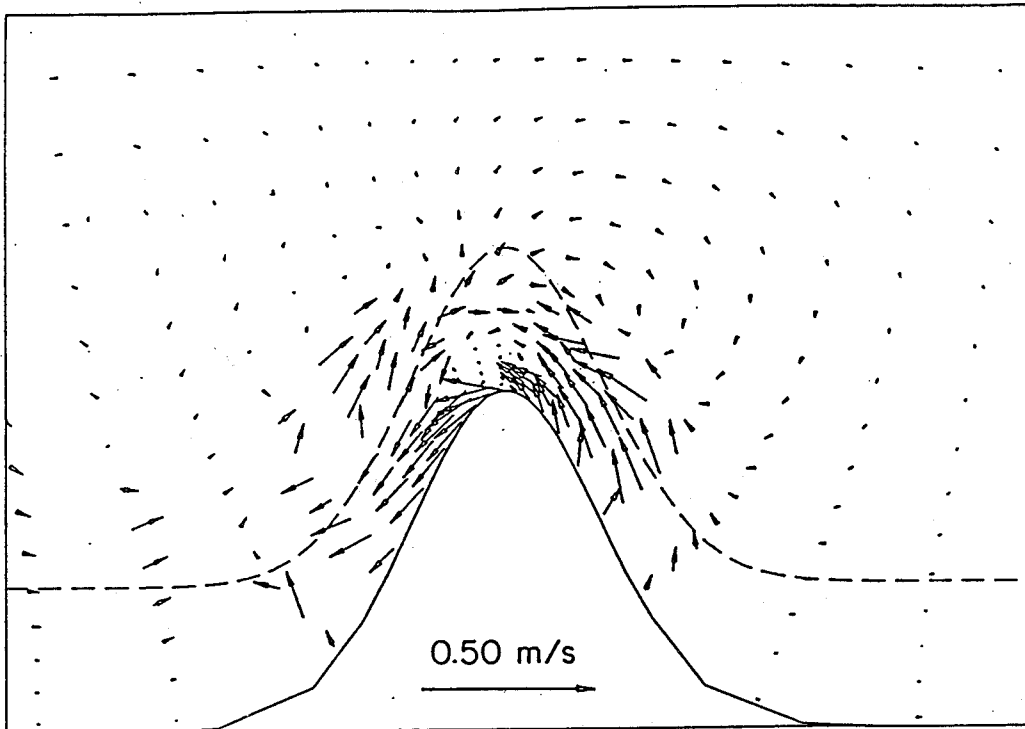


Figure 5-3: The Lagrangian residual velocity calculated at 0 lunar hours. This quantity is obtained by tracking a particle released at each grid point at a particular phase of the tide over a complete cycle. The net displacement of the particle over the cycle is then divided by the tidal period, forming a vector quantity, and is assigned to the release point. This field, if scaled by the tidal period, expresses the transformation that maps particle positions at a specified phase of the tide onto new positions one tidal cycle later.

positions at a specified phase of the tide onto new positions one tidal cycle later. Since the flow is periodic, this map (if calculated at infinite spatial resolution) contains all the information to calculate the subsequent evolution of particles released at a given phase of the tide. The path traveled by a released particle varies dramatically depending upon the phase of the tide at the time of release. The Lagrangian residual, therefore, also varies as a function of release phase.

The map of the Lagrangian residual corresponding to particles released at the beginning of the tidal cycle was constructed and is shown in Figure 5-3. In contrast to the Eulerian residual (Figure 5-4), far away from the headland the Lagrangian residual field is relatively

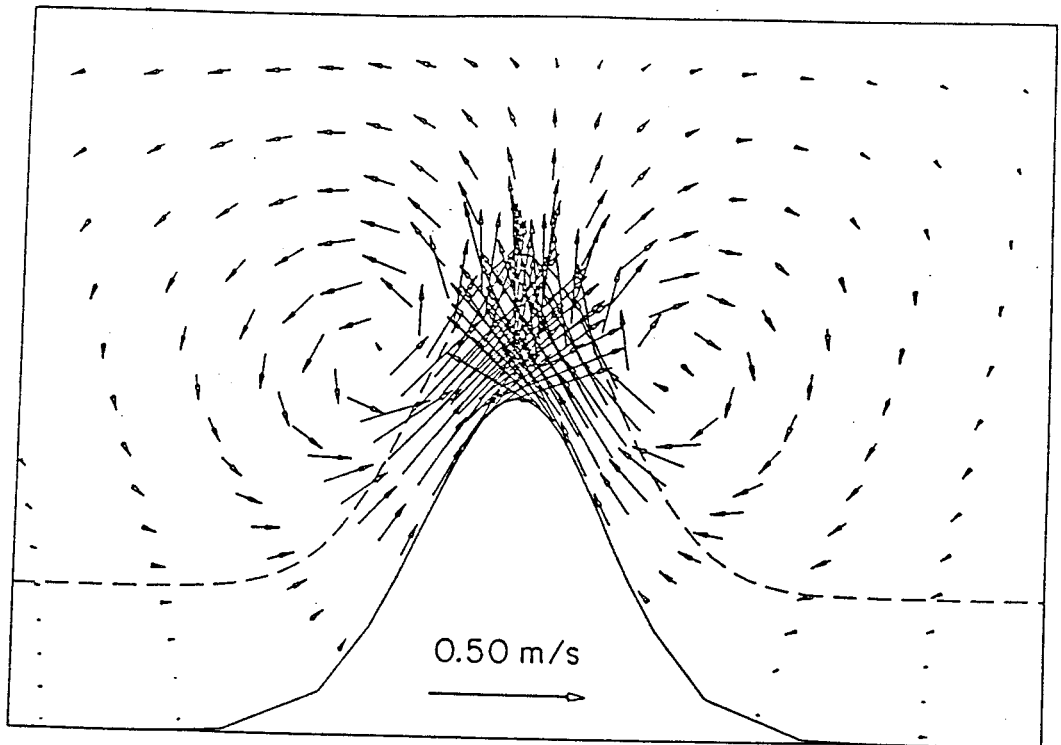


Figure 5-4: The Eulerian tide-induced residual flow, obtained by averaging the depth-averaged flow at each grid point over a tidal cycle.

smooth, but near the headland there is a region of rapid variation which is unresolved by the plotted vectors. If the vectors are plotted with higher resolution, the structure has more detail, but is still not fully resolved. In fact, particles arbitrarily close together can become widely separated over a tidal cycle, indicating chaotic behavior of the particle trajectories in this region. The implication of this map for dispersion is that a patch of material released in this region will be strongly stretched and deformed, while a patch released far away from the headland will exhibit some residual displacement, but will not be strongly deformed. Maps of the Lagrangian residual at other phases of the tide, while displaying much different local particle displacements, share this common global feature: they all reveal that material in a certain region near the headland will be strongly deformed, while material far away from the headland will not.

5.4 Dispersion experiments

5.4.1 Dispersion from a point release: an example

To illustrate the key aspects of the dispersion process and how it evolves with time, two rectangular patches of 900 particles each were released at 0 lunar hours (the start of eastward flow) in the Case A flow field (where $A_H=1 \text{ m}^2 \text{ s}^{-1}$) and tracked for 24 tidal cycles. The first patch was 200 m wide and released 3.5 km north of the tip, while the second patch was 100 m wide and released 0.2 km north (Figure 5-5a). After 6 tidal cycles (Figure 5-5b), the outer patch, released in a region of low strain, has migrated a few kilometers eastward, but has spread very little, while the inner patch, released in a region of high strain associated with the flow separation, has been distributed over a large area. Along the east edge of the inner patch distribution, multiple bands of material indicate successive injections of material from the flow separation, which deform relatively little after reaching the interior. After 12 tidal cycles, the outer patch and the bands of inner patch material have advected to the southeast, slowing recirculating back into the region of strong deformation (Figure 5-5c). This recirculation pattern is also seen in the map of the Lagrangian residual (Figure 5-3). After 24 tidal cycles, part of the outer patch has finally made its way back into the region of strong deformation and has been injected into the interior (Figure 5-5d). Outer patch material is being stretched by the flow separation and wrapped around the transient eddy. The inner patch material is continuing to evolve, with a tongue protruding to the west along the northern boundary and the bands along the southeast folding back into the interior.

The patch spreading over the 24 tidal cycles can be quantified by calculating the change in variance of the particle locations over a tidal cycle. In an infinite fluid of uniform diffusivity, the variance of particle position evolves according to $\sigma^2 = 2Dt$ where D is the diffusivity, and t is the elapsed time since release. In order to compare the spreading by deterministic motions to the spreading by turbulent diffusion, we define a dispersion coefficient

$$K(t) \equiv \frac{1}{2}(K_x(t) + K_y(t)) = \frac{1}{4} \left(\frac{\sigma_x^2(t+T) - \sigma_x^2(t)}{T} + \frac{\sigma_y^2(t+T) - \sigma_y^2(t)}{T} \right) \quad (5.2)$$

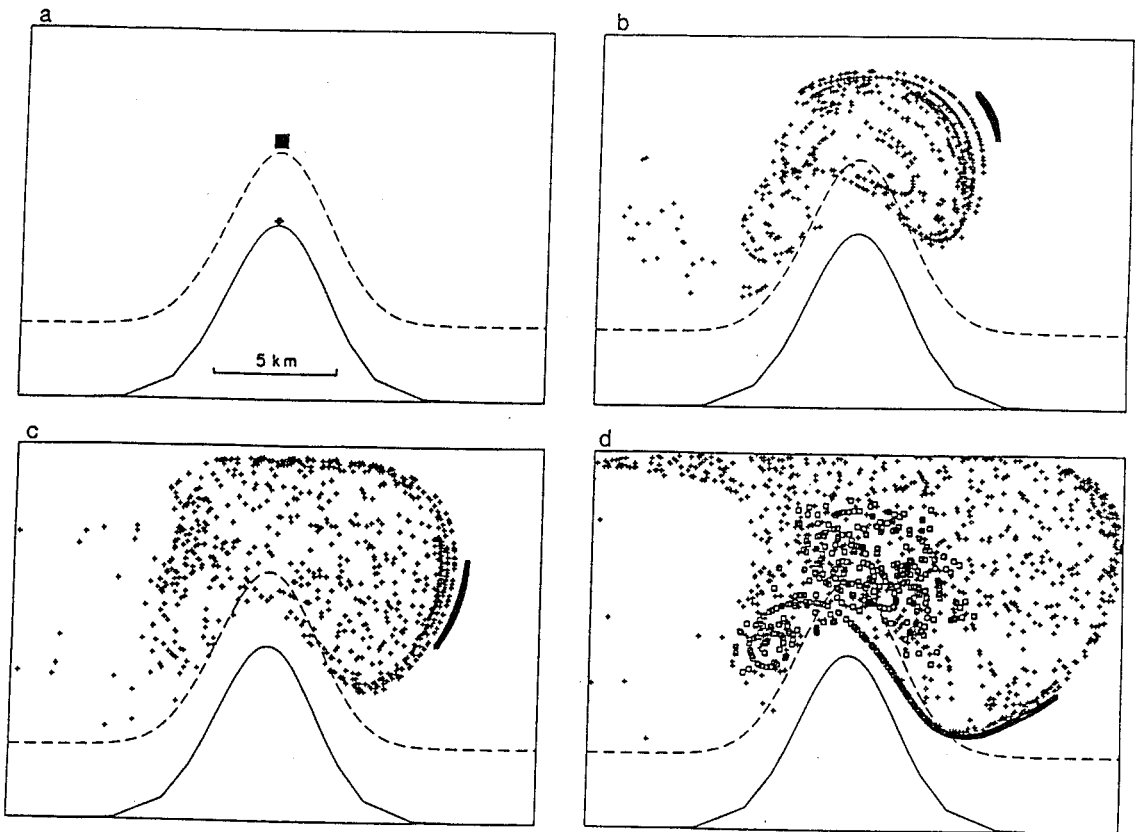


Figure 5-5: Dispersion of two patches of material released at 0 lunar hours. (a) Particle positions at 0 lunar hours (release configuration). The outer patch is initially 200 m wide and is released 3.5 km north of the tip (open boxes). The second patch is 100 m wide and released at 0.2 km north of the tip (pluses). (b) Particle positions 6 tidal cycles after release. (c) Particle positions 12 tidal cycles after release. (d) Particle positions 24 tidal cycles after release.

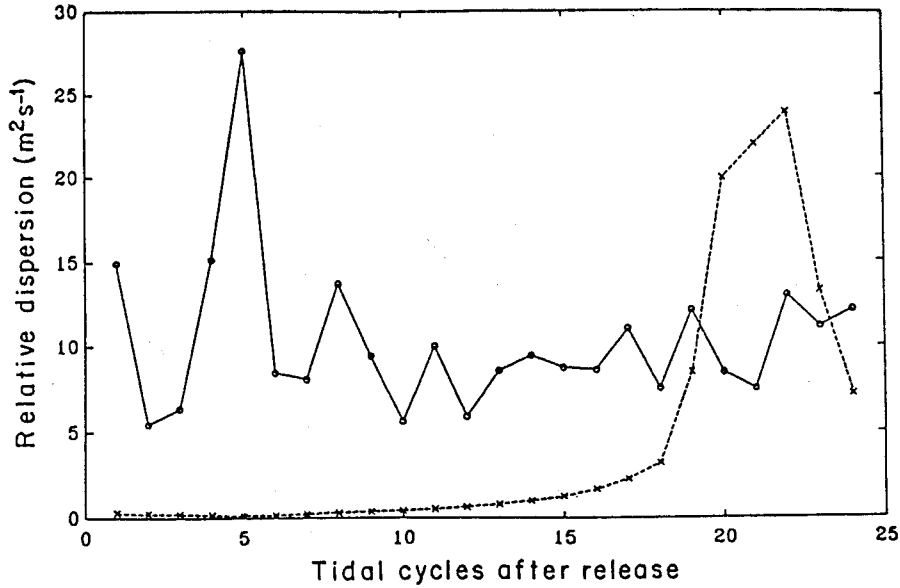


Figure 5-6: Time sequence of relative dispersion. The effective relative dispersion K (defined in text) is shown for the inner patch (solid line) and the outer patch (dashed line). The dispersion is calculated between successive tidal cycles only.

where σ_x and σ_y are defined by

$$\sigma_x^2(t) \equiv \frac{1}{N} \sum_{i=1}^N (x_i(t) - \bar{x}(t))^2, \quad (5.3)$$

$$\sigma_y^2(t) \equiv \frac{1}{N} \sum_{i=1}^N (y_i(t) - \bar{y}(t))^2, \quad (5.4)$$

T is the tidal period, (x_i, y_i) , $i = 1, \dots, N$ are the particle locations at time t , and (\bar{x}, \bar{y}) are the coordinates of the particles' center of mass. In the deterministic mixing process, K only describes the growth in the average variance of the patch: it does not completely describe the distribution, which requires higher-order moments to represent attributes such as streakiness.

Figure 5-6 shows the time sequence of the dispersion coefficient K for the inner and outer patches at intervals of 1 tidal cycle after release. For the inner patch, K varies rapidly from less than 6 to more than 27 $\text{m}^2 \text{s}^{-1}$ over the first eight tidal cycles, then fluctuates from 7 to 13 $\text{m}^2 \text{s}^{-1}$ for the duration of the simulation. For the outer patch, K increases slowly from less than 1 to 3 $\text{m}^2 \text{s}^{-1}$ over 18 tidal cycles, suddenly leaps to 20 $\text{m}^2 \text{s}^{-1}$ at 20 cycles,

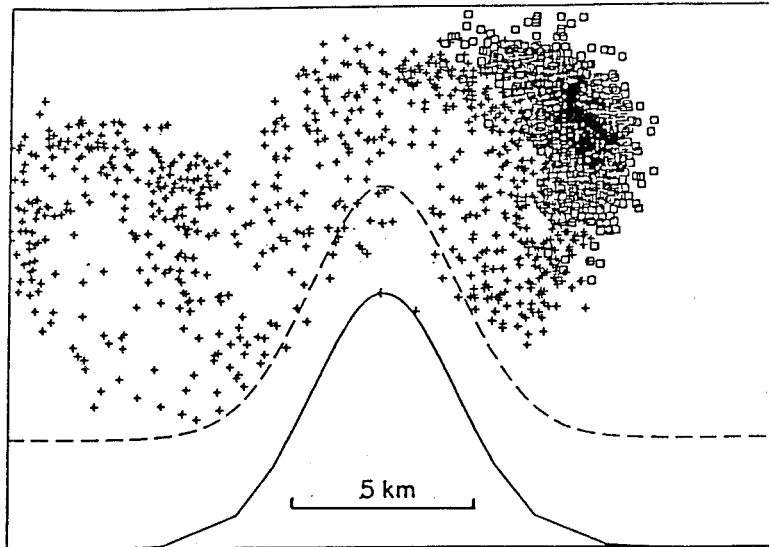


Figure 5-7: Dispersion of two patches with turbulence. Same as Figure 5-5b, but with $1 \text{ m}^2 \text{ s}^{-1}$ diffusion included using a random walk Markov-chain model.

then falls back to around $7 \text{ m}^2 \text{ s}^{-1}$ at 24 cycles. These values of dispersion are not as large as the values found by Zimmerman (1976) and Awaji (1982), probably due in part to the increased strength of the tide in their studies. The values are high enough to represent an important mixing mechanism, however, since dispersion due solely to three-dimensional turbulence would be on the order $1 \text{ m}^2 \text{ s}^{-1}$, the level of eddy viscosity in Case A.

Awaji (1982) found that the inclusion of small levels of turbulence in the tracking of particles led to large changes in local mixing characteristics. To assess the impact of diffusion on our dispersion results, the patch dispersion simulation was repeated including a Markov-chain model with $1 \text{ m}^2 \text{ s}^{-1}$ diffusion. Comparing the turbulent case after 6 tidal cycles (Figure 5-7) to the non-turbulent case (Figure 5-5b), the outer patch has spread laterally in a gradient-diffusive manner. The effect of turbulence on the inner patch, however, has not only smeared out the banded structure, but has resulted in the formation of a new lobe of the distribution to the west of the headland. This illustrates the sensitivity of the distribution at a given time to small perturbations at an earlier time.

5.4.2 Parameter dependence of dispersion

The nature of tidal currents around headlands was seen in section 4.4.1 to depend strongly upon the geometry, tidal forcing and the level of frictional damping. In this section it is shown that the mixing characteristics also are sensitive to these parameters. By varying the level of friction and the aspect ratio, it is found that the magnitude and spatial extent of dispersion increases with the amount of transient eddy activity (or vorticity) in the interior.

To compare the degree of dispersion between cases, patches of particles were released for each case at 3 lunar hours (\approx maximum eastward flow) from each grid cell in the domain and tracked for one tidal cycle. Each patch consisted of 16 particles with an initial Gaussian distribution defined by a standard deviation of 20 m. After tracking each patch for 12 lunar hours, the dispersion coefficient defined by (5.2) was calculated from the increase in variance of the patch particles over the cycle. The maps of dispersion obtained by this method indicate the extent of the region surrounding the headland over which released material actively mixes during a tidal cycle. The dispersion maps were obtained for five cases (Table 4.3): the basic case (Case 1), two frictional variation cases (Cases 2 and 4), and the two aspect ratio variation cases (Cases 7 and 8).

In the basic case, there are two bands surrounding the headland tip in which the dispersion coefficient indicates significant mixing takes place over a tidal cycle (Figure 5-8a). "Significant mixing" is used here to mean a dispersion coefficient greater than $1 \text{ m}^2 \text{ s}^{-1}$, which is the magnitude of mixing expected due to tidal turbulence. The distribution is very patchy, indicating the basic nature of the mixing process that was illustrated in section 5.2. Patches which undergo strong deformation over the tidal cycle may have initial locations very close to patches which undergo virtually no deformation. The total area over which significant mixing occurs is roughly 4 km^2 .

If the bottom friction is increased and decreased by a factor of two, large changes in the dispersion fields result. For the increased friction case (Case 2), the frictional decay scale is shorter than the tidal excursion, eddies decay rapidly, and the region of significant mixing decreases to less than 1 km^2 (Figure 5-8b). When the frictional decay scale becomes significantly longer than the tidal excursion (Case 4), the region of mixing increases to more than 20 km^2 (Figure 5-8c).

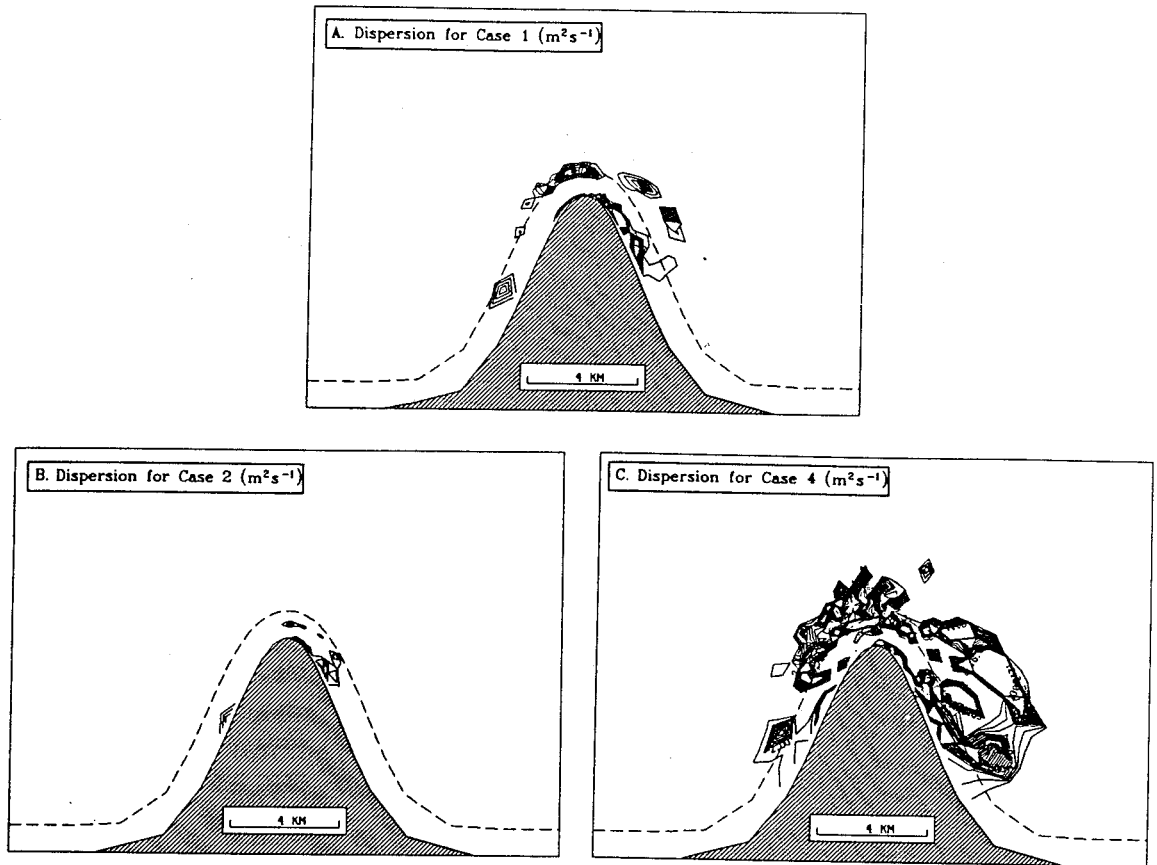


Figure 5-8: Dispersion coefficient for Cases 1, 2 and 4 based on the release of particles at 3 lunar hours tracked for one tidal cycle. In Case 2, the frictional decay scale is half as large as in Case 1. In Case 4, the frictional decay scale is twice as large as in Case 1. Contours are from 1 to 20 $m^2 s^{-1}$ in intervals of 1 $m^2 s^{-1}$.

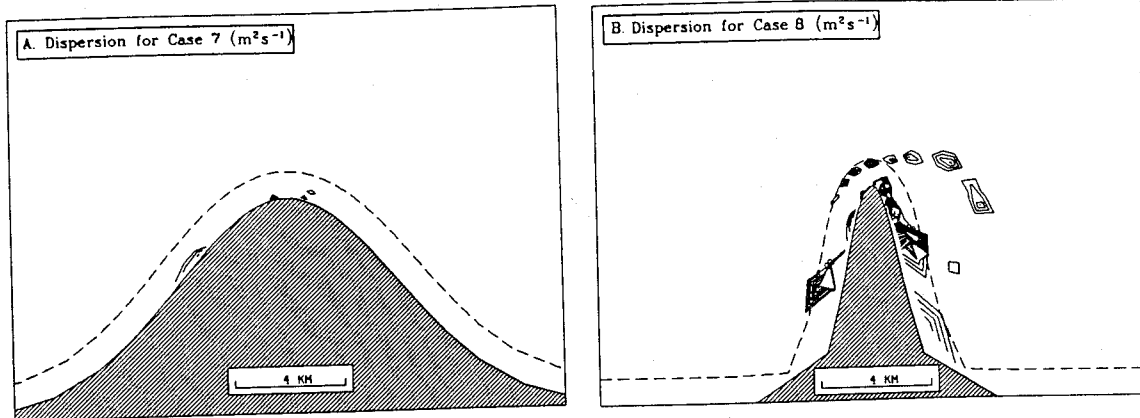


Figure 5-9: Same as Figure 5-8 except for Case 7, a smooth headland with aspect ratio 2, and Case 8, a sharp headland with aspect ratio 8.

The dispersion maps obtained for cases of varying aspect ratio also tend to reflect the degree of flow separation and eddy formation. For the gentle headland case (Case 7), there is virtually no region of significant mixing since the flow does not separate, vorticity is limited to the boundary layer, and transient eddies do not form (Figure 5-9a). In the sharp headland case (Case 8), the region of mixing is about the same as the basic case, again supporting the arguments of section 4.6 that once the headland is sharp enough for the flow to generate transient eddies, increasing the sharpness has little additional effect (Figure 5-9b).

5.5 Discussion

In the absence of stochastic processes, mixing occurs as the result of material being repeatedly stretched and folded (e.g., Ottino, 1988), like the action of an egg beater blending a viscous batter. Material is stretched when it passes through regions of high strain; if the stretching is exponential in time (as surrounding a point of pure strain), then reversal of the stretching process is unstable to infinitesimal perturbations, and deformed material cannot be restored to its original shape. Thus "unmixing" is not possible.

If the stretching is linear in time (e.g., an oscillatory parallel shear flow), then the

stretching process may be reversible and mixing need not occur. The mixing in a given area depends on the character of the strain field, and also on the large-scale structure of the flow which determines the frequency with which material interacts with the regions of high strain.

In this study of tidal dispersion around a headland, the snapshots of the flow field over the tidal cycle illustrate that material is rapidly stretched in the vicinity of the flow separation at the headland tip. As a tongue of material is drawn away from the tip, it begins to wrap around the core of the forming lee eddy, and it continues to wrap until the vorticity of the eddy decays to zero. The wrapped tongue of material is not subsequently unwrapped by the flow, but it also does not soon return to the vicinity of the flow separation. In fact, by examining the Lagrangian residual (Figure 5-3) and the recirculation time of outer patch material in the dispersion experiment (Figure 5-5), the period between successive interactions with the region of high strain for this particular flow field appears to be 10–20 tidal cycles. Since it takes many stretching and folding operations for a fluid to become well mixed, the time scale for material around the headland to achieve maximum variance, in this case study, may be hundreds of tidal cycles. In reality, material typically remains in the immediate vicinity of a particular headland for no more than a few days, due to advection by low-frequency currents of non-tidal origin. Over this period of time, the spreading of a patch in the vicinity of the headland will not have reached its asymptotic value. The distribution, therefore, will depend crucially on the initial release location and phase of the tide, since this will determine how soon the patch will interact with the region of high strain. The distribution of particles in the patch over several days must also be expected to have a streaky, patchy nature due to the limited amount of stretching and folding that has taken place.

The inclusion of turbulent mixing has basically two effects on the dispersion of material by deterministic processes. The first effect is to allow a particle traveling along a deterministic trajectory to “jump” to another trajectory through the random motions of the turbulence. Since even small changes in position can lead to large particle separations in a region of high strain, the distribution of particles in the turbulent case may look quite different from the non-turbulent case. This was first discussed by Awaji (1982). The second effect

of turbulent mixing is to smear out the streakiness of the deterministic particle distribution, since diffusive processes rapidly decrease the amplitude of short wavelength structure. Of course, if the turbulent fluctuations are large enough, i.e. if the time scale required to diffuse material over the region influenced by nonlinear tidal effects is short compared to the time scale over which mixing is of interest, then the mixing due to deterministic processes will be of minor importance.

The parameter dependence showed that the mixing due to deterministic movements of the tidal flow is related to the characteristics of the Eulerian flow field discussed in Chapters 3 and 4. If the flow does not separate, then mixing does not occur, as vorticity is limited to the boundary layer and the deformation that results from the shear flow at the boundary over a given half cycle is reversed on the following half cycle. If the flow does separate, then irreversible deformation occurs, and effective mixing takes place. The mixing increases with the activity and longevity of the transient eddies, which in turn depends on the decay scale of bottom friction relative to the tidal excursion.

In this idealized numerical study, we have shown that a tidal flow field around an isolated headland can cause effective mixing of material. In the real ocean, however, there will be low-frequency wind and density induced currents, as well as the possibility of multiple bathymetric and coastline features. Clearly these effects will modify the results presented here. Low-frequency motions would cause a broader area to be influenced by the headland effects. Material released in the vicinity of the headland would be advected out of the area of nonlinear tidal effects after being stretched once or twice, if at all. In our case study, for example, an along-shore flow of 0.05 m s^{-1} would replace the water in the region of the headland in 3 days (6 semi-diurnal tidal cycles). A substance released near the headland would not be homogenized in that period of time, and it may not even be mixed appreciably if it doesn't encounter the flow separation. Multiple headlands or bottom bumps, of course, could allow further spreading of material once it left the direct influence of a particular feature. For a sufficient number of features, one may enter the regime discussed by Zimmerman (1976) and Pasmanter (1988), where fields of tide-induced residual eddies interact with the oscillatory flow to act diffusively over large scales.

In conclusion, the deterministic motions of a tidal flow around a headland can be an

effective dispersive mechanism. The basic mixing mechanism is the stretching of material in a high strain region associated with the flow separation, followed by wrapping of this material around the transient eddies. Because the dispersion depends on the infrequent interaction of material with a small region of high strain, the spreading of an individual patch is extremely sensitive to the initial release location and phase of the tide. This implies that the distribution of particles from a released patch may be expected to be streaky and non-Gaussian over many tidal cycles.

Chapter 6

Summary and Conclusions

This thesis focuses on the dynamics and dispersion of shallow tidal flow around headlands with alongshore length scales that are comparable to or less than the scale of the tidal excursion. The nature of the tidal flow around this class of headlands is strongly nonlinear, characterized by flow separation near the headland tip and transient eddy formation. The rotational flow associated with these eddies strongly affects the basic tidal flow. This marks the point of departure from most previous studies that have treated the rotational flow as a perturbation on the basic tidal flow (Huthnance, 1973; Zimmerman, 1978; Loder, 1980, Robinson, 1981). While approximate analytic methods are used to obtain solutions in these weakly nonlinear studies, numerical models must be used to obtain solutions in separating tidal flow around headlands. The essential elements of the solution, however, may be understood with simpler models which represent the flow separation process and the transport and damping of vorticity away from the headland. These simple models clearly identify the parameter dependence of the flow separation and wake evolution.

In Chapter 2, it is shown that for shallow, vigorous tidal flows, phase variation and rotation of the tidal current with depth is small enough so that depth-averaged physics are appropriate. This allows the governing equations to be considerably simplified, and the solutions can be obtained with a two-dimensional tidal model whose characteristics are well known.

In Chapter 3, a detailed look at the results from this model for strongly nonlinear flow around a headland reveals that during each half cycle a transient eddy is formed which

strongly affects the nature of the flow. Transient eddy formation is explained in terms of vorticity dynamics. During each half tidal cycle, vorticity is produced in a narrow boundary layer along the boundary upstream of the headland tip. Near the tip, the high vorticity layer separates from the coast, whereupon it wraps up, forming a large blob of concentrated vorticity in the lee of the headland. The concentrated vorticity shed as a result of a rapid change in speed is referred to in aeronautics as a start-up vortex. In separating tidal flow around headlands, the oscillatory nature of the forcing generates start-up eddies during each half cycle, and these eddies drive strong recirculation in the lee of the headland.

In Chapter 4, it is shown that for transient eddies to form in the interior, the flow must separate. If the flow does not separate, then vorticity produced in the boundary layer remains largely in the boundary layer, and transient eddies cannot form. An idealized model of flow separation, based on irrotational interior flow and a narrow boundary layer in which vorticity is produced, shows that flow separation occurs when the pressure gradient switches from favorable (accelerating) to adverse (decelerating) along the boundary of the headland. This, in turn, occurs when the advective term in the alongshore momentum equation is larger than the frictional and time-dependent terms. The advective term is shown to be sensitive to the headland aspect ratio $[b/a]$, where b is the width scale (offshore extent), and a is the length scale (alongshore extent). For a given headland geometry, however, whether the pressure gradient changes from favorable to adverse along the boundary depends on two parameters that determine the scale of the advective term relative to the friction and time-dependent terms. The parameter relating advection to bottom friction is an equivalent Reynolds number $Re_f = [H/C_D a]$, where H is the interior water depth and C_D is the depth-averaged drag coefficient. For a particular headland geometry, there is a value of Re_f below which flow separation does not occur, as friction dominates advection to the degree that the pressure gradient is always favorable. The parameter relating advection to time-dependence is the Keulegan-Carpenter number $K_c = [U_o/\sigma a]$, where U_o is the amplitude and σ is the frequency of the far-field tidal flow. For a particular headland geometry, there is a value of K_c below which flow separation does not occur, as time-dependence dominates advection to the degree that the pressure gradient simultaneously changes sign along the entire headland.

The fact that the flow separates close to the point where the pressure gradient first

becomes adverse is determined by boundary layer theory. Using a boundary layer model, it is shown that as long as the depth becomes shallow near the coast, eddy viscosity and the no-slip condition have little effect on the boundary layer solution and the point of flow separation. While Tee (1977) noted that specifying a no-slip condition was essential in numerical models to correctly represent the vorticity, the work here shows that the no-slip condition is important only when the shallow depths at the coast are not well resolved by the model bathymetry.

The question of what happens to the boundary layer vorticity once it separates from the coast is also discussed in Chapter 4. It is shown that the structure of the vorticity distribution depends on the relative magnitudes of the tidal excursion $2U_o/\sigma$, the frictional decay length scale $H/2C_D$, and the alongshore headland length scale a . The downstream extent of the vorticity injected at the headland tip scales with the tidal excursion or the frictional length scale, whichever is smaller. The ratio of these two length scales $[\sigma H/4C_D U_o]$ indicates the lifetime of a particular vorticity patch expressed in units of tidal cycles. If the frictional length scale is much smaller than the tidal excursion, then vorticity persists for a fraction of a cycle, and vorticity produced during subsequent half cycles cannot interact. If the frictional length scale is much larger than the tidal excursion, the vorticity persists for multiple cycles and eddies produced during consecutive half cycles may interact.

The tidal excursion, frictional length scale and the headland length are combined to form two dimensionless parameters that describe the nature of the vorticity distribution. These are the same parameters that determine if flow separation occurs; the frictional Reynolds number $Re_f = [H/C_D a]$, which is proportional to the ratio of the frictional length scale to the headland length scale, and the Keulegan-Carpenter number $K_c = [U_o/\sigma a]$, which is proportional to the ratio of the tidal excursion to the headland length scale. There are three basic regimes: (1) a quasi-steady regime where friction dominates time-dependence ($Re_f \ll K_c$); (2) a regime where time-dependence and friction are comparable ($Re_f \approx K_c$); and (3) a regime where friction is weak compared to time-dependence ($Re_f \gg K_c$).

If the tidal flow is quasi-steady, the nature of the tidal flow around a headland of a particular aspect ratio will depend primarily on the frictional Reynolds number Re_f , as this parameter will determine both if the flow separates and the extent of the wake relative

to the headland length. If Re_f is smaller than a critical value (that is a function of the headland shape α), the flow will not separate, as the flow is everywhere down pressure gradient. Above the critical value the flow separates and the separation streamline bounds a weak recirculating region downstream of the headland, the downstream extent of which grows with increasing Re_f .

When the frictional length scale is comparable to the tidal excursion, the start-up vortex plays an important role in determining the flow field. In this case, when Re_f (or equivalently K_c , since they are comparable in this regime) exceeds the critical value, the flow separates, and a start-up eddy is formed. For $Re_f \approx 1$, the start-up eddy grows to the size of the headland scale and affects the flow near the headland throughout the half-cycle. This results in strong recirculation in the lee of the headland, as opposed to the weak recirculation in the quasi-steady case. As Re_f increases, the start-up eddy moves downstream from the headland, but the extent of its movement is significantly less than the tidal excursion due to interaction with its image eddy.

When the frictional length scale is much larger than the tidal excursion, then vorticity produced during subsequent half cycles may interact, and the nature of the resulting flow is determined by K_c , which is proportional to the ratio of the tidal excursion to the scale of the headland. If the tidal excursion is much smaller than the scale of the headland, the tide barely feels the influence of the coastline variation, the flow is quasi-linear, and flow separation does not occur. Above a critical value of Re_f , the flow separates, and a start-up eddy forms during each half cycle that may pair with previously formed eddies. In this case, the extent of the vorticity is not limited by the tidal excursion, as eddies interact and propagate according to their mutually induced velocities.

In previous work on separating tidal flow around an island, Wolanski et al. (1984) proposed that the structure of the flow was controlled solely by an "island wake parameter", a parameter that has a similar physical interpretation to Re_f . From the work in this thesis, it is clear that this parameter will solely determine the nature of the wake only under quasi-steady conditions. In many tidal flows, K_c is comparable to Re_f and the start-up vortex plays an important role in the structure of the flow. In fact, at Rattray Island, where Wolanski et al. applied the island wake parameter, scaling shows that K_c is comparable

to Re_f , indicating that time-dependent effects are important. Evidence was provided by the strong recirculation that was measured by Wolanski et al. in the lee of the headland, a feature incompatible with the quasi-steady flow, but easily explained by the presence of a start-up eddy.

Another aspect of the vorticity dynamics explored in this thesis is the strength of the wake. For regimes where eddies do not interact, (K_c is comparable to or greater than Re_f), a simple model represents the integrated vorticity outside the boundary layer, based on the vorticity flux at the headland tip and the degree of bottom frictional damping. The vorticity flux at the headland tip depends on the thickness of the boundary layer relative to the width (offshore extent) of the headland and the square of the far-field velocity. The boundary layer thickness depends on the width of the sloping bottom region, the tidal excursion, the frictional length scale and the headland length scale. Increasing the tidal excursion or the headland length scale causes the boundary layer to thicken, resulting in less vorticity flux. Increasing the frictional length scale or the aspect ratio causes the boundary layer to thin, resulting in more vorticity flux. This vorticity flux forces a circulation that is limited by frictional damping, the magnitude of which is determined by the ratio of the tidal excursion to the frictional length scale. The larger this ratio, the more strongly the vorticity is damped by bottom friction and the smaller the strength of the wake.

The results of the simple model describing the wake strength point out the importance of adequate grid resolution near the headland tip. The total vorticity flux at the tip, which drives the circulation in the wake, depends on the square of the velocity at the edge of the boundary layer. Tee (1976) argued that because the flux depends only on the velocity at the edge of the boundary layer, the correct flux can be obtained without resolving the structure of the layer. The velocity at the edge of the boundary layer, however, depends on the boundary layer thickness, since the irrotational flow field varies strongly around the tip of a sharp headland. A thinner boundary layer has a greater velocity at the edge of the layer, since the irrotational flow is greater closer to the tip, and leads to greater vorticity flux. Thus a numerical model which does not resolve the boundary layer causes the velocity at the edge of the layer to be underestimated. This means that the vorticity flux will be underestimated, and the resulting wake strength, as well as the harmonic and residual

circulation, will be too weak. In the present study, the use of curvilinear coordinates provides high resolution near the headland tip, and the vorticity flux is accurately represented. The use of curvilinear orthogonal coordinates to represent the highly convoluted coastlines of realistic embayments, however, may not be feasible, and an interesting topic for further work is the degree to which high-resolution rectangular grid models can accurately represent the dynamics of separating flow around a headland.

In Chapter 5, tide-induced dispersion is shown to be strongly dependent on the nature of the tidal flow around the headland. In weakly nonlinear, non-separating conditions, material advects back and forth at the fundamental frequency, and small residual displacements of particles result. If the tidal excursion is much smaller than the headland length scale, then these small residual displacements are due to contributions from the Eulerian residual velocity and Stokes drift, while if the tidal excursion is comparable to or smaller than the headland length scale, the residual displacements may be more complicated, but still related to the Eulerian flow field (Zimmerman, 1979). In strongly nonlinear, separating conditions, residual displacements of particles may be large in the vicinity of the headland, comparable to the tidal excursion. In this case, the Eulerian residual velocity field bears no relation to the Lagrangian residual displacement velocities, and therefore contains no information regarding the transport of water-borne material. This supports the assertion of Imasato (1983) that the Eulerian residual velocity around rapid changes in the coastline (comparable to or less than the tidal excursion) is only a mathematical abstraction which has no physical significance.

The strong spatial gradients found in separating flow around a headland are responsible for dispersion of material in the vicinity of the headland. The straining associated with the separated shear layer and transient vortices results in strong deformation of fluid parcels. For patches of material in the vicinity of the headland, the effect of this straining is to cause the variance of the particles constituting the patch to grow with time. This dispersion process is only active in a finite area surrounding the headland, however, corresponding to the area in which significant vorticity exists. The stretching and folding of material around a tidal headland takes many tidal cycles to homogenize material released within this region. As a result, over several tidal cycles, the distribution of material is extremely patchy and

streaky, in contrast to the smooth distributions resulting from gradient-type diffusion. The results of this study differ from realistic tidal flows, in which the presence of low-frequency currents of non-tidal origin will typically advect material out of the immediate vicinity of the headland over a time scale of several tidal cycles. As a result, homogenization does not have time to occur, and patches and streaks of partially mixed material will be carried away from the mixing region.

This thesis analyzed the nature of tidal flow and tide-induced dispersion around an idealized, isolated headland in shallow water. The goal was to identify the important processes that determine the nature of the tidal flow, and to understand the basic physics which control these processes. Toward this goal, flow separation and the formation of transient eddies have been identified as key processes which strongly affect tidal currents and mixing around headlands. Flow separation is important because it allows boundary layer vorticity to penetrate the interior, and is shown to depend on the geometry of the headland, the tidal excursion, and the frictional length scale. The formation of transient eddies is important because it drives strong recirculating flow in the vicinity of the headland, and is shown to depend on flow separation and the oscillatory nature of the flow. Bottom friction plays a critical role in determining the evolution of the eddy. Future work will focus on realistic flow simulations of observed flows, such as those measured by Geyer and Signell (1989) at Gay Head, Massachusetts, and simulation of dispersion in realistic flows. This study indicates that high spatial resolution near the headland tip and realistic representation of the bottom friction will be of critical importance to obtain accurate results.

Appendix A

Details of the Numerical Model

A.1 The basic difference scheme

The equations (2.21-2.22) were solved with finite difference technique based on Flather and Heaps (1975). The equations (2.21-2.22) were discretized on a Richardson grid, a time-staggered form of the Arakawa C-Grid (see Mesinger and Arakawa, 1976). Figure A-1 illustrates the nature of the grid. At time level n , the grid consists of only velocity points, and each cell consists of u_1 -points at the center of each of the x_2 directed sides, and u_2 -points at the centers of the x_1 directed sides. At time level $n + 1/2$, the grid consists of only elevation points located at the cell centers.

The basic numerical approach to solving the governing equations on the Richardson grid is best described using a simple example. Consider the case of non-rotating linear gravity waves travelling in the x_1 direction in a rectangular, flat-bottomed domain. In this case, the momentum and continuity equations are simply

$$\frac{\partial u_1}{\partial t} = -\frac{gh}{s_1} \frac{\partial \eta}{\partial x_1}, \quad (\text{A.1})$$

$$\frac{\partial \eta}{\partial t} = -\frac{1}{s_1} \frac{\partial u_1 h}{\partial x_1}. \quad (\text{A.2})$$

The equations are then discretized as

$$\frac{u_{1(i+1/2)}^{n+1} - u_{1(i+1/2)}^n}{\Delta t} = -\frac{gh_{i+1/2}}{s_{1(i+1/2)}} \left[\eta_{i+1}^{n+1/2} - \eta_i^{n+1/2} \right], \quad (\text{A.3})$$

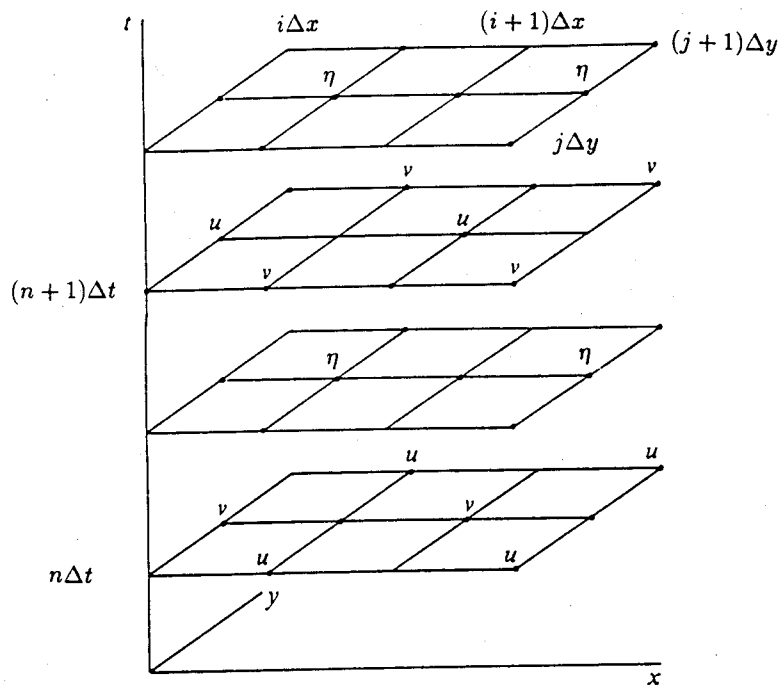


Figure A-1: Schematic of Richardson grid. The space-time grid is staggered both in space and time, with velocities and elevations evaluated at alternate half time unit intervals.

$$\frac{\eta_i^{n+3/2} - \eta_i^{n+1/2}}{\Delta t} = -\frac{1}{s_{1(i)}} \left[u_{1(i+1/2)}^{n+1} h_{i+1/2} - u_{1(i-1/2)}^{n+1} h_{i-1/2} \right]. \quad (\text{A.4})$$

Starting from an initial specification of the velocity fields at time level n and the elevation field at time level $n + 1/2$, the velocity at time level $n + 1$ is first obtained by center differencing the x_1 momentum equation about time level $n + 1/2$. The scheme for the x_1 momentum equation is centered about fictitious u_1 -points at time level $n + 1/2$ shown as open circles in Figure A-1. The pressure gradient $(g/s_1)\partial\eta/\partial x_1$ at $n + 1/2$ is obtained by center differencing the surrounding η -points, and the local acceleration $\partial u/\partial t$ is obtained by center differencing the u_1 points from levels n and $n + 1$. This yields an expression for the velocity at $n + 1$ in terms of the velocity at n and the elevation at $n + 1/2$. Once the velocity at $n + 1$ is obtained, the continuity equation is solved in yield the elevation points at $n + 3/2$. The accuracy of this scheme is order $\Delta x^2, \Delta t^2$ and has no numerical damping (Mesinger and Arakawa, 1976). The scheme is stable provided that the Courant-Friedrichs-Lewy (CFL) condition

$$\Delta t < \left[\frac{\Delta x}{\sqrt{gh}} \right]_{max}. \quad (\text{A.5})$$

is satisfied (e.g. Richtmyer and Morton, 1967). This condition means that the distance the wave propagates in one time step must be less than the distance between points on the grid where the wave is evaluated. For linear wave propagation, the Richardson grid allows efficient centered-space, centered-time differencing.

As the dynamics become more complicated, with advection, bottom friction, Coriolis and diffusive terms, representation on the Richardson grid also becomes more complicated, and details can be found in Flather and Heaps (1975). When nonlinear terms are included, the equations are no longer strictly centered in time, and the accuracy degrades to order $\Delta x^2, \Delta t$. In practice, this is of little importance, as the time step to maintain stability is much smaller than the temporal scales of interest. In modifying the scheme for curvilinear coordinates, differencing was performed in such a way as to yield centered estimates in time and space as much as possible.

A.2 Advection scheme

Due to the importance of momentum advection in the vicinity of a rapidly varying coastline, the representation of these terms in the numerical scheme must be given special consideration. Using the “angled-derivative” scheme of Roberts and Weiss (1966), the velocity gradients at time level $n + 1/2$ are correctly centered in time and space, but the multiplying velocities are obtained from the old time level. If the scheme is applied to the linear advection equation

$$\frac{\partial \phi}{\partial t} = -C \frac{\partial \phi}{\partial x} \quad (\text{A.6})$$

where C is the speed of propagation of some quantity ϕ , some attributes of the scheme can be determined by considering the time-evolution of a particular wavenumber component $\phi_0 \exp ikx$. The exact solution, of course, is just $\phi = \phi_0 \exp[ik(x - Ct)]$. The numerical solution, however, is $\phi = \phi_0 \exp[ik(x - \hat{C}t)]$, where \hat{C} is a complex number that depends on the numerical scheme, the nondimensional wavenumber ($k\Delta x$), and the Courant number [$C\Delta t/\Delta x$]. Roberts and Weiss (1967) showed that the angled derivative scheme has no numerical damping, but the numerical phase speed becomes progressively slower for shorter wave components. Figure A-2 shows the numerical phase speed relative to the true phase speed as a function of wavelength and Courant number. The figure shows that if 80% accuracy in propagation speed is required, wavelengths must be at least $8\Delta x$ long. The shortest resolvable waves, with wavelength $2\Delta x$, have zero phase speed. The numerical dispersion of the angled derivative scheme is typical of second order difference methods for advection (Leonard, 1979). Although better phase accuracy could be obtained by using a higher-order advective scheme (e.g. Leonard, 1979; Schlesinger, 1985), it was decided to direct resources to refinement of the numerical grid to obtain the desired accuracy.

A.3 Shapiro filtering

High wavenumber components that are improperly represented by the numerical scheme should be filtered from the solution fields periodically, so that the energy at high wavenumber cannot affect lower wavenumber components through nonlinear interaction. An effective means of accomplishing this was described by Shapiro (1975), who presented linear filters

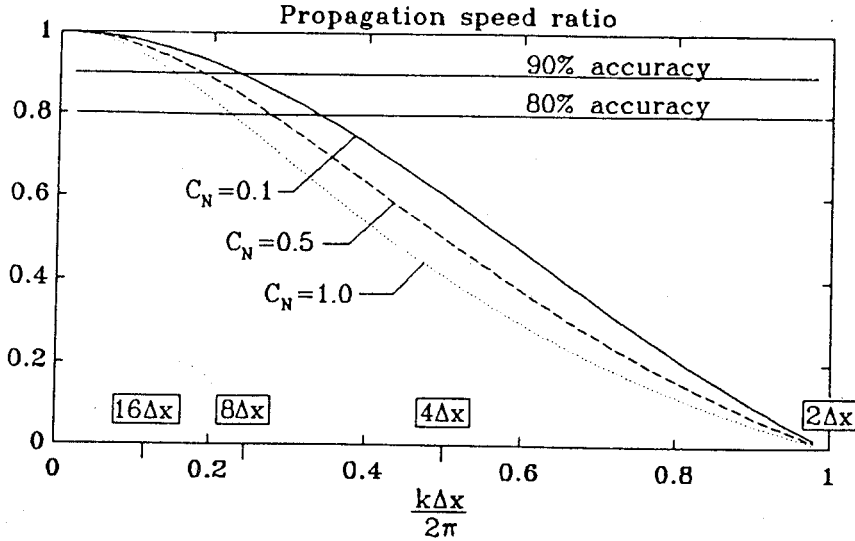


Figure A-2: Numerical phase speed for angled derivative advection scheme. The phase speed is plotted relative to the true phase speed at Courant numbers of 0.1, 0.5, and 1.0.

that completely eliminate $2\Delta x$ waves and minimize damping of lower wavenumber components. These filters are constructed by repeated passes of three point filters with varying filter weights for each pass. The number of passes is defined as the “order” of the filter, which determines the wavenumber response of the filter. The first order filter is equivalent to Laplacian diffusion with a diffusion coefficient of $D_1 = 0.25\Delta x^2/\Delta t$, while the second order filter is equivalent to bi-harmonic friction with a coefficient of $D_2 = -1/16(\Delta x^4/\Delta t)$. The desired order of the filter and the number of time steps between filter applications were determined by ensuring that the e-folding time-scales of the well-resolved wavenumber components ($> 6\Delta x$) were much longer than the tidal period (reduction of $< 10\%$ over a tidal cycle).

A.4 Boundary conditions

The model domain has closed boundaries at the north and south, and open boundaries at the east and west. Along the closed boundaries, the normal velocity u_2 is set to zero at the wall, which ensures no mass flux at the wall. The inclusion of horizontal eddy viscosity, with second order spatial derivatives, requires that another boundary condition be specified

to close the problem. In many viscous flow problems, a no-slip condition is applied at the boundary, since the fluid at the boundary adheres to the walls. In the tidal headland problem, flow in the immediate vicinity of the boundary is probably determined by processes that are not considered in the model, i.e. long-shore transport in the surf zone. In most cases, the no-slip condition is applied due to the lack of information, and the model can be run again with a free-slip boundary condition to determine the impact on the solution. Since no u_1 points occur along the solid boundary with a staggered grid, values are assigned to fictitious points u_{1B} located half a grid cell landward of the solid walls. The values at these fictitious points are then used in the estimation of the second derivatives at u_{1I} points located half a grid cell seaward of the boundary. The slip condition is specified by setting $u_{1B} = u_{1I}$, while the no-slip condition is specified by setting $u_{1B} = -u_{1I}$.

Along the open boundaries at the east and west ends of the domain, a variety of different conditions can be set. The forcing for the tidal problem can be specified by either elevation or the normal velocity component to the boundary. Using the continuity equation, the normal velocity component can be determined if the elevation is specified, and vice versa. Open boundaries can also be set with simple gravity wave radiation, where u_1 and η at the boundaries are assumed to satisfy

$$\frac{\partial \phi}{\partial t} = \pm C \frac{\partial \phi}{\partial x_1} \quad (\text{A.7})$$

where $C = \sqrt{gh}$ is the shallow water wave speed, and ϕ denotes either u_1 or η . The sign is chosen to let waves propagate out of the domain. A more complicated radiation condition which estimates phase speed directly from the model was also tried (Orlanski, 1976), but had little effect. In fact, the only importance of the open boundary conditions is to generate a fundamentally sinusoidal flow in the vicinity of the headland. For many coastal oceanographic problems, a careful treatment of open-boundary conditions is essential (Chapman, 1985), but in the headland problem transients are always allowed to die out before the tidal solution is analyzed, and the time-dependence of the free surface does not significantly affect the character of the periodic flow field, since the headland scale is much shorter than the tidal wavelength (section 4.2.1).

A.5 Time splitting

Although not required to solve the equations, a time-splitting procedure was adopted to improve the efficiency of the code on vector-processing computers such as the Cray X-MP at NCAR, where most of the modeling was performed. The time-splitting technique allows momentum to be propagated, advected and diffused in separate steps (Marchuk, 1974). The propagation and diffusion steps both vectorize, meaning that vector operations can be employed. This results in a significant speed-up over the scheme which solves the entire momentum equation at once. In addition, the advection and diffusion terms need not be computed at every time step, since the time step required for stability of the gravity wave step is much smaller than is required for stability of the advection and diffusion steps. This is particularly important since the advection step using the angled-derivative scheme does not vectorize. For example, in a typical model run, if the advective terms are computed every 5 time steps, the speed-up over the non-split scheme is nearly a factor of 5, with negligible change in accuracy due to the very small time steps required by the gravity wave stability (1-10 s). The time-splitting technique has been successfully used in weather prediction and storm surge modeling in the British Meteorological Office (Gadd, 1978).

A.6 Operational procedure

To obtain a periodic tidal solution for a particular basin, first the orthogonal curvilinear grid is created using the program developed by Wilkin (unpublished, 1988). With this program, the grid spacing along two boundaries may be fixed by the user, allowing a degree of control over the resolution in specific regions of the domain. Once the grid has been generated, the bathymetry is specified, and this allows the maximum time step to be estimated from the CFL condition, which in curvilinear coordinates can be expressed as

$$\Delta t < \min \left[\frac{s_1 s_2}{\sqrt{gh (s_1^2 + s_2^2)}} \right], \quad (\text{A.8})$$

where the right hand side is the minimum over the entire domain. This means that the smallest grid cell limits the model time step for a constant depth basin, but in a depth varying basin this need not be the case.

Once the maximum time step has been estimated, the parameters of the Shapiro filtering can be selected to minimally damp the wavelengths that are properly represented by the model.

References

- Abbott, M. B., J. Larsen, and J. Tao, Modelling circulations in depth-integrated flows, Part 1: The accumulation of the evidence, *Journal of Hydraulic Research*, 23, 397-426, 1985.
- Anderson, D. A., J. C. Tannehill, and R. H. Pletcher, *Computational fluid mechanics and heat transfer*, Hemisphere Publishing Corporation, 1984, 599 pp.
- Aref, H., Stirring by chaotic advection., *J. Fluid Mech.*, 143, 1-21, 1984.
- Awaji, T. A., Water mixing in a tidal current and the effect of turbulence on tidal exchange through a straight, *J. Phys. Oceanogr.*, 12, 501-514, 1982.
- Awaji, T. A., N. Imasato, and H. Kunishi, Tidal exchange through a strait: A numerical experiment using a simple model basin, *J. Phys. Oceanogr.*, 10, 1499-1508, 1980.
- Batchelor, G. K., *An Introduction to Fluid Dynamics*, Cambridge University Press, 1967, 615 pp.
- Bigelow, H. B., Physical oceanography of the Gulf of Maine, *Bull. U. S. Bur. Fish.*, 40, 511-1027, 1927.
- Caston, V. N. D. and A. H. Stride, Tidal sand movement between some linear sand banks in the North Sea off northeast Norfolk, *Marine Geology*, 9, M38-M42, 1970.
- Chapman, D. C., Numerical treatment of cross-shelf open boundaries in a barotropic coastal ocean model, *J. Phys. Oceanogr.*, 15, 1060-1075, 1985.
- Cheng, R. T. and V. Casulli, On Lagrangian residual currents with applications in South San Francisco Bay, California, *Water Resources Research*, 18, 1652-1662, 1982.
- Choi, B. H., *A tidal model of the Yellow Sea and the Eastern China Sea*, Technical Report 80-02, Korea Ocean Research and Development Institute, 1980, 72 pp.
- Flather, R. A. and N. S. Heaps, Tidal computations for Morecambe Bay, *Geophys. J. R. Astr. Soc.*, 42, 489-517, 1975.
- Gadd, A. J., A split explicit integration scheme for numerical weather prediction, *Quart. J. R. Met. Soc.*, 104, 569-582, 1978.
- Garrett, C. J. R. and R. H. Loucks, Upwelling along the Yarmouth shore of Nova Scotia, *J. Fish. Res. Bd. Can.*, 33, 116-117, 1976.
- Geyer, W. R. and R. P. Signell, Measurements of tidal flow around a headland with a shipboard acoustic Doppler current profiler, in *Proceedings of the International Conference on Tidal Hydrodynamics.*, edited by B. Parker, 1989, submitted.
- Gill, A. E., *Atmosphere-Ocean Dynamics*, vol. 30 of *International geophysics*, Academic Press, 1982, 662 pp.
- Hazel, P., Numerical studies of the stability of inviscid stratified shear flows, *J. Fluid Mech.*, 51,

39-61, 1972.

- Heaps, N. S., Linearized vertically-integrated equations for residual circulation in coastal seas, *Dt. hydrogr. Z.*, *31*, 147-169, 1978.
- Heaps, N. S. (ed.), *Three-dimensional coastal ocean models*, vol. 4 of *Coastal and Estuarine sciences*, American Geophysical Union, 1987, 208 pp.
- Huthnance, J. M., Tidal current asymmetries over the Norfolk Sandbanks, *Estuarine Coastal Mar. Sci.*, *1*, 89-99, 1973.
- Ianniello, J. P., Tidally induced residual currents in estuaries of variable breadth and depth, *J. Phys. Oceanogr.*, *9*, 962-974, 1979.
- Imasato, N., What is tide-induced residual current?, *J. Phys. Oceanogr.*, *13*, 1307-1317, 1983.
- Kalkwijk, J. P. T. and R. Booij, Adaptation of secondary flow in nearly-horizontal flow, *Journal of Hydraulic Research*, *24*, 19-37, 1986.
- Keulegan, G. H. and L. H. Carpenter, Forces on cylinders and plates in an oscillating fluid, *J. Res. Nat. Bur. Stand.*, *60*, 1958.
- Loder, J. W., Topographic rectification of tidal currents on the sides of Georges Bank, *J. Phys. Oceanogr.*, *10*, 1399-1416, 1980.
- Longuet-Higgins, M. S., On the transport of mass by time-varying ocean currents, *Deep Sea Res.*, *16*, 431-447, 1969.
- Marchuk, G. I., *Numerical methods in weather prediction*, Academic Press, 1974, 277 pp.
- Mesinger, F. and A. Arakawa, *Numerical methods used in atmospheric models*, GARP Publication series 17, WMO-ICSU Joint Organizing Committee, 1976, 64 pp.
- Milne-Thompson, L. M., *Theoretical hydrodynamics*, Macmillan, London, 1938, 552 pp.
- Nihoul, J. C. J. (ed.), *Three-dimensional models of marine and estuarine dynamics*, vol. 45 of *Elsevier Oceanography series*, Elsevier, 1987.
- Nihoul, J. C. J. and F. C. Roday, The influence of the "tidal stress" on the residual circulation: application to the Southern Bight of the North Sea, *Tellus*, *27*, 484-490, 1975.
- Orlanski, I., A simple boundary condition for unbounded hyperbolic flows, *J. Comput. Phys.*, *21*, 251-269, 1976.
- Ottino, J., C. Leong, H. Rising, and P. Swanson, Morphological structures produced by mixing in chaotic flows, *Nature*, *333*, 419-425, 1988.
- Pasmanter, R. A., Deterministic diffusion, effective shear and patchiness in shallow tidal flows, in *Physical Processes in Estuaries*, edited by J. Dronkers and W. van Leussen, pp. 42-52, Springer-Verlag, Berlin, 1988.
- Pingree, R., The formation of The Shambles and other banks by tidal stirring of the seas., *J. Mar.*

- Biol. Ass. U.K.*, 58, 211-226, 1978.
- Pingree, R. and D. K. Griffiths, Sand transport paths around the British Isles resulting from m_2 and m_4 tidal interactions, *J. Mar. Biol. Ass. U.K.*, 59, 497-513, 1979.
- Pingree, R. and L. Maddock, Tidal eddies and coastal discharge, *J. Mar. Biol. Ass. U.K.*, 57, 869-875, 1977.
- Prandtl, L., *The Essentials of Fluid Dynamics*, Blackie, 1952.
- Richtmyer, T. D. and K. W. Morton, *Difference methods for initial-value problems*, John Wiley and Sons, New York, second edition, 1967.
- Roache, P. J., *Computational Fluid Dynamics*, Hermosa Publishers, Albuquerque, NM, 1976, 446 pp.
- Roberts, K. V. and N. O. Weiss, Convective difference schemes, *Maths. Comput.*, 20, 272-299, 1966.
- Robinson, I., Tidal vorticity and residual circulation, *Deep Sea Res.*, 28A, 195-212, 1981.
- Schlichting, H., *Boundary-layer theory*, McGraw-Hill, sixth edition, 1968.
- Shapiro, R., Linear filtering, *Mathematics of Computation*, 29, 1094-1097, 1975.
- Spaulding, M. L., A vertically averaged circulation model using boundary-fitted coordinates, *J. Phys. Oceanogr.*, 14, 973-982, 1984.
- Tee, K., Tide-induced residual current, a 2-D nonlinear numerical tidal model, *J. Mar. Res.*, 34, 603-628, 1976.
- Tee, K. T., Tide-induced residual current—verification of a numerical model, *J. Phys. Oceanogr.*, 7, 396-402, 1977.
- Uncles, R. J., Residual currents in the Severn Estuary and their effects on dispersion, *Oceanol. Acta*, 5, 403-410, 1982.
- Wilkin, J., L., A computer program for generating two-dimensional orthogonal curvilinear coordinate grids, 1988, unpublished document, 12 pp.
- Williamson, C., Sinusoidal flow relative to circular cylinders, *J. Fluid Mech.*, 155, 141-174, 1985.
- Wolanski, E., J. I. and M. Heron, Island wakes in shallow coastal waters, *J. Geophys. Res.*, 89, 10,553-10,569, 1984.
- Zimmerman, J., Mixing and flushing of tidal embayments in the Western Dutch Wadden Sea, part II: analysis of mixing processes, *Neth. J. Sea Res.*, 10(4), 397-439, 1976.
- Zimmerman, J. T. F., Topographic generation of residual circulation by oscillatory tidal currents, *Geophys. Astrophys. Fluid Dynamics*, 11, 35-47, 1978.
- Zimmerman, J. T. F., On the Euler-Lagrange transformation and the Stokes drift in the presence of oscillatory and residual currents, *Deep Sea Res.*, 26A, 505-520, 1979.